Linear Sparse Regular Array Antenna Demonstrator

by

Rina-Mari Weideman

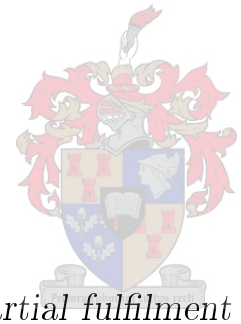

Thesis presented in partial fulfilment of the requirements for the degree of Master of Engineering (Electronic) in the Faculty of Engineering at Stellenbosch University

Supervisor: Prof. DIL de Villiers

March 2021

Declaration

By submitting this thesis electronically, I declare that the entirety of the work contained therein is my own, original work, that I am the sole author thereof (save to the extent explicitly otherwise stated), that reproduction and publication thereof by Stellenbosch University will not infringe any third party rights and that I have not previously in its entirety or in part submitted it for obtaining any qualification.

Date: March 2021 .....

Abstract

Linear Sparse Regular Array Antenna Demonstrator

R. Weideman

Department of Eletrical and Electronic Engineering,
University of Stellenbosch,
Private Bag X1, Matieland 7602, South Africa.

Thesis: MEng (EE)

March 2021

Sparse uniform linear arrays (ULAs), i.e., arrays with adjacent elements spaced further than a half-wavelength, have advantages over dense ULAs, such as an improved resolution for the same number of receivers and reduced mutual coupling effects. Due to the sparse ULAs not satisfying the spatial Nyquist criterion, however, aliasing is introduced when applying direction of arrival (DOA) estimation methods, meaning that ambiguous results are achieved. A new DOA estimation method based on exponential analysis, called Validated Exponential Analysis (VEXPA) has been developed in [1] to overcome this problem, making use of the aliasing effect rather than avoiding it.

This project investigated the practical performance of VEXPA. We found that the use of VEXPA with sparse arrays can improve the angular resolution with a factor of up to five from that of a dense array. The biggest drawback of the technique was found to be the specific case when multiple signals are unable to be distinguished from each other. The method also struggles to deliver accurate results with low-resolution quantised data, which is a disadvantage as high-resolution quantisers are costly and require an intricate design process.

A small four-element prototype antenna array was manufactured. Experiments were performed in an anechoic chamber with a single source. The results returned by VEXPA proved to be accurate.

Uittreksel

Lineêre Yl Reëlmatige Skikkingsantenna Demonstrator

("Linear Sparse Regular Array Antenna Demonstrator")

R. Weideman

Departement Elektriese en Elektroniese Ingenieurswese,
Universiteit van Stellenbosch,
Privaatsak X1, Matieland 7602, Suid Afrika.

Tesis: MIng (EE)

Maart 2021

Yl eenvormige reëlmatige skikkingsantennas, d.w.s. skikkingsantennas met aangrensende elemente verder as 'n half-golflengte gespasieër, het voordele bo digte eenvormige reëlmatige skikkingsantennas, soos 'n verbeterde resolusie vir dieselfde aantal ontvangers en verminderde wedersydse koppeling. As gevolg van die feit dat yl eenvormige reëlmatige skikkingsantennas nie die ruimtelike Nyquist kriterium nakom nie, word aliasering veroorsaak wanneer rigtingsafskatting metodes toegepas word, wat beteken dubbelsinnige resultate word gelewer. 'n Nuwe rigtingsafskatting metode wat gebaseer is op eksponensiële analise, met die naam van Bevestigde Eksponensiële Analise ("VEXPA"), is ontwerp in [1] om hierdie probleem te oorkom, waar daar eerder van die aliasering gebruik gemaak word as om dit te probeer voorkom.

Hierdie projek het die praktiese uitvoering van VEXPA ondersoek. Ons het gevind dat die gebruik van VEXPA met yl skikkingsantennas die resolusie tot 'n faktor van vyf kan verbeter van die resolusie wat 'n digte skikkingsantenna bied. Die grootste nadeel van die tegniek is die geval wanneer meervoudige seine nie van mekaar onderskei kan word nie. Hierdie metode sukkel ook om akkurate resultate te lewer met lae-resolusie gekwantiseerde data, wat 'n nadeel is omdat hoë-resolusie kwantiseerders duur is en 'n ingewikkelde ontwerpproses behels.

'n Klein vier-element prototipe skikkingsantenna was vervaardig. Eksperimente was uitgevoer in 'n anechoïese kamer met 'n enkele bron. Die resultate gelewer deur VEXPA was akkuraat.

Acknowledgements

Without the following people and organisations, this thesis would have remained an unreachable goal and therefore I would like to express my thanks to:

- The South African Radio Observatory (SARAO) for funding this research.
- My supervisor, Prof. Dirk de Villiers, for always being involved and willing to share your insight. Your persistent eagerness to gain knowledge is inspirational. I am also grateful to you for lending me the opportunity to attend the ICEAA conference when my knowledge on the topic was still very limited.
- Ridalise Louw, not only for being a mentor I can look up to, but also for being a wonderful colleague and becoming a true friend. Every challenge I faced was more manageable with you being there.
- Prof. Annie Cuyt, Dr Wen-shin Lee and Ferre Knaepkens at the University of Antwerp for being willing to explain the VEXPA algorithm in such a way that transformed it from something perplexing to something straightforward.
- Anneke Bester, for spending multiple hours helping with the experimental setup.
- Wessel Croukamp, for manufacturing the dipoles and antenna array so swiftly and meticulously.
- All my family members and friends for offering support of both academic and emotional nature.

Contents

List of Figures

List of Tables

Acronyms

ADC Analogue-to-Digital Converter

AWGN Additive White Gaussian Noise

DBSCAN Density-Based Spatial Clustering of Applications with Noise

DOA Direction-of-Arrival

DOF Degrees of Freedom

ESPRIT Estimation of Signal Parameters via Rotational Invariance Techniques

FDM Frequency Division Multiplexing

FDMA Frequency Division Multiple Access

LS Least Squares

MOM Method Of Moments

MP Matrix-Pencil

MRA Minimum Redundancy Array

MUSIC Multiple Signal Classification

RFI Radio Frequency Interference

RMSE Root-Mean-Square Error

SD Standard Deviation

SNR Signal-to-Noise Ratio

SQNR Signal-to-Quantisation-Noise Ratio

TLS Total Least Squares

ULA Uniform Linear Array

VEXPA Validated Exponential Analysis

Chapter 1

Introduction

1.1 Radio astronomy and the SKA

When looking at the sky through an optical telescope, a lot can be learned about celestial objects in the universe. Some astronomical phenomena, however, are located in the radio frequency part of the electromagnetic spectrum and go unnoticed by optical astronomy. This is where radio astronomy comes into play.

Radio telescopes can detect invisible light and can be used even in cloudy skies. It is useful for perceiving [2]:

- the formation of stars and planets;
- molecules in cold interstellar clouds;
- hydrogen, the most abundant element;
- pulsars;
- cosmic magnetic fields;
- the early cosmos.

In 1932, the first radio waves were detected by the father of radio astronomy, Karl Jansky. Since then, significant progress has been made in the field. An issue that remains, however, is the fact that radio telescopes need to be much larger than optical telescopes to achieve the same resolution, due to radio sources having longer wavelengths.

The Square Kilometre Array (SKA) is an international project aiming to build the world's largest radio telescope, with a collecting area of a square kilometre [3]. Thousands of dishes will be linked together to form a telescope array, also known as an interferometer [4]. These dishes will be situated in the Karoo region in South Africa and Murchison Shire in Western Australia. The large collecting area, as well as the large number of dishes, will create the

opportunity for an increased image resolution quality, exceeding that of the Hubble Space Telescope. By the late 2020s, routine science observations are expected to commence [3].

1.2 Project objectives

The operation of radio astronomy observatories is often hampered by sources of radio frequency interference (RFI) such as digital devices or aircraft. The ability to detect such sources is therefore an important contribution to the field of radio astronomy. Methods to eliminate the effect of RFI include flagging the data, steering nulls towards the source, or eliminating the source by enforcing RFI mitigation regulations.

Traditional direction-of-arrival (DOA) estimation algorithms rely on antenna arrays that adhere to the spatial Nyquist criterion, i.e., adjacent antenna elements are spaced closer than half a wavelength. These dense arrays have the disadvantage of higher mutual coupling and a lower angular resolution. DOA estimation methods that are able to perform using the existing sparse telescope infrastructure are therefore ideal.

This thesis focuses on a newly developed exponential analysis algorithm Validated Exponential Analysis (VEXPA) that specifically allows antenna elements to be spaced sparsely, and is also able to detect the number of incoming signals accurately [1]. The main aim of this project is to investigate the practical limitations of the VEXPA algorithm for use in sparse array antenna DOA estimation applications.

1.3 Thesis layout

The above objectives are achieved and described in the following chapters:

- Chapter 2: Direction-of-arrival estimation theory. The theory behind DOA estimation is presented. We look at the data model of the signals captured by the antenna array, as well as traditional DOA estimation methods used on dense arrays. We also briefly discuss existing sparse array configurations.

- Chapter 3: Validated Exponential Analysis (VEXPA). We take a detailed look at the VEXPA algorithm, with specific focus on the required array configuration, how the number of incoming signals is estimated, and how the aliased results are used to resolve the true DOAs.

- Chapter 4: Simulated performance of VEXPA. Here we consider the different practical limitations of the VEXPA algorithm by performing simulations.

- Chapter 5: Practical performance of VEXPA. We discuss the process of designing and manufacturing a simple antenna array that is used in a practical experiment. VEXPA is performed on the captured data of the system, and these results are discussed.
- Chapter 6: Conclusion. We conclude the thesis by discussing the findings of the practical performance of the VEXPA algorithm and mentioning future work te be done on the topic.

Chapter 2

Direction-of-arrival estimation theory

2.1 Antenna arrays

Single element antennas have the disadvantage of requiring a large aperture if a high directivity is needed. In this case, using multiple interfering antennas, called an antenna array, is beneficial, as a high gain and directivity can be achieved. The phase of each element can be steered to change the main beam direction of the complete array. For this project, we will focus solely on array antennas that are both uniform and linear, meaning that the elements are equispaced in a straight line. These arrays are known as uniform linear arrays (ULAs). Other two-dimensional antenna configurations include planar and conformal arrays. This section will describe general antenna array theory, including concepts relevant to both transmitting and receiving systems.

Figure 2.1 shows a signal impinging on a ULA with M elements. A narrow-band signal is assumed, as well as omnidirectional elements and an isotropic linear transmission medium. The antenna elements are in the far-field of the source. These assumptions will be described in more detail in a later section.

The distance d between consecutive ULA elements causes a delay in time at which an incident signal is received at each element. This delay is given by

$$\tau_i = \frac{d \cos \phi_i}{c}, \tag{2.1}$$

where ϕ_i is the direction of the incoming signal, measured from the axis of the array, and c is the speed of light. This time delay corresponds to a phase difference in the received signal at consecutive elements, given by

$$\Delta\Psi = kd \cos \phi_i, \tag{2.2}$$

where $k = \frac{2\pi}{\lambda}$ is the wavenumber, and λ is the wavelength.

The array factor of an array antenna is an element-by-element sum that is multiplied by the radiation pattern of each individual antenna to deliver the

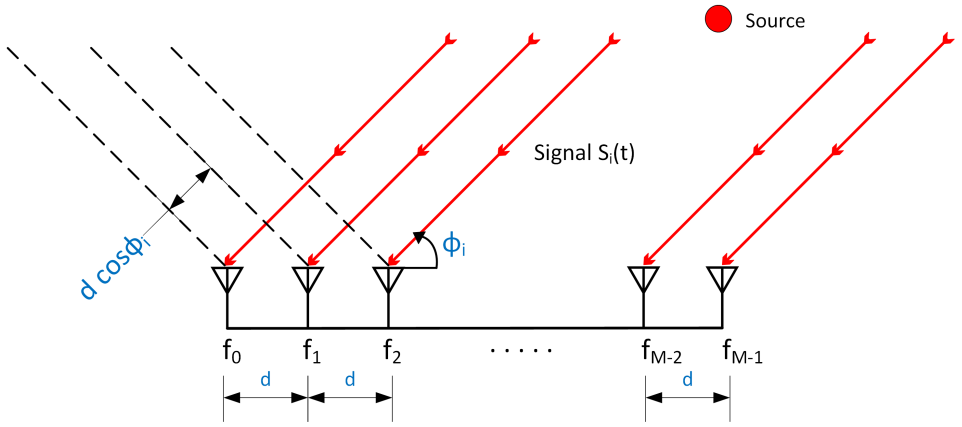

Figure 2.1: ULA with M elements, with an incoming signal at an angle of ϕ_i.

output of the complete array [5]. It is calculated as

$$AF(\phi) = \sum_{m=0}^{M-1} a_m e^{j(\Psi_m + mkd\cos\phi)}. \tag{2.3}$$

The values M, a_m and Ψ_m represent the number of antenna elements, the gain and phase shift of the specific element, respectively.

To sum the received signals at each element in phase to produce a maximum in the direction of the incoming signal, the phase shift Ψ_m must be given by [6]

$$\Psi_m = -mkd\cos\phi_i. \tag{2.4}$$

The array factor can then be rewritten as

$$AF(\phi) = \sum_{m=0}^{M-1} a_m e^{jmkd(\cos\phi - \cos\phi_i)}. \tag{2.5}$$

2.1.1 Spatial Nyquist criterion

If we define $v = \cos\phi$, we can observe that the array factor is a periodic function of v with period $\frac{2\pi}{kd} = \frac{1}{d/\lambda} = \frac{\lambda}{d}$. The array factor reaches a maximum value when the exponent $kd(v - v_0)$ is a factor of 2π. This can be expressed as [6]

$$kd(v - v_0) = 2\pi n, \qquad n \in \mathbb{Z} \tag{2.6}$$

$$v_n - v_0 = \frac{n}{d/\lambda}. \tag{2.7}$$

The beam that occurs when $n = 0$ is referred to as the main lobe. When the array factor has multiple maximum values, unwanted large beams occur, commonly referred to as grating lobes. This effect is known as aliasing: the

grating lobes are aliases of the true main beam. Since grating lobes diminish the power in the main beam, they should be avoided in most applications. The first grating lobe that occurs is at $n = 1$. For real angles of ϕ, called the visible space, v can occupy a range of values between -1 and 1. Substituting $n = 1$ and $v_1 = 1$ into (2.6), we find that

$$1 - \cos\phi_i = \frac{\lambda}{d}. \tag{2.8}$$

This means that the criterion for maximum spacing to avoid grating lobes is

$$\frac{d}{\lambda} < \frac{1}{1 - \cos\phi_{imax}}. \tag{2.9}$$

Since the maximum angle of arrival possible is 180°, the criterion is simplified to

$$d < \frac{\lambda}{2}. \tag{2.10}$$

Equation (2.10) is known as the spatial Nyquist criterion. Arrays that violate this limit are referred to as sparse arrays. Sparse array configurations have certain advantages over densely spaced arrays, such as an increased angular resolution and less mutual coupling.

The achievable resolution of an array with a fixed number of elements is determined by the Rayleigh limit

$$\Delta_\phi \approx \frac{\lambda}{D}, \tag{2.11}$$

where Δ_ϕ is the resolution in radians, and D is the total length of the array. For a fixed number of elements, D is larger for a sparser array, as the elements are spaced further apart. It is clear that a sparse array therefore has a smaller, and thus increased resolution. On the other hand, sparse arrays pose the problem of delivering ambiguous results due to the violation of the Nyquist criterion [7].

2.2 Direction-of-arrival estimation problem formulation

The azimuthal angle of incoming signals can be determined by using the phase differences caused by the spacing between antenna elements. For one-dimensional DOA estimation of ULAs, we make a few assumptions [8]:

- *Isotropic and linear transmission medium*: The medium through which the signals are travelling is isotropic, meaning that its physical properties

are the same for all directions. At any point, the incoming signals can be superimposed linearly. This assumption ensures that the propagation property does not change as the DOA changes, and also that the signal received by the array can be expressed as a sum of all individual signals impinging on the array.

- *Far-field assumption*: The far-field of an antenna array is the space where the distance from the array is much larger than the dimension of the array. A source is usually accepted to be in the far-field if it is further than $2D^2/\lambda$ from the array, where D is the dimension of the array, and λ is the wavelength of the signal. We assume that all signals impinging on the array are in the far-field of the array. This ensures that the wavefront of the signals are planar, meaning all propagating rays are parallel to one another.

- *Narrowband assumption*: The assumption is made that the amplitude and phase of the incoming signals vary slowly with respect to time. Specifically, that the time rate of change of the signal amplitude and phase is significantly smaller than the time it takes the signal to traverse the length of the array. This ensures that one may assume the same phasor is impinging on all the antennas in the array when describing the problem in the frequency (phasor) domain.

- *Additive white Gaussian noise (AWGN) channel*: The noise that is added to the incoming signals is complex white Gaussian noise with a constant variance σ^2 at all elements and no correlation at any element. It is also independent from the sources.

Taking these four assumptions into account, the incoming signals can be written as complex exponentials

$$S_i(t) = s_i(t)\exp(j\omega t), \qquad s_i(t) = a_i(t)\exp(jp_i(t)). \tag{2.12}$$

If the ULA receiving these signals consists of M elements, the samples $f_1(t), ..., f_M(t)$ at time t are [7]

$$f_m(t) = \sum_{i=1}^{n} S_i(t + m\tau_i), \tag{2.13}$$

with τ_i as defined in (2.1), and n referring to the number of incoming signals. As the amplitude a_i and phase p_i do not vary noticeably across the different antenna elements (the narrowband assumption), we can state that

$$s_i(t + m\tau_i) \approx s_i(t), \tag{2.14}$$

which means that

$$\begin{aligned} S_i(t + m\tau_i) &= s_i(t + m\tau_i)\exp(j\omega(t + m\tau_i)) \\ &\approx S_i(t)\exp(j\omega m\tau_i). \end{aligned} \tag{2.15}$$

Thus, we can rewrite (2.13) as

$$\begin{aligned} f_m(t) &\approx \sum_{i=1}^{n} S_i(t)\exp(j\omega m\tau_i) \\ &= \sum_{i=1}^{n} S_i(t)\exp\left(\frac{j\omega md\cos\phi_i}{c}\right). \end{aligned} \tag{2.16}$$

This exponential analysis problem is defined by what we call the base terms

$$\Psi_i = \exp(\psi_i d), \tag{2.17}$$

with ψ_i known as the exponents:

$$\psi_i = \frac{j\omega\cos\phi_i}{c}. \tag{2.18}$$

In terms of these base terms, (2.16) becomes

$$f_m(t) = \sum_{i=1}^{n} S_i(t)\Psi_i^m, \quad m = 0, ..., M-1. \tag{2.19}$$

To introduce a more concise notation, we can construct a matrix using the base terms:

$$A = \begin{bmatrix} 1 & 1 & \dots & 1 \\ \Psi_1^1 & \Psi_2^1 & \dots & \Psi_n^1 \\ \vdots & \vdots & \ddots & \vdots \\ \Psi_1^{M-1} & \Psi_2^{M-1} & \dots & \Psi_n^{M-1} \end{bmatrix} \tag{2.20}$$

The above matrix A is called the steering matrix of size $M \times n$, with its columns referred to as the steering vectors $\boldsymbol{a}_1, \boldsymbol{a}_2, ..., \boldsymbol{a}_n$, corresponding to the n incoming signals. It is noteworthy that the steering matrix takes the form of a Vandermonde matrix. In a practical system, noise will be added to each element. With noise added to (2.19), a matrix equation can be written

$$\boldsymbol{f}(t) = A\boldsymbol{S}(t) + \boldsymbol{n}(t), \tag{2.21}$$

where $\boldsymbol{S}(t)$ is the signal vector $\begin{bmatrix} S_1 & S_2 & \cdots & S_n \end{bmatrix}^T$, and $\boldsymbol{n}(t)$ is the $M \times 1$ noise vector. The vector $\boldsymbol{f}(t) = \begin{bmatrix} f_1 & f_2 & \cdots & f_M \end{bmatrix}^T$ contains the output samples of the ULA. Once the base terms are recovered from the steering matrix A, the angles of arrival ϕ_i can readily be retrieved by using (2.17) and (2.18).

Relating to Section 2.1.1, we consider the spatial Nyquist criterion with regards to DOA estimation. It is critical that a one-to-one mapping is achieved since in the case that more than one angle corresponds to the same base term, the ambiguous results will not allow us to identify the true DOA. The base terms take on values that lie on the unit circle: complex numbers with unit amplitude and phase $\frac{\omega \cos \phi_i d}{c}$. As the possible DOA values ϕ_i lie between $0°$ and $180°$, the phases lie in the range

$$\left[\frac{\omega d}{c}, -\frac{\omega d}{c}\right]. \tag{2.22}$$

To ensure a one-to-one mapping of this phase to the base terms, these phases should be in the range $[\phi_0, \phi_0 + 2\pi]$, $\phi_0 \in \mathbb{R}$. This means that the difference between the limits of the range in (2.22) should be strictly smaller than 2π, implying the inequality

$$\begin{aligned} \frac{\omega d}{c} - \left(-\frac{\omega d}{c}\right) &< 2\pi \\ \frac{2\omega d}{c} &< 2\pi \\ \frac{4\pi d}{\lambda} &< 2\pi \\ d &< \frac{\lambda}{2}. \end{aligned} \tag{2.23}$$

If this criterion is violated, aliasing occurs, which in turn requires sparse DOA estimation methods to rectify. Some methods making use of dense ULAs are discussed in the following section.

2.3 Direction-of-arrival estimation methods

We have now described the data model resulting from samples of a ULA. Several methods exist to estimate the base terms and in turn, the angles of arrival. Some of these methods will now be discussed, namely beamforming, Multiple Signal Classification (MUSIC) and its variant Root-MUSIC, Estimation of Signal Parameters via Rotational Invariance Techniques (ESPRIT) and the Matrix-Pencil method.

2.3.1 Beamforming

Beamforming is a popular traditional method of DOA estimation. It is based on the process of combining the incoming signals from a range of possible directions, with a weight vector added for each respective direction. The output signal should be undistorted, with a maximum average power at the genuine direction of arrival, whereas the other angles will produce distorted results [9].

Conventional beamformers do not depend on the incoming signals and use only the array response, whereas adaptive beamformers use the received data to calculate the appropriate weight vectors, leading to an improved resolution.

The weight vectors are calculated by using the known time delay of each element. Each delay is added to the signal received at the respective element, after which all the signals are summed. If $\boldsymbol{w}$ and $\boldsymbol{x}$ are the weight vector and input vector respectively, the output signals are

$$y(t) = \boldsymbol{w}^H \boldsymbol{x}(t). \tag{2.24}$$

$(\,.\,)^H$ indicates the conjugate transpose. If the output power of the antenna array is averaged over a certain number of time samples K, the following equation is obtained:

$$\begin{aligned} P(\boldsymbol{w}) = \frac{1}{K}\sum_{k=1}^{K} |\, y(t_k)\,|^2 &= \frac{1}{K}\sum_{k=1}^{K} \boldsymbol{w}^H \boldsymbol{x}(t_n)\boldsymbol{x}^H(t_n)\boldsymbol{w} \\ &= \boldsymbol{w}^H R \boldsymbol{w}. \end{aligned} \tag{2.25}$$

There are different methods to define the weight vector $\boldsymbol{w}$, of which the most simple is the conventional beamformer technique. This method defines $\boldsymbol{w}$ as the array steering vector $\boldsymbol{a}(\phi)$ for all possible angles of arrival. At the true impinging angle(s), the steering vector, and thus weight vector, will cause the phases of the received signals to add constructively, causing a peak in the power spectrum [8].

2.3.2 Multiple Signal Classification (MUSIC)

MUSIC is a subspace-based DOA method, meaning that the noise and signal subspaces of the incoming signals are retrieved through eigendecomposition [10]. This method was first presented by Schmidt in 1979 [11].

If we consider the same data model as in (2.21), we can calculate the $M \times M$ covariance matrix of the output data as

$$\begin{aligned} R &= E[\boldsymbol{f}(t)\boldsymbol{f}(t)^H] \\ &= AE[\boldsymbol{S}(t)\boldsymbol{S}(t)^H]A^H + E[\mathbf{n}(t)\mathbf{n}(t)^H] \\ &= AR_{ss}A^H + \sigma^2 I_M \end{aligned} \tag{2.26}$$

where R_{ss} represents the signal covariance matrix, σ the variance of the noise, and I_M the identity matrix of size $M \times M$ [8]. $E[\,.\,]$ represents the statistical expectation, which can be approximated by using the temporal average of the K time samples of the antenna array:

$$R = \frac{1}{K}\sum_{k=1}^{K} \mathbf{f}(t_k)\mathbf{f}^H(t_k) \tag{2.27}$$

If the number of samples K is very large, this estimated covariance matrix is an accurate approximation of the true covariance matrix.

It is further noted that R has M eigenvalues $\lambda_1, ..., \lambda_M$ that all satisfy the equation

$$| R - \lambda_i I_M | = 0. \tag{2.28}$$

$|\,.\,|$ denotes the determinant operation. Substituting (2.26) into (2.28) yields

$$| AR_{ss}A^H + \sigma^2 I_M - \lambda_i I_M | = 0. \tag{2.29}$$

Moreover, this implies that the eigenvalues of the matrix $AR_{ss}A^H$ are

$$\gamma_i = \lambda_i - \sigma^2, \quad i = 0, ..., M-1. \tag{2.30}$$

A has full column rank as it is composed of the linear independent steering vectors. Additionally, if the incoming signals are uncorrelated, the covariance matrix R_{ss} contains non-zero entries only along its diagonal, and is thus nonsingular [12]. These two characteristics ensure that $AR_{ss}A^H$ is positive semidefinite with its rank being equal to the number of incoming signals, n. This implies $M - n$ of its eigenvalues are equal to zero. We can rewrite (2.30) as

$$\gamma_i = \begin{cases} \lambda_i - \sigma^2, & \text{if } 1 \leq i \leq n, \\ \lambda_i - \sigma^2 = 0, & \text{if } n+1 \leq i \leq M, \end{cases} \tag{2.31}$$

which results in the following eigenvalues for R,

$$\lambda_i = \begin{cases} \gamma_i + \sigma^2, & \text{if } 1 \leq i \leq n, \\ \sigma^2, & \text{if } n+1 \leq i \leq M. \end{cases} \tag{2.32}$$

We can assign eigenvectors $\mathbf{q}_i$ to the $M - n$ smallest eigenvalues λ_i as

$$\left(R - \sigma^2 I_M\right) \mathbf{q}_i = 0, \qquad n+1 \leq i \leq M. \tag{2.33}$$

Substituting (2.26) into (2.33), we achieve

$$\begin{aligned} \left(R - \sigma^2 I_M\right) \mathbf{q}_i &= AR_{ss}A^H\mathbf{q}_i + \sigma^2 I_M \mathbf{q}_i - \sigma^2 I_M \mathbf{q}_i \\ &= AR_{ss}A^H\mathbf{q}_i = 0. \end{aligned} \tag{2.34}$$

As R_{ss} is nonsingular and A^HA is full rank, both ${R_{ss}}^{-1}$ and $\left(A^HA\right)^{-1}$ exist [13]. If we multiply (2.34) with ${R_{ss}}^{-1}\left(A^HA\right)^{-1}A^H$ then,

$${R_{ss}}^{-1}\left(A^HA\right)^{-1}A^HAR_{ss}A^H\mathbf{q}_i = 0, \tag{2.35}$$

leading to,

$$A^H\mathbf{q}_i = 0, \qquad n+1 \leq i \leq M. \tag{2.36}$$

The above equation presents the useful observation that the n steering vectors of the incoming signals are orthogonal to the eigenvectors of the $M-n$ smallest eigenvalues of the covariance matrix:

$$\{\boldsymbol{a}_1, ..., \boldsymbol{a}_n\} \perp \{\boldsymbol{q}_{n+1}, ..., \boldsymbol{q}_M\}. \tag{2.37}$$

Here we are introduced to the concept of two subspaces that are orthogonal, i.e., the signal and noise subspace. This orthogonality appears in (2.37), as the steering vectors belong to the signal subspace, whereas the eigenvectors corresponding to the $M-n$ smallest eigenvalues belong to the noise subspace (since these eigenvalues are equal to the noise variance).

We can then construct the noise subspace by appending these eigenvectors:

$$E_N = \begin{bmatrix} \boldsymbol{q}_{n+1} & \cdots & \boldsymbol{q}_M \end{bmatrix}. \tag{2.38}$$

Due to the orthogonality of the noise and signal subspace, $\boldsymbol{a}(\phi)^H E_N {E_N}^H \boldsymbol{a}(\phi) = 0$ when $\phi = \phi_i$, with ϕ_i denoting the correct angles of arrival. As it is numerically easier to find peaks than zeros, we define the MUSIC spectrum as

$$Z_{\text{MUSIC}}(\phi) \coloneqq \frac{1}{\boldsymbol{a}(\phi)^H E_N {E_N}^H \boldsymbol{a}(\phi)}, \tag{2.39}$$

and solve for the n angles that maximise this quantity.

2.3.2.1 Root-MUSIC

An adaptation of the MUSIC algorithm, known as Root-MUSIC, avoids the search spectrum step and provides an alternative solution from the noise subspace [14]. Rewriting the MUSIC spectrum as

$$Z_{\text{MUSIC}}(\phi) = \frac{1}{\boldsymbol{a}(\phi)^H C \boldsymbol{a}(\phi)}, \tag{2.40}$$

where $C = E_N {E_N}^H$. The matrix multiplication of the spectrum denominator can be expressed as a summation:

$$\begin{aligned} \boldsymbol{a}(\phi)^H C \boldsymbol{a}(\phi) &= \sum_{m=1}^{M} \sum_{n=1}^{M} \exp\left(\frac{j\omega d(m-1)\cos\phi}{c}\right) C_{mn} \exp\left(\frac{j\omega d(n-1)\cos\phi}{c}\right) \\ &= \sum_{\ell=-M+1}^{M-1} C_\ell \exp\left(\frac{j\omega d\ell\cos\phi}{c}\right). \end{aligned} \tag{2.41}$$

In the equation above, C_ℓ is the sum of the elements along the ℓth diagonal of matrix C:

$$C_\ell \triangleq \sum_{m-n=\ell} C_{mn}. \tag{2.42}$$

We can now write the denominator as a polynomial $D(z)$,

$$D(z) = \sum_{\ell=-M+1}^{M-1} C_\ell z^\ell. \tag{2.43}$$

It is important to note that the zeros of $D(z)$ correspond to the base terms Ψ_i which relate to the angles that create peaks in $Z_{\text{MUSIC}}(\phi)$. The n zeros that represent the true base terms will lie closest to the unit circle, i.e., $z = z_\ell = |z_\ell| \exp(j \arg(z_\ell))$, where $|z_\ell| = 1$. One of the key advantages of Root-MUSIC over MUSIC is that Root-MUSIC performs better than MUSIC for cases where signal peaks lie close together in the MUSIC spectrum. The non-Root MUSIC algorithm often cannot distinguish between these peaks, finding only one signal when there are in fact more [15]. Another advantage of Root-MUSIC is that it is less computationally intensive, as no search step is required. On the other hand, Root-MUSIC has the restriction that it is only realisable for uniform arrays.

2.3.3 ESPRIT

A complication introduced by most DOA estimation algorithms is that the steering matrix $A(\phi)$ should be known precisely. Searching over the parameter space, such as in MUSIC, can also require substantial computational effort. The above two issues are alleviated by the DOA estimation method ESPRIT, by requiring array elements to occur in pairs, causing a displacement invariance [16].

The array configuration of ESPRIT is based on two identical sub-arrays, where the antenna elements are allowed to belong to either or both of these arrays. If the total number of elements is M, the number of elements in each sub-array is $k \geq M/2$ for overlapping arrays, and $k = M/2$ when no overlap occurs. Element pairs are formed containing one element of each sub-array. There exists a displacement vector describing the shift from one element of the pair to the other. This vector should be identical for all pairs to cause a displacement invariance, leading to a rotational invariance of signal sub-spaces [8]. This rotational invariance is the crux of the ESPRIT method to estimate DOAs. An example of an ESPRIT-based planar array configuration can be seen in Fig. 2.2, where three element pairs are present.

Now denote the output signals of two sub-arrays $\boldsymbol{x}(t)$ and $\boldsymbol{y}(t)$, with each array receiving its own noise vector $\boldsymbol{n}_x(t)$ and $\boldsymbol{n}_y(t)$. The two arrays are separated by a known displacement vector $\boldsymbol{\Delta}$ with magnitude Δ. Using the same data model as in Section 2.2, we can write the outputs at element m

$$\boldsymbol{x}_m(t) = \sum_{i=1}^{n} S_i(t)\Psi_i^m + \boldsymbol{n}_{xm}(t), \quad m = 0, ..., k_x - 1 \tag{2.44}$$

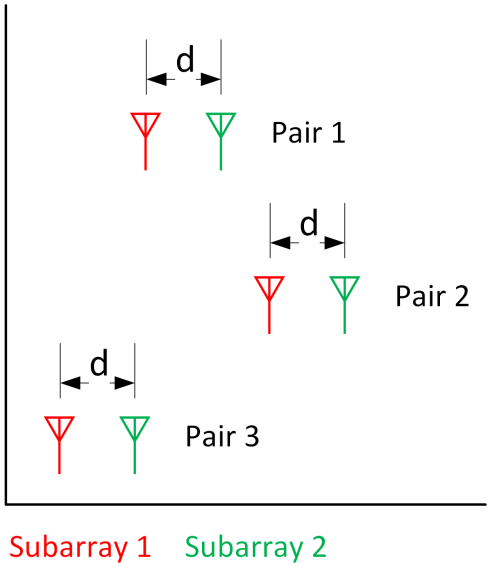

Figure 2.2: An example of an ESPRIT-based planar antenna array. Three element pairs are present, all with the same displacement vector d between elements. The red elements belong to one subarray, and the green elements to another.

$$\boldsymbol{y}_m(t) = \sum_{i=1}^{n} S_i(t) \exp\left(-j\omega\Delta \cos\phi_i/c\right)\Psi_i^m + \boldsymbol{n}_{ym}(t), \quad m = 0, ..., k_y - 1 \tag{2.45}$$

Using (2.44) and (2.45), the combined output of all elements can be written as

$$\boldsymbol{x}(t) = A\boldsymbol{S}(t) + \boldsymbol{n}_x(t), \tag{2.46}$$

$$\boldsymbol{y}(t) = A\Phi\boldsymbol{S}(t) + \boldsymbol{n}_y(t), \tag{2.47}$$

where Φ is the so-called rotational operator, and contains the phase delays between the two elements of each pair:

$$\Phi = \text{diag}\left\{e^{\Gamma_1}, \ldots, e^{\Gamma_n}\right\}, \tag{2.48}$$

where $\Gamma_i = -j\omega\Delta\cos\phi_i/c$. The goal of the ESPRIT algorithm is to estimate the signal subspace, after which the subspace rotation operator can be found, containing the true DOAs.

If we define $\boldsymbol{z}(t)$ to contain the outputs of both arrays, (2.46) and (2.47) can be combined to show that

$$\boldsymbol{z}(t) = \begin{bmatrix}\boldsymbol{x}(t) & \boldsymbol{y}(t)\end{bmatrix}^T = \tilde{A}\boldsymbol{S}(t) + \boldsymbol{n}_z(t), \tag{2.49}$$

where $\tilde{A} = \begin{bmatrix} A & A\Phi \end{bmatrix}^T$ and $\boldsymbol{n}_z(t) = \begin{bmatrix} \boldsymbol{n}_x(t) & \boldsymbol{n}_y(t) \end{bmatrix}^T$. As with MUSIC (Section 2.3.2), the covariance matrix of the measurements is calculated as

$$\begin{aligned} R &= E[\boldsymbol{z}(t)\boldsymbol{z}(t)^H] \\ &= \tilde{A}R_{ss}\tilde{A}^H, \end{aligned} \tag{2.50}$$

where $\text{rank}(R_{ss}) = \text{rank}(\tilde{A}) = n$. Now suppose $E_s = \begin{bmatrix} \boldsymbol{e}_1 & \dots & \boldsymbol{e}_n \end{bmatrix}$ is defined as a basis of the signal subspace. Then E_s spans the same space as $\tilde{A}$, as R_{ss} has full rank [8]. This implies that there exists a unique nonsingular matrix T, such that the following equation is satisfied:

$$E_s = \tilde{A}T. \tag{2.51}$$

Partitioning E_s into its components for the two sub-arrays, we get

$$E_s = \begin{bmatrix} E_1 \\ E_2 \end{bmatrix} = \begin{bmatrix} AT \\ A\Phi T \end{bmatrix}. \tag{2.52}$$

From (2.52) we can see that the range of E_1 and E_2 are both equal to the range of A. Because the two sub-arrays are identical, their outputs span the same signal subspace and have the same dimension. Thereafter, we can find a $d \times d$ nonsingular matrix Ψ such that

$$\begin{aligned} E_1\Psi &= E_2 \\ AT\Psi &= A\Phi T \end{aligned} \tag{2.53}$$

and

$$T\Psi T^{-1} = \Phi. \tag{2.54}$$

The above expression shows us that the diagonal elements of Φ are equal to the eigenvalues of Ψ, and the columns of T are the eigenvectors of Ψ. The matrix Ψ is referred to as the subspace rotating operator, and it maps the matrix E_1 to the matrix E_2.

In the noisy case, (2.50) changes to

$$\begin{aligned} R &= E[\boldsymbol{z}(t)\boldsymbol{z}(t)^H] \\ &= \tilde{A}R_{ss}\tilde{A}^H + \sigma^2 I_M. \end{aligned} \tag{2.55}$$

Due to the noise, the ranges of $E1$, $E2$ and A are no longer equal to one another, and therefore $E_1\Psi = E_2$ cannot be solved. As a result, the estimation of Ψ is usually performed using least squares (LS) or total least squares (TLS).

The standard LS method uses the simple matrix model $AX = B$, where X is the parameter of interest, A is a known matrix, and all errors are due to

noise present in matrix B. The estimated solution of X denoted as $\hat{X}$ is given as

$$\hat{X} = \left[AA^H\right]^{-1} A^H B. \tag{2.56}$$

In contrast to the LS method, the TLS method assumes noise in both matrices A and B [16]. This method finds the residual matrices R_A and R_B of minimum Frobenius norm such that

$$\left[A + R_A\right] \hat{X} = B + R_B. \tag{2.57}$$

Once Ψ is approximated, one can solve for the DOAs, as the eigenvalues of Ψ are equal to the diagonal values of Φ.

Often, it is preferable to operate on the array data directly instead of using the covariance matrix [16]. For example, when few samples are available, the covariance matrix cannot be accurately approximated. In [17], a variant to ESPRIT is presented that is based on the singular-value decomposition (SVD) of the direct data. This led to the development of another DOA estimation method by the name of Matrix Pencil, which will be discussed in the following subsection.

2.3.4 Matrix Pencil (MP) method

The Matrix-Pencil (MP) DOA estimation method holds advantages such as the ability to handle correlated incoming signals, and the ability to retrieve the angle of arrival from a single snapshot [18]. A snapshot is the output of the ULA at a fixed time t.

The concept of pencils was first introduced by F.R. Gantmacher in his book "The theory of matrices" [19]. If A and B are two matrices of the same size, a pencil is any matrix that satisfies $A + \lambda B$, where λ is a parameter. For the cases where λ is complex, the pencil is called a matrix pencil [20].

As this method solves the DOA estimation problem using a single snapshot, we alter the notations of (2.12) and (2.13) to be independent of time:

$$\alpha_i = S_i(t), \qquad f_m = f_m(t). \tag{2.58}$$

We start by defining two Hankel matrices of size $(M-L)\times L$, where L is known as the pencil parameter. L is commonly chosen to be a value lying between $M/3$ and $M/2$ [21]. We name the two matrices Y_1 and Y_2 and populate them with the samples of (2.58):

$$Y_2 = \begin{bmatrix} f_1 & f_2 & \cdots & f_L \\ f_2 & f_3 & \cdots & f_{L+1} \\ \vdots & \vdots & \ddots & \vdots \\ f_{M-L} & f_{M-L+1} & \cdots & f_{M-1} \end{bmatrix}, \tag{2.59}$$

$$Y_1 = \begin{bmatrix} f_0 & f_1 & \dots & f_{L-1} \\ f_1 & f_2 & \dots & f_L \\ \vdots & \vdots & \ddots & \vdots \\ f_{M-L-1} & f_{M-L} & \dots & f_{M-2} \end{bmatrix}. \tag{2.60}$$

Here, the similarity to ESPRIT is clear: Y_1 uses the samples $[f_0, ..., f_{M-L-1}]$, which can be seen as the first sub-ULA used by ESPRIT, and the same goes for Y_2 using the samples $[f_1, ..., f_{M-L}]$, corresponding to the second sub-ULA. These matrices can be factorised as

$$Y_2 = Z_1 D_\alpha D_\Psi Z_2, \tag{2.61}$$

$$Y_1 = Z_1 D_\alpha Z_2, \tag{2.62}$$

where

$$Z_1 = \begin{bmatrix} 1 & 1 & \dots & 1 \\ \Psi_1^1 & \Psi_2^1 & \dots & \Psi_n^1 \\ \vdots & \vdots & \ddots & \vdots \\ \Psi_1^{(M-L-1)} & \Psi_2^{(M-L-1)} & \dots & \Psi_n^{(M-L-1)} \end{bmatrix}, \tag{2.63}$$

$$Z_2 = \begin{bmatrix} 1 & \Psi_1^1 & \dots & \Psi_1^{(L-1)} \\ 1 & \Psi_2^1 & \dots & \Psi_2^{(L-1)} \\ \vdots & \vdots & \ddots & \vdots \\ 1 & \Psi_n^1 & \dots & \Psi_n^{(L-1)} \end{bmatrix}, \tag{2.64}$$

$$D_\Psi = diag \begin{bmatrix} \Psi_1 & \cdots & \Psi_n. \end{bmatrix}, \tag{2.65}$$

$$D_\alpha = diag \begin{bmatrix} \alpha_1 & \cdots & \alpha_n. \end{bmatrix}. \tag{2.66}$$

As before, n denotes the number of incoming signals, and Ψ_i represents the base terms as given in (2.17). We can create a matrix pencil

$$Y_2 - \lambda Y_1 = Z_1 D_\alpha \left(D_\Psi - \lambda I \right) Z_2, \tag{2.67}$$

where I is the $n \times n$ identity matrix.

As $\text{rank}(Y_1) = \text{rank}(Y_2) = n$, it follows that $\text{rank}(Y_2 - \lambda Y_1) = n$. However, this is not true when $\lambda = \Psi_i$, as this causes the ith entry of $D_\Psi - \lambda I$ to be zero, consequently making the rank of $Y_2 - \lambda Y_1$ equal to $n - 1$. The values of Ψ_i can therefore be found by determining the rank-reducing values of λ, which are the generalised eigenvalues of the generalised eigenvalue problem

$$Y_2 v_i = \lambda_i Y_1 v_i. \tag{2.68}$$

When the output data is noisy, the MP method has to be altered. We create a matrix Y as a combination of Y_1 and Y_2:

$$Y = \begin{bmatrix} f_0 & f_1 & \cdots & f_L \\ f_1 & f_2 & \cdots & f_{L+1} \\ \vdots & \vdots & \ddots & \vdots \\ f_{M-L-1} & f_{M-L} & \cdots & f_{M-1} \end{bmatrix}. \tag{2.69}$$

Note that Y_1 (Y_2) is the matrix Y with the last (first) column removed.

An SVD is performed on Y to separate the noise and signal subspaces,

$$Y = U\Sigma V^H, \tag{2.70}$$

with Σ containing the singular values of Y. Just as the $M-n$ smallest eigenvalues of the covariance matrix R are equal to the noise variance in (2.32), the $M-n$ smallest singular values here are equal to the noise variance, with the n largest singular values corresponding to the signal subspace. A filtered version of V is created by choosing the n columns that correspond to the n largest singular values:

$$V' = [V_1, ..., V_n]. \tag{2.71}$$

Now, Y_1 and Y_2 can be written as

$$Y_1 = U\Sigma' V_1'^H \tag{2.72}$$

$$Y_2 = U\Sigma' V_2'^H, \tag{2.73}$$

where V_1' and V_2' are obtained by removing the last and first rows of V', respectively, and Σ' is the n columns of Σ corresponding to the n largest singular values.

It can be shown that the values of Ψ_i for the noisy case can be found by solving the generalised eigenvalue problem

$$V_2' v_i = \lambda_i V_1' v_i, \tag{2.74}$$

similar to the noiseless case in (2.68).

2.4 Sparse array configurations

To win the advantages offered by sparse arrays, the disadvantage of the violation of the spatial Nyquist criterion is introduced. Existing sparse array configurations offer solutions to mitigate the aliasing caused by this violation. Some of these configurations are discussed in this section, namely co-prime arrays, minimum redundancy arrays (MRAs) and nested arrays.

2.4.1 Co-prime arrays

A co-prime antenna array consists of two sub-arrays on the same axis [22]. The first ULA consists of M_1 elements, with a distance of $M_2\lambda/2$ between each element, whereas the second ULA consists of M_2 elements, with a distance of $M_1\lambda/2$ between each element. The parameters M_1 and M_2 should be chosen as co-prime integers, meaning they have no common factors other than unity [23]. Since the first sensor is shared between the two sub-arrays, the total number of elements in the array is $M_1 + M_2 - 1$.

Moreover, the steering matrix for sub-array number k is then comprised of n steering vectors:

$$\boldsymbol{a}_k(\phi_i) = \left[1, e^{-jM_{\tilde{k}}\pi\cos(\phi_i)}, \ldots, e^{-j(M_k-1)M_{\tilde{k}}\pi\cos(\phi_i)}\right]^T, \qquad \left(k + \tilde{k} = 3\right). \quad (2.75)$$

Due to the violation of the spatial Nyquist criterion for each sub-array ($M_1\lambda/2 > \lambda/2$, $M_2\lambda/2 > \lambda/2$), there exist equivalent angles that will generate the same steering vector than the true DOA. To show this, consider a virtual array with M_k elements and half-wavelength spacing. To find the equivalent angles for this array that will deliver identical steering vectors for the sparse array, we take the M_kth roots of the sparse exponents, i.e., $-j\pi\cos(\phi_{k,i}^{eqv}) = -j\pi\cos\phi_i + j2\pi n_k/M_{\tilde{k}}$, where n_k is any integer. The above result is due to the periodicity of the complex exponential function, having a period $2\pi j$. The relationship between the equivalent and true angles for the two sub-arrays can be found as

$$\begin{aligned} \cos\left(\phi_{1,i}^{eqv}\right) &= \cos(\phi_i) + \frac{2n_1}{M_2}, \qquad n_1 \in \mathbb{Z}, \\ \cos\left(\phi_{2,i}^{eqv}\right) &= \cos(\phi_i) + \frac{2n_2}{M_1} \qquad n_2 \in \mathbb{Z}. \end{aligned} \quad (2.76)$$

Even though n_1 and n_2 could be any integers, it is limited by the fact that $\cos\left(\phi_{1,i}^{eqv}\right)$ has to lie between -1 and 1. Because M_1 and M_2 are co-prime, the only term that will coincide in the sets of both sub-arrays are the true terms $\cos(\phi_i)$. Therefore, a search algorithm is needed to match these terms, and can become computationally expensive if M_1 and/or M_2 are large.

When the number of incoming signals is more than one, the individual sub-arrays might return the same false angle, giving the impression that another signal is present. This occurrence is rare, but is a noteworthy drawback of the co-prime array configuration. Fig. 2.3 shows an example of a co-prime array setup [24].

2.4.2 Minimum redundancy arrays (MRAs)

The aim of the MRA is to achieve the maximum possible resolution with the minimal redundant spacings [25]. If we consider a ULA consisting of 6 elements, a spatial lag of 3 is caused by any of the antenna pairs $\{0, 3\}, \{1, 4\}, \{2, 5\}$

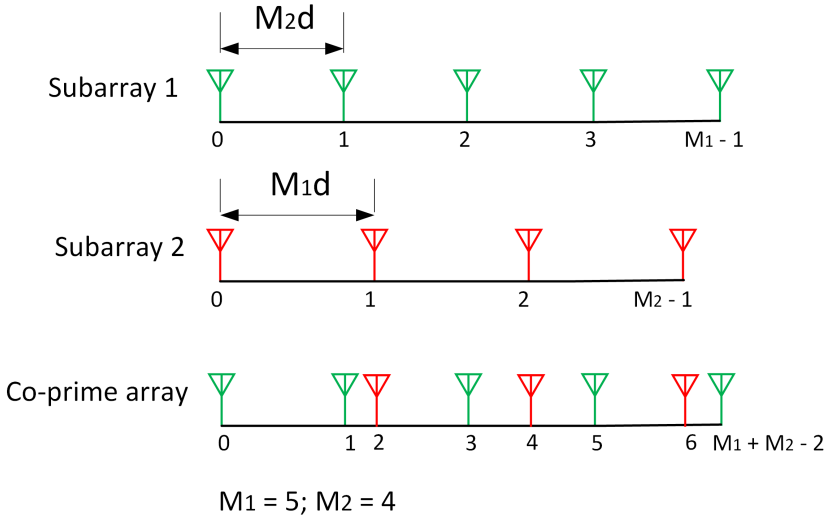

Figure 2.3: Co-prime sparse array setup, with $M_1 = 5$ and $M_2 = 4$.

or $\{3, 6\}$. This redundancy is reduced by selecting only a few elements of a ULA to ensure that there exists only one pair of elements that correspond to each spacing between zero and a maximum number [26]. It has been proven in [27] that there exist four arrays that contain zero redundancy: the first is the single-element array; the other three consist of one pair of element pairs for each multiple of unit spacing, from zero to the distance between the first and last elements. This is illustrated in Fig. 2.4.

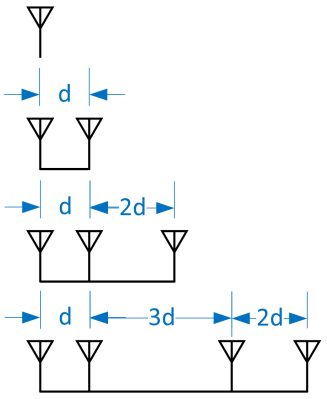

Figure 2.4: The four possible arrays that have zero redundant spacings. For each array, there exists only one pair of elements for each possible spacing between two distinct elements.

The redundancy r can be quantified by the equation

$$r = \frac{\frac{1}{2}N(N-1)}{N_{max}}, \tag{2.77}$$

Table 2.1: The number of pairs for each spacing for the MRA in Fig. 2.6

Spacing between pairs	1	2	3	4	5	6	7	8	9
Number of pairs	2	1	1	1	1	1	1	1	1

where N is the number of elements, and N_{max} is the maximum multiple of unit spacing d that ensures all multiple spacings smaller than N_{max} are realised by an element pair. Fig. 2.5 shows an example of an MRA, and Table 2.1 lists the number of element pairs for each possible spacing. For this array, $N = 5$ and $N_{max} = 9$, resulting in a redundancy metric of $r = 1.11$. A disadvantage of

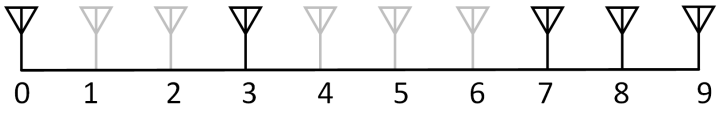

Figure 2.5: An example of an MRA with redundancy $r = 1.11$.

the MRA is that its angular resolution can only be increased by increasing the number of elements and then rearranging the configuration to optimise it [25].

2.4.3 Nested arrays

The main appeal of the nested array is its ability to detect more signals than there are sensors [28]. The degrees of freedom (DOF) achieved by these arrays are $O(M^2)$, where M is the number of antenna elements.

The concept behind the nested array relies on multiple ULAs of which the elements are intertwined. A two-level nested array contains two ULAs: the first one having a inter-element spacing of d_1, and the second one having an inter-element spacing of $d_2 = (M_1 + 1)d_1$. This means the set of element locations for ULA 1 is $S_1 = \{md_1,\ m = 1, 2, \ldots, M_1\}$, and for ULA 2 $S_2 = \{n(M_1 + 1)d_1,\ n = 1, 2, \ldots, M_2\}$ [29]. An example setup of a nested array is shown in Fig. 2.6.

2.5 Conclusion

This chapter discussed the formulation of the problem to be solved by DOA estimation methods. We described a few of the methods commonly used in dense array configurations. The idea of sparse arrays was also introduced, mentioning the advantages gained by spacing elements further than a half-wavelength apart. These arrays violate the spatial Nyquist criterion, however, and deliver aliased results from which the true angles of arrival need to be recovered. A few existing sparse configurations that resolve this problem were presented.

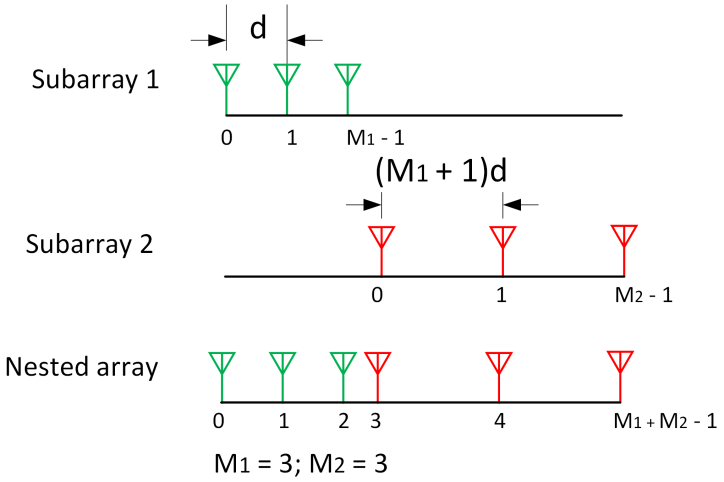

Figure 2.6: An example of a nested array, with $M_1 = M_2 = 3$.

In the next chapter, we will present the DOA estimation method named VEXPA. This method uses a chosen existing DOA estimation method and builds on it to allow the use of sparse arrays.

Chapter 3

Validated Exponential Analysis (VEXPA)

The VEXPA method is a DOA estimation method for sparse arrays. It should be noted that it is not meant to act as an alternative to other DOA estimation methods, but rather as a supplementary estimation technique to these methods to mitigate the violation of the spatial Nyquist criterion. VEXPA uses any linear one-dimensional Prony-like DOA estimation method, adding the following features [1]:

- validation of the output
- automatic estimation of the number of incoming signals n
- robustness against outliers
- parallelism in the algorithm.

3.1 The Prony method

As mentioned above, the VEXPA algorithm extends any one-dimensional Prony-like DOA estimation method and builds on it. In this context, Prony-like DOA estimation methods refer to techniques that use the same key concepts to solve the problem that was first presented by de Prony in 1795 [30]. Prony's method aims to find the $2n$ parameters $\{A_i, s_i\}$ of the problem

$$f_a(t) = \sum_{i=1}^{n} A_i \exp(s_i t), \tag{3.1}$$

by sampling the data at constant intervals [31]. We write these samples as

$$f_m = f(mT), \tag{3.2}$$

where T is the sampling period. With $m = 1$, we define a new variable

$$z_i = e^{(s_i T)}. \tag{3.3}$$

The so-called Prony polynomial contains the terms z_i as roots:

$$\sum_{m=0}^{n} \alpha_m z^m = \prod_{i=1}^{n} (z - z_i). \tag{3.4}$$

If we substitute $t = mT$ in (3.1), we get

$$f_m = \sum_{i=1}^{n} A_i {z_i}^m. \tag{3.5}$$

Using the relationships in (3.4) and (3.5), we obtain the following result,

$$\begin{aligned} \sum_{m=0}^{n} f_{k+m}\alpha_m &= \sum_{m=0}^{n} \left\{ \sum_{i=1}^{n} A_i {z_i}^{k+m} \right\} \alpha_m \\ &= \sum_{i=1}^{n} A_i {z_i}^k \left\{ \sum_{m=0}^{n} \alpha_m {z_i}^m \right\} = 0, \quad k = 0, ..., n-1. \end{aligned} \tag{3.6}$$

Thereafter, the coefficients α_m are retrieved by solving the linear set of equations

$$\sum_{j=0}^{n-1} f_{k+j}\alpha_m = -f_{k+n}. \tag{3.7}$$

The roots of the polynomial (3.1) are equal to the parameters z_i, which can be used to find s_i by the relationship

$$s_i = \frac{1}{T} \ln z_i. \tag{3.8}$$

Whereas this original Prony method relies on time-sampled data, the DOA estimation methods that adapt the Prony method use spatial-sampled data, where each sample is produced by an antenna element. Moreover, where the original Prony method requires samples with a constant sampling interval, the DOA problem requires the antenna elements to be spaced equidistantly.

3.2 VEXPA sparse array setup

The concept of the VEXPA DOA estimation method rests on two sparse sub-ULAs. These two ULAs each consist of a subset of antenna elements from a virtual dense ULA that satisfies the Nyquist criterion. The selection of

elements is dependent on two parameters: σ, referred to as the scale parameter, and ρ, known as the shift parameter.

If we consider the samples f_m of the virtual dense ULA with M elements, the first sub-ULA uses the samples $f_{m\sigma}$, and the second sub-ULA uses the samples $f_{m\sigma+\rho}$. This means that the distance between elements of the first sub-ULA is σd, and the second sub-ULA is identical to the first, but shifted with a distance of ρd [7]. The scale and shift parameters $\sigma \in \mathbb{N}_0$ and $\rho \in \mathbb{Z}_0$ should be co-prime, meaning that the Greatest Common Denominator (GCD) of σ and ρ is 1. This requirement is further discussed in Section 3.5.

The notations M_σ and M_ρ are used for the number of elements in the first and second sub-ULAs respectively, with the requirement that $M_\sigma \geq 2n$, $M_\rho \geq n$.

The setup is illustrated in Fig. 3.1.

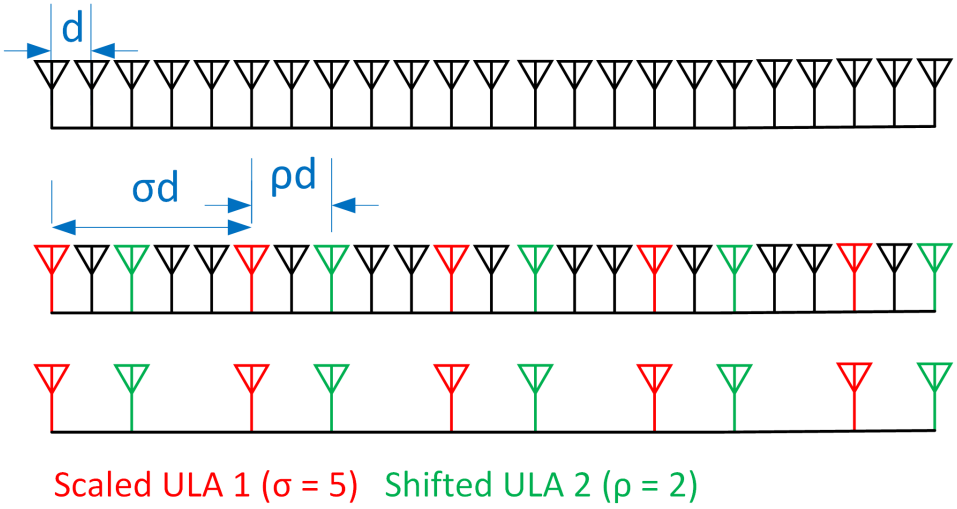

Figure 3.1: VEXPA co-prime sparse array setup. The top ULA is the virtual dense array, with $d < \lambda/2$. Furthermore, the middle array highlights the chosen elements for the scaled and shifted ULAs. The red (green) elements belong to ULA 1 (ULA 2), with a spacing of σd. ULA 2 is separated from ULA 1 by a distance ρd. The bottom array shows the resulting co-prime setup.

Next, we will discuss how we get the base terms from the antenna samples of the co-prime setup.

3.3 Retrieval of base terms Ψ_i^σ and Ψ_i^ρ

In estimating the base terms, the two sub-ULAs are treated mutually exclusive with regards to their samples. Furthermore, where the virtual dense array has a uniform spacing of d and samples f_m, the first sub-ULA has a spacing of

σd. This results in the argument within the exponent of Ψ_i, defined in (2.17), being scaled by a factor of σ. This means that the samples $f_{m\sigma}$ can be written as

$$f_{m\sigma} = \sum_{i=1}^{n} \alpha_i \Psi_i^{m\sigma} = \sum_{i=1}^{n} \alpha_i \left(\Psi_i^{\sigma}\right)^m, \quad m = 0, ..., M_\sigma - 1. \tag{3.9}$$

Note that, as in Section 2.3.4, we consider each snapshot individually, and the samples are thus independent of time.

In a similar fashion, the samples of the second, shifted ULA can be written as

$$f_{m\sigma+\rho} = \sum_{i=1}^{n} \alpha_i \Psi_i^{m\sigma+\rho} = \sum_{i=1}^{n} \left(\alpha_i \Psi_i^{\rho}\right) \left(\Psi_i^{\sigma}\right)^m, \quad m = 0, ..., M_\rho - 1. \tag{3.10}$$

The values of the first ULA base terms Ψ_i^σ are found by using any DOA estimation method such as the Matrix-Pencil method, ESPRIT etc. The chosen method is referred to as the underlying DOA method of VEXPA.

Thereafter, the coefficients α_i can be found by using the base terms Ψ_i^σ and samples $f_{m\sigma}$ to solve the Vandermonde structured linear system

$$\begin{bmatrix} 1 & 1 & \dots & 1 \\ \Psi_1^\sigma & \Psi_2^\sigma & \dots & \Psi_n^\sigma \\ \vdots & \vdots & \ddots & \vdots \\ \Psi_1^{\sigma(M_\sigma-1)} & \Psi_2^{\sigma(M_\sigma-1)} & \dots & \Psi_n^{\sigma(M_\sigma-1)} \end{bmatrix} \begin{bmatrix} \alpha_1 \\ \alpha_2 \\ \vdots \\ \alpha_n \end{bmatrix} = \begin{bmatrix} f_0 \\ f_{1\sigma} \\ \vdots \\ f_{(M_\sigma-1)\sigma} \end{bmatrix}. \tag{3.11}$$

Comparing (3.9) and (3.10), it is observed that both systems share the same base terms Ψ_i^σ albeit with different coefficients. Where the samples of ULA 1 are used to find the coefficients α_i, the Vandermonde system of the ULA 2 samples deliver the coefficients $\alpha_i \Psi_i^\rho$:

$$\begin{bmatrix} 1 & 1 & \dots & 1 \\ \Psi_1^\sigma & \Psi_2^\sigma & \dots & \Psi_n^\sigma \\ \vdots & \vdots & \ddots & \vdots \\ \Psi_1^{\sigma(M_\rho-1)} & \Psi_2^{\sigma(M_\rho-1)} & \dots & \Psi_n^{\sigma(M_\rho-1)} \end{bmatrix} \begin{bmatrix} \alpha_1\Psi_1^\rho \\ \alpha_2\Psi_2^\rho \\ \vdots \\ \alpha_n\Psi_n^\rho \end{bmatrix} = \begin{bmatrix} f_0 \\ f_{1\rho} \\ \vdots \\ f_{(M_\rho-1)\rho} \end{bmatrix}. \tag{3.12}$$

Once we have retrieved the coefficients $\alpha_i \Psi_i^\rho$, the base terms Ψ_i^ρ can be computed by dividing each coefficient with α_i. Since the samples of the second ULA are only used to calculate the coefficients and not the base terms as for ULA 1, the number of elements in ULA 2 need only be half that of ULA 1, i.e., $M_\sigma \geq 2n$ and $M_\rho \geq n$.

The following subsection highlights one useful attribute of the VEXPA algorithm, namely that satisfactory results can be computed even when the number of incoming signals is unknown.

3.4 Estimating the number of incoming signals

The maximum number of DOAs that can be determined by ULA 1 is $M_\sigma/2$. Therefore, we can overestimate the number of signals by choosing an integer N in the interval $[n, M_\sigma/2]$. Thereafter, the underlying DOA estimation method is performed to calculate the base terms $\Psi_1^\sigma, ..., \Psi_N^\sigma$, of which n are true, and $N - n$ are spurious. Consequently, by overestimating the number of signals, the size of the base term matrix in (3.11) is enlarged from $M_\sigma \times n$ to $M_\sigma \times N$, and the coefficient matrix from $n \times 1$ to $N \times 1$. The same expansion applies to the matrices in (3.12), allowing N base terms $\Psi_1^\rho, ..., \Psi_N^\rho$ to be computed. The integer N, and in turn the number of elements M, should ideally be chosen as large as possible [7].

In order to calculate the n true base terms, Padé approximation theory and cluster analysis can be used. These two approaches are presented in the following two subsections.

3.4.1 Padé approximation

A formal power series can be constructed by the samples f_m as

$$R(z) = \sum_{m=0}^{\infty} f_m z^m. \tag{3.13}$$

Substituting the definition of samples f_m yields

$$\begin{aligned} R(z) &= \sum_{m=0}^{\infty} \left(\sum_{i=1}^{n} \alpha_i \Psi_i^m \right) z^m \\ &= \sum_{i=1}^{n} \alpha_i \left(\sum_{m=0}^{\infty} \Psi_i^m z^m \right) \\ &= \sum_{i=1}^{n} \frac{\alpha_i}{1 - \Psi_i z}. \end{aligned} \tag{3.14}$$

This shows us that the power series $R(z)$ has the form of a rational function of degree $n - 1$ in the numerator and n in the denominator. In the noise-free case, the $[n-1, n]_R$ Padé approximant recovers this rational function exactly. In the case of an overestimated approximant, of degree $N-1$ in the numerator and N in the denominator, with $N > n$, all additional poles and zeros would cancel out.

In the noisy case, however, the power series $R(z)$ becomes

$$R(z) + \epsilon(z) = \sum_{m=0}^{\infty} (f_m + \epsilon_m) z^m. \tag{3.15}$$

The added noise results in $N - n$ unwanted pole-zero combinations for the Padé approximant $[N-1, N]_{R+\epsilon}$, as the additional zeros do not cancel the poles perfectly when noise is added. These zero-pole pairs are referred to as Froissart doublets [7]. For each different realisation of noise, the $N-n$ spurious poles are random, while the n true poles remain stable. The randomness of the additional poles gives one a way to distinguish the signals from the noise. Cluster analysis is therefore applied to the base terms, which are the poles of (3.14), found by considering multiple snapshots, to identify the stable poles.

3.4.2 Cluster analysis

In order to apply cluster analysis to separate the signals from the noise, the results from multiple snapshots are used, each snapshot delivering N base terms Ψ_i^σ and Ψ_i^ρ. The true base terms will form clusters, while the spurious ones will be randomly scattered. As there are n stable poles, the clustering algorithm should find n clusters.

The Density-based Spatial Clustering of Applications with Noise (DBSCAN) is an example of a clustering algorithm [32]. In this algorithm, clusters are defined by two parameters:

- μ: The minimal number of points within the neighbourhood of a certain point in order for it to be considered a cluster.
- δ: The distance defining the size of a neighbourhood.

A larger μ means that a larger fraction of the snapshot results needs to be in the same vicinity to be accepted as a cluster, increasing the certainty thereof. On the other hand, if μ is much smaller than the total number of snapshots, the presence of outliers is assumed, and these outliers are not included in the cluster.

In addition, a larger δ results in a wider cluster, which is useful for signals with a lower signal-to-noise ratio (SNR), as the noise will cause the true base terms to be spread further from the cluster core point.

The resulting base terms, Ψ_i^σ and Ψ_i^ρ found by multiple snapshots create two sets: A_σ for ULA 1, and A_ρ for ULA 2. Because of the shared Vandermonde system in (3.9) and (3.10), each element in A_σ is automatically matched to another in A_ρ. The clustering method is first applied to A_σ, after which the clusters that were found are validated by a specified subset of A_ρ. In the case that there are K snapshots, A_σ contains KN elements that are fed into the clustering method. Thereafter, a set C_σ is created, containing the elements of A_σ that form a cluster. The elements in set A_ρ corresponding to those in C_σ are subsequently fed into the clustering method. After the sets A_σ and A_ρ have undergone the clustering, three scenarios are possible:

1. A cluster C_σ is found, containing a valid number of elements in A_σ. The elements in A_ρ that are matched to these elements also form a cluster,

C_ρ. The centres of these two clusters are accepted to be Ψ_i^σ and Ψ_i^ρ. This case is illustrated in Fig. 3.2.

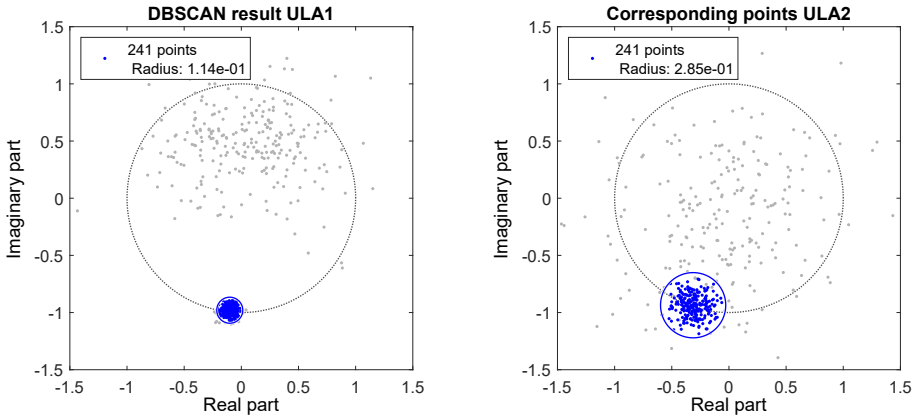

Figure 3.2: A cluster C_σ is formed by the results of ULA 1. A cluster C_ρ is also formed by the results of the corresponding snapshots of ULA 2.

2. A cluster C_σ is found, containing a valid number of elements in A_σ. The elements in A_ρ that are matched to these elements, however, do not form a cluster. The cluster C_σ is then discarded, and no Ψ_i^σ or Ψ_i^ρ are retrieved. This case is illustrated in Fig. 3.3.

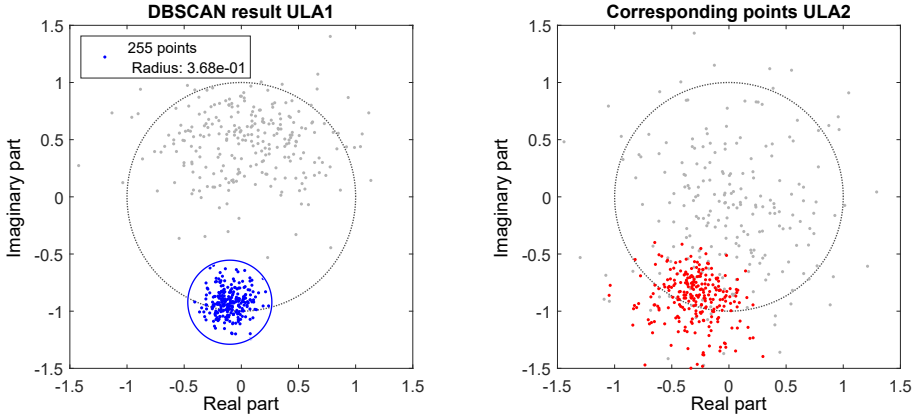

Figure 3.3: A cluster is formed by the results of ULA 1. The results of the corresponding snapshots of ULA 2 do not, however, form a cluster, and are discarded. As a result, no base terms are retrieved.

3. A cluster C_σ is found, containing a valid number of elements in A_σ. Some of the elements in A_ρ that are matched to these elements also form a cluster, C_ρ, while the remaining elements are treated as outliers and

are disregarded. The centres of the n clusters are accepted to be Ψ_i^σ and Ψ_i^ρ. This case is illustrated in Fig. 3.4.

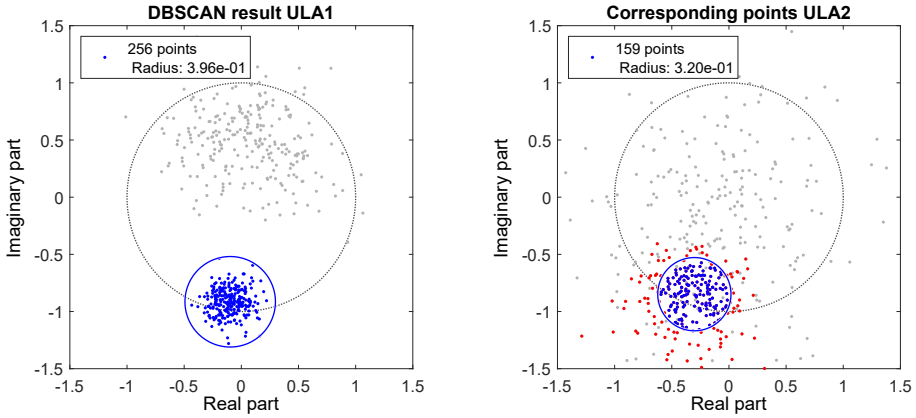

Figure 3.4: A cluster is formed by the results of ULA 1. Some of the results of the corresponding snapshots of ULA 2 form a cluster, the remaining points are discarded.

Thus, the number of incoming signals n can be regarded as the number of clusters found in A_σ and validated by A_ρ. Now suppose we have two sub-ULAs, both with 12 elements. The maximum number of signals that can be detected by this setup is $n_{max} = M_\sigma/2 = 6$, and therefore we set $N = 6$, solving for N base terms. The number of snapshots is $2^8 = 256$, meaning that $KN = 1536$ points are used. If the actual number of incoming signals is four, we expect the clustering method to return four clusters, with the remaining base terms scattered. This example is portrayed in Fig. 3.5. We can clearly see four clusters found using the results of ULA 1, which are then validated by the corresponding data of ULA 2.

Now that we have estimated the base terms Ψ_i^σ and Ψ_i^ρ, the next step is to calculate Ψ_i from these. This will be explained in the next section.

3.5 Using the aliased results to find the true DOAs

After cluster analysis is performed, the values of Ψ_i^σ and Ψ_i^ρ are known. Thereafter, in order to find Ψ_i, from which the DOAs can be readily computed, we will have to obtain the σth and ρth roots of these exponents. Due to the

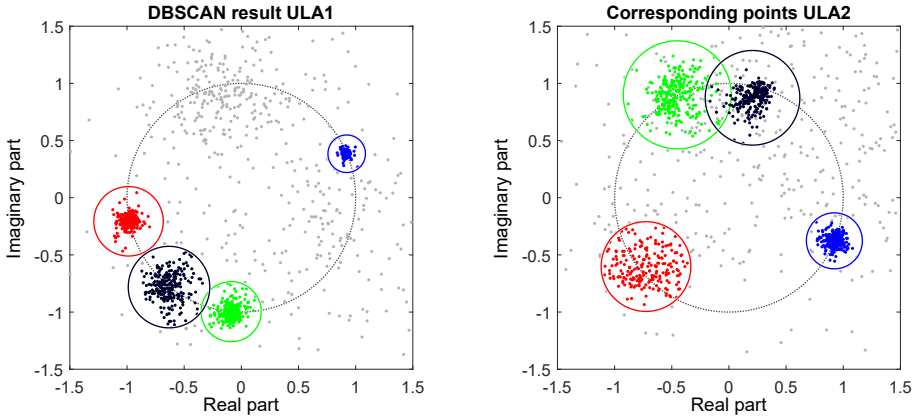

Figure 3.5: Determining the number of incoming signals n through cluster analysis. Four clusters are formed by the results of ULA 1, which are validated by the results of ULA 2. The grey dots are treated as outliers and are ignored. The centroid of each cluster are accepted as the values for Ψ_i^{σ} and Ψ_i^{ρ}, $i = 1, \ldots, 4$.

sparseness of both sub-ULAs, multiple solutions exist:

$$\begin{aligned} \Psi_i &= (\Psi_i^{\sigma})^{\frac{1}{\sigma}} \\ &= \exp\left(\psi_i d\sigma\right)^{\frac{1}{\sigma}} \\ &= \left\{ \exp\left(\psi_i d + \frac{2\pi j}{\sigma}\ell\right) : \ell = 0, \ldots, \sigma - 1 \right\}. \end{aligned} \tag{3.16}$$

In a similar fashion, we find the possible base terms of ULA 2:

$$\begin{aligned} \Psi_i &= (\Psi_i^{\rho})^{\frac{1}{\rho}} \\ &= \exp\left(\psi_i d\rho\right)^{\frac{1}{\rho}} \\ &= \left\{ \exp\left(\psi_i d + \frac{2\pi j}{\rho}k\right) : k = 0, \ldots, \rho - 1 \right\}. \end{aligned} \tag{3.17}$$

From (3.16) and (3.17), it becomes clear why the scale and shift parameters should be chosen as co-prime. As the largest positive integer that can be divided into both σ and ρ is one, the only Ψ_i that will appear in both sets will be the true one, $\Psi_i = \exp(\psi_i d)$, when $l = 0$ and $k = 0$. Fig. 3.6 shows the possible base term values found by two sub-ULAs, with $\sigma = 11$, $\rho = 5$. The true DOA is 90°, relating to a base term of $\Psi = 1$. This is indeed the value that belongs to both sets of solutions, which can be seen by the point of intersection of the red cross and blue circle in Fig. 3.6.

Due to the shared Vandermonde systems, we know which Ψ_i^{σ} correspond to which Ψ_i^{ρ} for each signal. In this regard, VEXPA has an advantage over the co-prime sparse configuration (see Section 2.4.1).

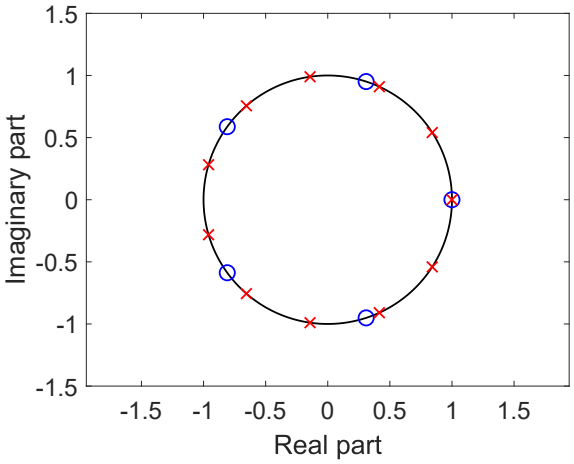

Figure 3.6: Base term solution sets from two sparse ULAs ($\sigma = 11, \rho = 5$). The red crosses indicate the solutions of the scaled ULA 1, while the blue circles indicate the solutions of the shifted ULA 2. The intersection of solutions indicates the correct base term (for $\phi = 90°$).

When the incoming data is noisy, the true Ψ_i will not be exactly equal for both sets. In this case, the points that are closest to each other are picked. It is worthwhile to note that if σ and ρ are large, then more candidate solutions will exist, meaning the solutions lie closer together on the unit circle. This will cause difficulty in identifying the true solution. Hence, the parameters must therefore be chosen as small as the desired angular resolution would allow [7].

Once the true Ψ_i are recovered, the exponents are determined as

$$\psi_i = \frac{\log(\Psi_i)}{d}, \tag{3.18}$$

after which the DOAs can be found as

$$\phi_i = \arccos\left(\frac{j\psi_i c}{\omega}\right). \tag{3.19}$$

3.6 Base term collisions

A problem that may occur when multiple signals are incoming, is the collision of base terms Ψ_i^σ on the unit circle. This occurs as there is not a one-to-one mapping of angles of arrival to base terms (which is usually the case with dense setups). These base term collisions are thus investigated along with a possible cure being presented.

We consider two incoming signals arriving from the angles 90° and 79.08° at a frequency of 1.575 GHz. Using a co-prime array setup with virtual array spacing $d = 0.48\lambda$ and scaling parameter $\sigma = 11$, the base terms Ψ_i^σ of the

signals are equal: $\Psi_1^\sigma = \Psi_2^\sigma = 1$. This means that in the step (3.11) to solve for the coefficients, a single, faulty, coefficient is retrieved, equal to $\alpha_1 + \alpha_2$.

It is still possible to recover the correct base terms from the collided base terms, if additional antenna samples are used. Hence, a new parameter, R, is introduced, where R indicates an additional number of systems of the form (3.12) to be solved. Thus, the new set of equations becomes

$$f_{m\sigma+r\rho} = \sum_{i=1}^{n} \alpha_i \Psi_i^{m\sigma+r\rho} = \sum_{i=1}^{n} \left(\alpha_i \Psi_i^{r\rho}\right) \left(\Psi_i^\sigma\right)^m, \quad r = 0, ..., R-1. \tag{3.20}$$

Where we usually have two sub-ULAs, we now have the original scaled ULA 1, with $R-1$ shifted ULAs. Fig. 3.7 shows an example of a setup: $\sigma = 13, \rho = 5$, and $R = 4$. ULA 1 ($r = 0$) consists of four elements, while the other $R-1$ shifted ULAs only have two elements.

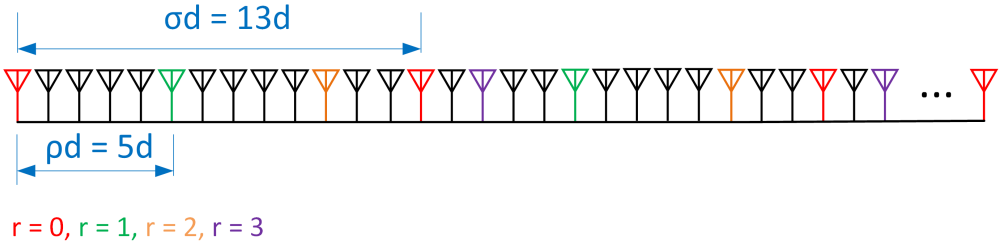

Figure 3.7: Sparse array setup with additional elements to mitigate collided base terms. The chosen elements correspond to the samples $f_{m\sigma+r\rho}$, $r = 0, ..., R-1 = 3$.

For each shift r, we solve the Vandermonde system, using the base terms Ψ_i^σ found by ULA 1 and the shifted samples $f_{m\sigma+r\rho}$ to find the values of $\alpha_i \Psi_i^{r\rho}$.

$$\begin{bmatrix} 1 & 1 & \dots & 1 \\ \Psi_1^\sigma & \Psi_2^\sigma & \dots & \Psi_n^\sigma \\ \vdots & \vdots & \ddots & \vdots \\ \Psi_1^{\sigma(M_\sigma-1)} & \Psi_2^{\sigma(M_\sigma-1)} & \dots & \Psi_n^{\sigma(M_\sigma-1)} \end{bmatrix} \begin{bmatrix} \alpha_1 \Psi_i^{r\rho} \\ \alpha_2 \Psi_i^{r\rho} \\ \vdots \\ \alpha_n \Psi_i^{r\rho} \end{bmatrix} = \begin{bmatrix} f_0 \\ f_{\sigma+r\rho} \\ \vdots \\ f_{(M_\sigma-1)\sigma+r\rho} \end{bmatrix}. \tag{3.21}$$

This system is solved R times, r taking a distinct value between 0 and $R-1$ each time. The combined results of each system give the sequence

$$\alpha_i,\ \alpha_i \Psi_i^\rho,\ \alpha_i \Psi_i^{r\rho},\ \dots,\ \alpha_i \Psi_i^{(R-1)\rho}. \tag{3.22}$$

It is critical that, for fixed i, we see this follows the same exponential model as in (3.9) [1]. We therefore use a one-dimensional DOA estimation method to solve for Ψ_i^ρ, as with Ψ_i^σ.

R should be chosen large enough to ensure all collided base terms are taken into account [1]. Specifically, at minimum, it should be at least twice the

number of collided base terms. Since the invalid base terms will be discarded by the clustering algorithm, the overestimation of R is not a problem.

However, in a practical case, taking additional samples by adding more elements to the antenna setup is not ideal. This shortcoming is discussed in a later chapter.

3.7 Summary of the VEXPA algorithm

In summary, the steps of the VEXPA algorithm are[1]:

VEXPA Algorithm Steps to find one or more DOA

1: Collect data $f_{m\sigma}$ from ULA 1 and $f_{m\sigma+\rho}$ from ULA 2.
Repeat Steps 2 to 5 for each snapshot:
2: Solve for the base terms Ψ_i^σ by using any one-dimensional DOA estimation algorithm on the samples $f_{m\sigma}$.
3: Solve for the coefficients α_i by using the structured Vandermonde linear system:
$f_{m\sigma} = \sum_{i=1}^{n} \alpha_i \left(\Psi_i^\sigma\right)^m, \quad m = 0, ..., M_\sigma - 1.$
4: Solve for the coefficients $\alpha_i \Psi_i^\rho$ by using the structured Vandermonde linear system:
$f_{m\sigma+\rho} = \sum_{i=1}^{n} \left(\alpha_i \Psi_i^\rho\right) \left(\Psi_i^\sigma\right)^m, \quad m = 0, ..., M_\rho - 1.$
5: Solve for the base terms Ψ_i^ρ by dividing $\alpha_i \Psi_i^\rho$ by α_i.
6: Use a clustering method on the set A_σ containing the results Ψ_i^σ returned by every snapshot.
7: For each cluster C_σ found in Step 6, use a clustering method on the corresponding set A_ρ containing the results Ψ_i^ρ from the snapshots matched to those of C_σ.
8: Find the centroids of the clusters found in Steps 6 and 7: these are the accepted values of Ψ_i^σ and Ψ_i^ρ. In addition, the number of clusters found are equal to the number of incoming signals n.
9: For each $i = 1, \ldots, n$ determine the sets that contain all possible solutions for $(\Psi_i^\sigma)^{\frac{1}{\sigma}}$ and $(\Psi_i^\rho)^{\frac{1}{\rho}}$.
10: Find the intersections of the sets found in Step 9: these are the accepted values of Ψ_i for $i = 1, \ldots, n$.
11: Find the exponents from the base terms by using the formula $\psi_i = \frac{\log(\Psi_i)}{d}$.
12: Find the DOAs from the exponents by using the formula
$\phi_i = \arccos\left(\frac{-j\psi_i c}{\omega}\right)$.

[1]Note that the theoretical mitigation of collided base terms is not included in these steps, as a different approach is discussed in Chapter 4

3.8 Conclusion

In this chapter, we described the VEXPA algorithm, showing how a co-prime configuration can be used to solve the aliasing problem when using existing DOA estimation methods on sparse regular arrays. We also highlighted VEXPA's ability to detect the number of incoming signals automatically.

To date much of the development on VEXPA was from the theoretical point of view, with limited attention given to the specifics of using VEXPA as a DOA estimation method in practical antenna array systems. Several non-ideal effects are present in such systems including mutual coupling, quantisation noise, signal bandwidth effects, positional errors and calibration errors. The rest of this thesis is dedicated to the description and study of these practical effects and the limitations they impose on the use of VEXPA in antenna array-based DOA.

Chapter 4

Simulated performance of VEXPA

4.1 Experimental setup

In order to test the performance of the VEXPA algorithm, we implement different simulations that introduce practical non-idealities. The various experiment conditions are given in Table 4.1, which shows the specifications of the signals, antenna configuration, and algorithm parameters; if other values are used, it will be specified in the relevant section.

One thing that should be noted is that the distance parameter δ_σ used in DBSCAN takes on a set of values. This is because multiple DBSCAN runs are performed, with the distance parameters δ_ρ fixed and δ_σ being increased until the clusters from ULA 1 are no longer validated by a cluster from ULA 2.

Table 4.1: Specifications used in simulations

(a) Signal specifications: centre frequency, fractional bandwidth, elevation angle, and signal-to-noise ratio

f_0	$b_f = b/f_0$	θ	SNR
1.575 GHz	0.05 %	90°	30 dB

(b) Antenna array specifications: virtual dense array spacing, scaling parameter, shifting parameter, and number of elements in ULA 1, ULA 2

d	σ	ρ	M_σ	M_ρ
0.48λ	11	5	6	6

(c) VEXPA algorithm specifications: number of snapshots, number of Monte Carlo runs, minimal number of points in a cluster, and distance parameter

N_t	Runs	μ_σ	μ_ρ	δ_σ	δ_ρ
$2^8 = 256$	100	$0.9N_t$	$0.6N_t$	[0.0001,0.001,0.01,0.1,0.2,0.3]	0.3

Results of the VEXPA algorithm are in some cases given as a root-mean-square error (RMSE) of the estimated angles, which is given by

$$RMSE = \sqrt{\frac{1}{nR}\sum_{r=1}^{R}\sum_{i=1}^{n}\left(\widehat{\phi}_{i,r} - \phi_i\right)^2}, \tag{4.1}$$

where $\hat{\phi}_{i,r}$ is the ith DOA estimate in the rth Monte Carlo run.

In other cases, the effectiveness is measured as a success rate, which is the number of successful trials divided by the total number of trials as a percentage. For a trial to be considered successful, the number of signals must be estimated correctly, and the RMSE of all returned angles has to be smaller than the angular resolution, as given by the Rayleigh limit in (2.11).

4.2 Narrowband noise signals

DOA estimation methods that use the output data covariance matrix, such as MUSIC, do not perform satisfactorily when the incoming signals are coherent with alike frequencies and phases. For this reason, instead of considering pure complex exponential signals with constant frequency and phase, we simulate the incoming signals as narrowband noise, where the bandwidth is a small percentage of the centre frequency [33].

If we consider multiple complex exponential signals with frequencies in the range $f_0 \pm b$ and random phases, the Central Limit Theorem suggests that the summing of these signals would result in a Gaussian random process. The frequencies of the complex exponential signals are separated by Δf, and the mean noise power of each component is $N_0\Delta f$, with N_0 the noise power density. Thus, the total mean noise power will be $2bN_0$ in the narrow frequency band and zero elsewhere. Figure 4.1 shows an illustration of the power distribution. Moreover, it is important to keep the bandwidth b sufficiently small so that the narrowband assumption mentioned in Section 2.2 is still respected. The signal bandwidth is usually expressed as a fractional bandwidth, which is defined as

$$b_f = \frac{2b}{f_0}. \tag{4.2}$$

The spectral elements of a signal representing narrowband noise lie at frequencies $f_0 \pm k\Delta f$, where k takes on values so that $k\Delta f$ lies between $-b$ and b. The total number of lines in the frequency range is then $L = \frac{2b}{\Delta f} + 1$, and the total noise power is

$$N = \sum_{k=-b}^{+b} |k\Delta f N_0|. \tag{4.3}$$

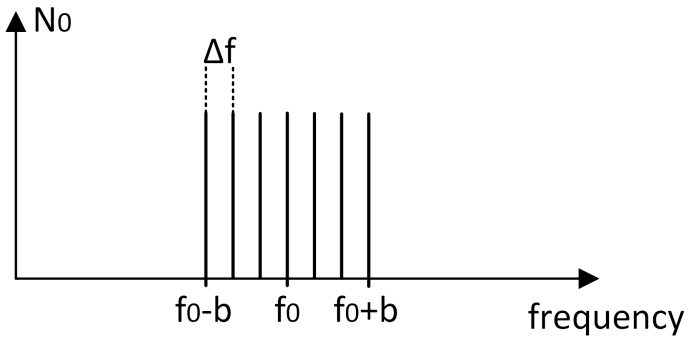

Figure 4.1: Representation of the power distribution of a narrowband noise signal.

With different phases for each frequency element, one can express the noise signal as

$$S(t) = \sum_{k=-b}^{+b} \sqrt{\frac{N}{L}} \exp\left[j\left(\left(\omega_0 + 2\pi k\Delta f\right)t + p_k\right)\right]. \tag{4.4}$$

From (2.18), we know that the array steering vectors are dependent on the signal frequencies, and therefore also need to contain the different spectral elements. At the frequency $f_0 + k\Delta f$, the base terms Ψ_i that make up the steering matrix A as defined in (2.20) are given by $\exp(\psi_i d)$, where

$$\psi_i = \frac{j\left(\omega_0 + 2\pi k\Delta f\right)\cos\phi_i}{c}. \tag{4.5}$$

The array output signal $\boldsymbol{f}(t) = A\boldsymbol{S}(t) + \boldsymbol{n}(t)$ as in (2.21) will thus change for the narrowband noise to a summation of all the spectral elements, as

$$\boldsymbol{f}(t) = \sum_{k=-b}^{+b} A_k\boldsymbol{S}_k(t) + \boldsymbol{n}_k(t). \tag{4.6}$$

Here, A_k refers to the steering matrix with the exponents ψ_i of the base terms as in (4.5) and $\boldsymbol{n}_k(t)$ is the $M \times 1$ noise vector. $\boldsymbol{S}_k(t)$ is the signal vector $\begin{bmatrix} S_1 & S_2 & \cdots & S_n \end{bmatrix}^T$ at $f_i = f_{i0} + k\Delta f$, where f_{i0} is the centre frequency of the ith signal. Specifically, $S_i(t) = \sqrt{\frac{N}{L}} \exp\left[j\left(\left(\omega_{i0} + 2\pi k\Delta f\right)t + p_k\right)\right]$.

4.3 Using Root-MUSIC as underlying method to VEXPA

As mentioned previously, VEXPA is used in conjunction with any other one-dimensional DOA estimation method. MUSIC has the advantage over other

DOA estimation methods in that it seems to deliver accurate results even with low-resolution quantised data [34]. We now investigate using MUSIC as underlying method.

Referring to Section 2.3.2, MUSIC solves the DOA problem by performing a search for the angle that minimises the MUSIC spectrum, whereas Root-MUSIC returns the base terms of the exponential analysis problem. As the VEXPA algorithm uses the base terms found by the scaled ULA, Root-MUSIC is preferred above MUSIC as underlying method. We see in (2.43) that the polynomial solved by Root-MUSIC is essentially a Prony polynomial, proving that Root-MUSIC is a Prony-like DOA estimation method.

As mentioned in Section 2.3.2, the Matrix-Pencil method can solve the DOA problem using only one snapshot of data, whereas Root-MUSIC uses the approximated covariance matrix, which is only accurate with a significant number of time samples as it is approximated by taking a temporal average of the antenna samples. Methods such as the Matrix-Pencil method, which is able to return an accurate answer using a single snapshot, is thus superior in this regard.

The most accurate estimation of the covariance matrix would mean using all possible snapshots, meaning that a single result is achieved, and the use of cluster analysis on the results is not applicable. If one still wishes to use the clustering step of VEXPA, one can divide the time-sampled data into subsets of samples. For example, if we have $2^8 = 256$ snapshots, we can choose any number of subsets, each consisting of any number of snapshots. If 256 subsets are chosen, the Root-MUSIC algorithm is performed 256 times using the snapshots of each subset. This means that 256 sets of base term results are passed to the clustering algorithm, making it identical to the case of the per-snapshot algorithms. The snapshots chosen for each subset do not have to be consecutive and can be chosen at random. If r snapshots are chosen for each subset from a total of N_t snapshots, the number of unique subsets is given by

$$\binom{N_t}{r} = \frac{N_t!}{r!(N_t - r)!}. \tag{4.7}$$

This means that, to ensure all subsets are unique, the maximum number of snapshots in each subset is $N_t - 1$, because $\binom{N_t}{N_t-1} = N_t$.

In the case of the Matrix-Pencil method, a set of base terms Ψ_i^σ is retrieved for each snapshot, after which this base term and the corresponding snapshot of ULA 2 are used in the Vandermonde system to solve for Ψ_i^ρ. Now that multiple snapshots are used in the retrieval of Ψ_i^σ, which snapshots of ULA 2 should one use in the Vandermonde system to solve for Ψ_i^ρ correctly?

To ensure an accurate calculation of Ψ_i^ρ, we solve the Vandermonde systems $f_{m\sigma} = \sum_{i=1}^{n} \alpha_i \left(\Psi_i^\sigma\right)^m$ and $f_{m\sigma+\rho} = \sum_{i=1}^{n} \left(\alpha_i \Psi_i^\rho\right) \left(\Psi_i^\sigma\right)^m$ by using the same subset of snapshots that was used to solve for Ψ_i^σ. For the case of the Matrix-Pencil

method, as only one snapshot is used, the samples $f_{m\sigma}$ and $f_{m\sigma+\rho}$ are of sizes $[1 \times M_\sigma]$ and $[1 \times M_\rho]$ respectively, but now that multiple snapshots are used, these sizes change to $[N_t \times M_\sigma]$ and $[N_t \times M_\rho]$, meaning a total of N_t sets of values calculated for Ψ_i^ρ. Thereafter, a final answer for Ψ_i^ρ is obtained by taking an average of the N_t sets.

This increase in matrix sizes translates to a significant increase in computational time, but because an average is ultimately computed, it is unnecessary to take all the snapshots of each subset in the Vandermonde system. By choosing a number of random snapshots from each subset, i.e., choosing a subset from each subset, one can speed up the computation.

Root-MUSIC, like any other algorithm that uses the covariance matrix, requires that incoming signals are uncorrelated and incoherent, because the covariance matrix becomes singular when this is not the case [8]. Multipath environments cause signals to reach the receiving antennas by more than one path, which in turn leads to received signals that are scaled and delayed versions of one another. Hence, these signals are highly correlated and coherent.

Taking these considerations into account, we proceed to investigate the results of Root-MUSIC used together with VEXPA, specifically the cases where the incoming signals are coherent, and also when the number of snapshots is fewer than desired.

Considering the effect of coherent signals, we use two complex exponential signals, incoming from angles 56° and 90°, which are 90° out of phase. For the coherent case, the signals have identical frequencies. The incoherent cases are simulated as separations of the signal frequencies which are defined as follows. If one considers a centre frequency f_0, the two signals are at frequencies $f_L = f_0 - \Delta f$ and $f_H = f_0 + \Delta f$, where Δf is chosen as a percentage of f_0. In this investigation we consider two incoherent cases, with $\Delta f = 0.001\% f_0$ and $\Delta f = 0.01\% f_0$.

In addition, the total number of snapshots and subsets are kept constant at $2^8 = 256$, while the number of snapshots in each subset N_s is either $2^5 = 32$ or $2^8 - 1 = 255$. This essentially means that the respective cases use 32 and 255 snapshots to calculate the covariance matrix.

For this simulation we specifically look at the results of Ψ_i^σ as determined by the samples of ULA 1, as these are the results that will be passed to the VEXPA algorithm. Fig. 4.2 shows the results of four different cases, where the true base terms are indicated in blue, and the returned base terms are indicated in red.

The top left figure shows the case of two signals with identical frequencies, thus coherent, with 255 snapshots used by the covariance matrix calculation. We see that even with such a large number of snapshots, inaccurate results are achieved due to the coherence of the signals.

Next, we consider the case where the signals have a 0.001% frequency separation, still with 255 snapshots. In the top right figure, we see that this

separation causes enough incoherence between the signals to deliver more accurate results.

Thereafter, the number of snapshots is reduced to 32 in the bottom left figure, keeping the frequency separation at 0.001%. The estimated base terms are in the vicinity of the correct base terms, but ideally one would wish for a more accurate estimation. This means that we should use more snapshots to approximate an accurate covariance matrix.

The bottom right figure shows the results if we increase the frequency separation to 0.01%, but keep the number of snapshots at 32. A larger frequency separation thus means fewer snapshots are needed as the signals are less coherent.

This shows that both the incoherence of the signals and the number of snapshots used are important factors to take into consideration when using Root-MUSIC as underlying method to VEXPA, but that it is indeed a possibility.

For the simulated experiments using Root-MUSIC, we choose to use narrowband noise signals with a fractional bandwidth, as defined in (4.2), of 0.05%, to ensure signal incoherence. With sufficient signal incoherence, we look at the performance when the total number of snapshots are kept constant but the number of snapshots in the two subsets differ. The total number of snapshots is 256, while the number of snapshots used in the covariance matrix (N_s) is varied from 50 to 250, and the number of snapshots used in the Vandermonde systems (N_{ss}) is expressed as a fraction of N_s. Two signals, incoming from $\phi_1 = 90°$ and $\phi_2 = 70°$ are present. The SNR of these signals is equal to 0 dB, as the necessity for a larger number of snapshots used in the covariance matrix is clearer at higher noise levels. Fig. 4.3 shows the success rate, where we can clearly see the improvement in DOA detection as the number of snapshots increase. Fewer snapshots imply a faster computation, and for this reason, we choose $N_s = 100$ and $N_{ss} = 0.5N_{ss}$ in future simulations, as a high success rate of 98% is achieved for these values.

Since Root-MUSIC requires multiple snapshots to compute the covariance matrix and solutions of the Vandermonde systems, it increases the computation time of VEXPA. The effect of the number of snapshots on computational time is quantified by performing simulations in MATLAB R2019b on an Intel(R) Core(TM) i7-8550U CPU with 32 GB RAM. The increase in snapshots leading to the increase in computation time is highlighted in Table 4.2. Hence, the use of Root-MUSIC as underlying method comes at the cost of a more computationally expensive implementation of VEXPA.

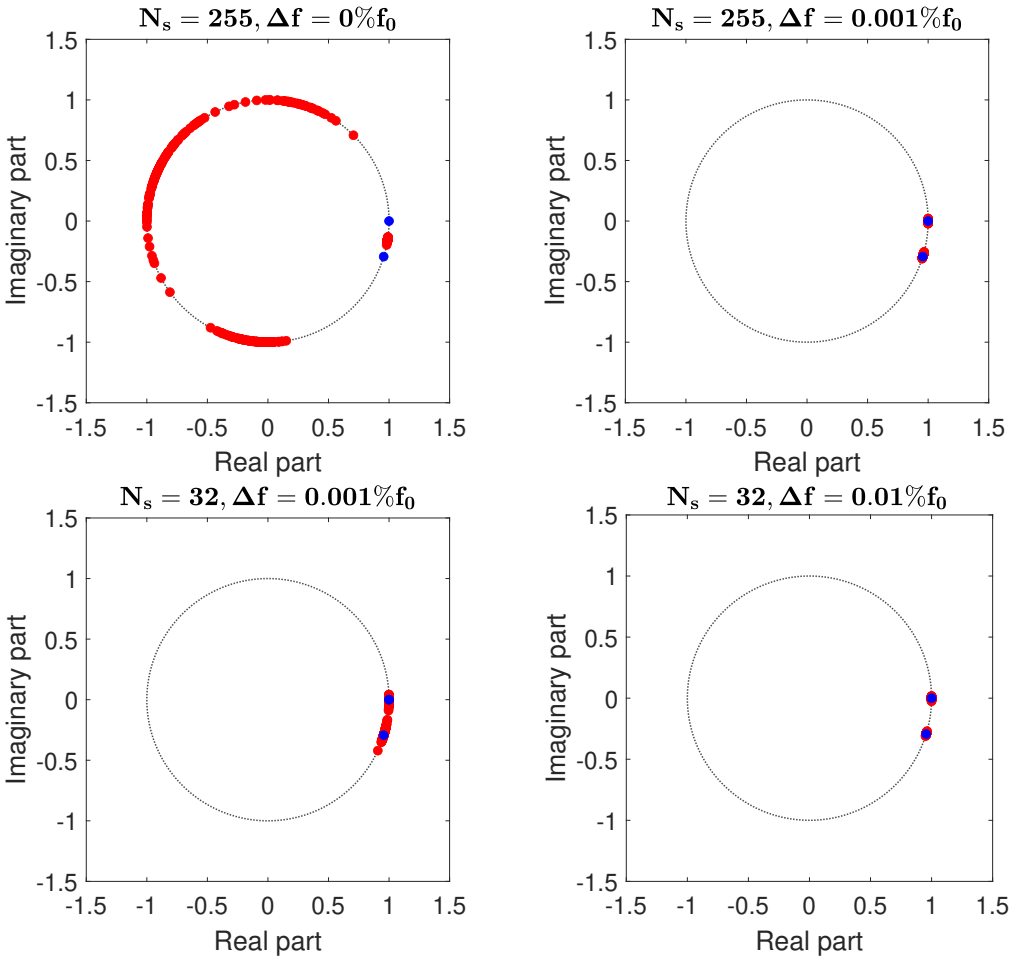

Figure 4.2: Base terms Ψ_i^σ returned by Root-MUSIC in red and true base terms in blue for four different sample sets: top left shows results of two incoming signals 90° out of phase but with identical frequencies, creating signal coherence, with 255 snapshots; top right shows results of approximated covariance matrix using 255 snapshots, with frequency separation of 0.001%. Bottom left shows results of 0.001% frequency separation with 32 snapshots; bottom right shows results of 0.01% frequency separation with 32 snapshots.

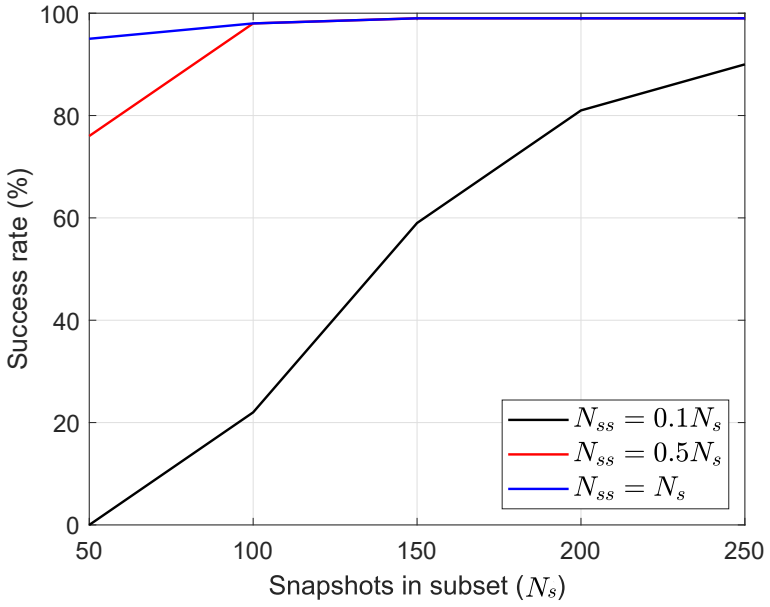

Figure 4.3: The effect of the number of snapshots used when using Root-MUSIC as underlying method to VEXPA. N_s refers to the number of snapshots in the subset used to calculate the covariance matrix, while N_{ss} is the number of snapshots in the subset used to calculate Ψ_i^ρ in the Vandermonde systems.

Table 4.2: Computational time (in seconds) of VEXPA with different underlying methods and numbers of snapshots.

	$N_t = 2^6$	$N_t = 2^8$	$N_t = 2^{10}$
Matrix-Pencil	0.085	0.19	1.05
Root-MUSIC	0.14	0.30	1.61

4.4 Sparse arrays and improved angular resolution

The biggest advantage of sparse antenna arrays versus dense arrays is the improved angular resolution. As mentioned previously, this is given by $\Delta\phi \approx \frac{\lambda}{D}$, with D the total length of the array. For a sparse array, D is much larger for the same number of antenna elements, and therefore a much higher resolution can be achieved.

To illustrate this, we consider two dense DOA estimation algorithms, as well as the sparse implementation of these algorithms by using VEXPA. Both cases use an array with 12 elements: the dense case has an inter-element spacing of 0.48λ, and the co-prime sparse array has parameters $\sigma = 11$, $\rho = 5$, ULA 1 and ULA 2 each consisting of six elements. Two arriving signals are

present, the first fixed at $\phi_1 = 45°$, and the second varied in $\phi_2 \in [30°, 44°]$. The number of snapshots is $2^8 = 256$ for both the dense and sparse cases, the SNR is constant at 30 dB, and $R = 100$ Monte Carlo runs are performed. Fig. 4.4 shows the results as the RMSE of the estimated angles.

The angular resolution of each array configuration is shown as vertical dotted lines, where it can be seen clearly that the sparse array has a smaller resolution at $\Delta\phi = 1.98°$ versus $\Delta\phi = 10.85°$ for the dense case. For the sparse case, incoming signals as close as 1.5° to each other can be detected by both algorithms, all with errors smaller than 0.02°. For the Matrix Pencil method, such small errors are only achieved by the dense case at an angular separation of about 14°. In the case of Root-MUSIC, even though the errors are small even for the dense case, the performance is improved when using a sparse configuration.

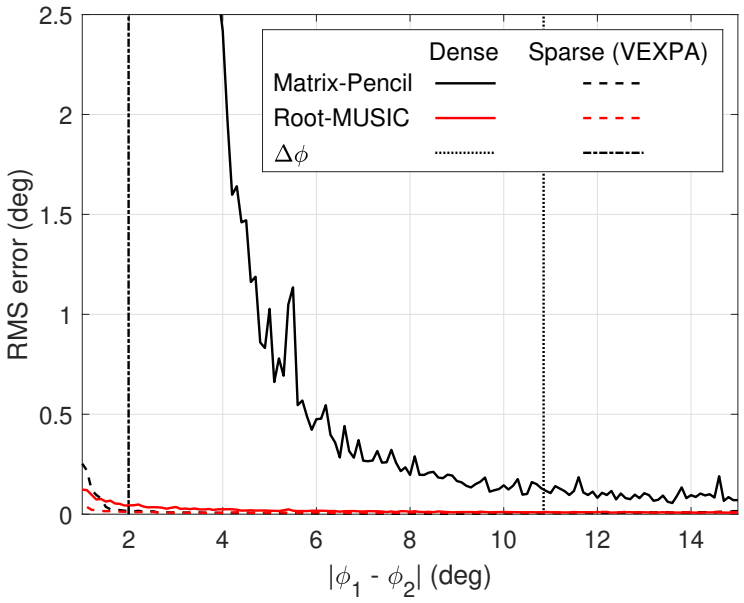

Figure 4.4: Performance of two DOA estimation methods, when applied to both a dense array and a co-prime sparse array that makes use of VEXPA. The angular resolution of each array configuration is indicated by black vertical lines. Having a smaller angular resolution, the sparse configuration is able to distinguish between signals with smaller angular separations.

We now illustrate how the angular resolution improves for the co-prime configuration when the inter-element spacing of the virtual dense array is increased, meaning a sparser array. Three values of d, the virtual dense spacing, are considered: $d = 0.09\lambda$, $d = 0.3\lambda$, and $d = 0.48\lambda$. The results are shown in Fig. 4.5, with increasing values of d from the top to the bottom graph. We can clearly see how the angular resolution improves as the array becomes sparser.

The above highlights one of the main benefits introduced by the VEXPA sparse co-prime configuration, as the array can be as sparse as practical considerations allow, and with this a high angular resolution can be achieved.

4.5 Estimation of the number of incoming signals

Section 3.4 explains how the VEXPA algorithm uses cluster analysis to estimate the number of incoming signals. In this section, we compare this approach to the traditional approach used in dense DOA estimation methods. Taking MUSIC as an example, equation (2.32) shows that the $M-n$ smallest eigenvalues of the covariance matrix are equal to the noise variance, whereas the other n eigenvalues rise up above the noise floor. This means one can identify the number of incoming signals by subtracting the multiplicity of the smallest eigenvalue from the total number of eigenvalues (i.e., the number of antenna elements). As the covariance matrix is determined by using only a finite number of snapshots, the smaller eigenvalues will not be exactly equal, and therefore the number of eigenvalues lying in the same vicinity is considered. This is achieved by considering each eigenvalue. For the ith eigenvalue σ_i, if it satisfies the inequality

$$\frac{\sigma_i}{\sigma_{max}} > 10^{-p}, \tag{4.8}$$

it is classified as part of the signal subspace, where σ_{max} is the most dominant eigenvalue, and p is the number of significant decimal digits [18]. The value n is then equal to the number of eigenvalues belonging to the signal subspace.

These two methods of estimating the number of signals are compared as follows: the VEXPA algorithm is used for the first case, assuming the maximum number of signals possible for the specific number of antennas and cluster analysis is done on the complete set of results. The second case incorporates some, but not all, of the steps of VEXPA. Specifically, the one-dimensional DOA estimation method is used on the samples of ULA 1 to solve for Ψ_i^σ, as usual. In this process, however, the number of incoming signals is estimated through the eigenvalue-counting method, with the parameter p in (4.8) chosen as 1. The base terms Ψ_i^ρ is, as with VEXPA, calculated by the Vandermonde systems, but the clustering analysis step falls away. When the Matrix-Pencil method is used, the estimation of the base terms Ψ_i^σ is performed per snapshot, after which an average of the base terms of all the snapshots is taken, replacing the cluster analysis step. When Root-MUSIC is used, the estimation of the base terms Ψ_i^σ is performed one time using all available snapshots, so an averaging step is not necessary. The number of snapshots is constant at $2^8 = 256$.

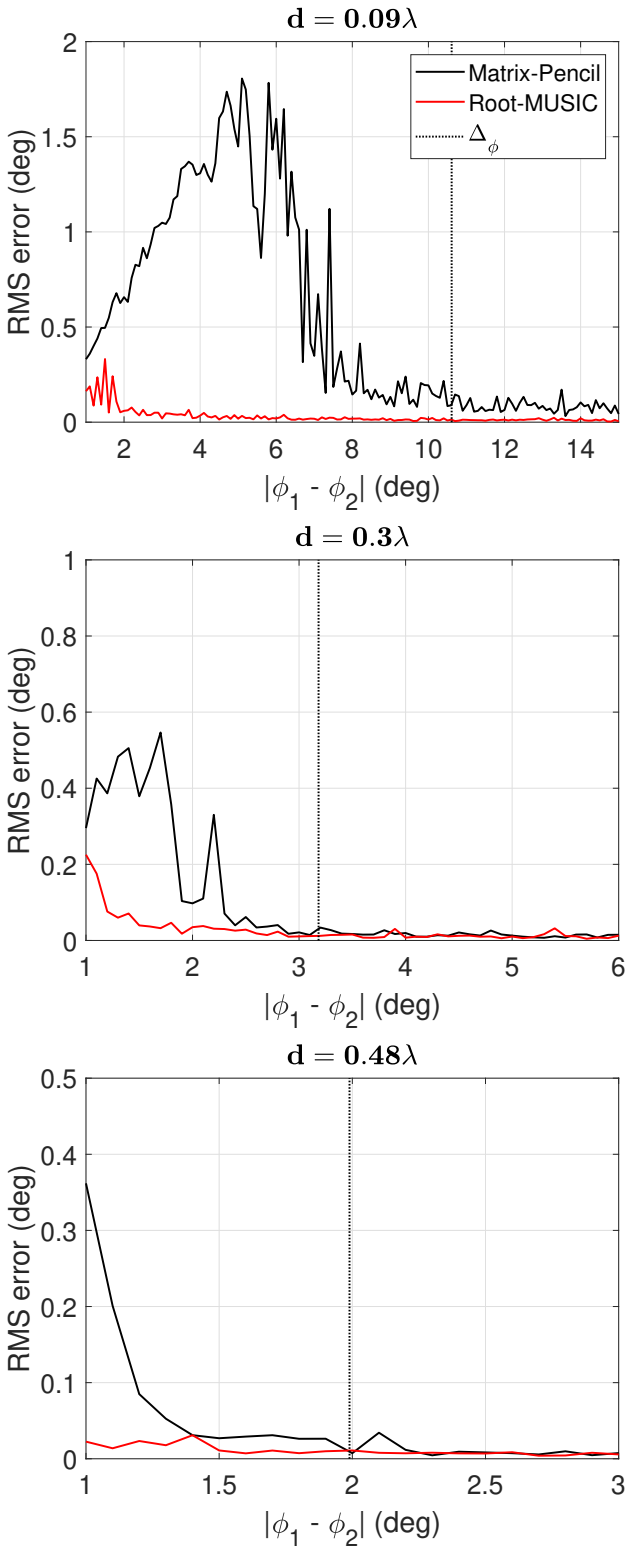

Figure 4.5: Performance of the VEXPA algorithm for three different array configurations. The top graph shows the results of an array with $d = 0.09\lambda$, the middle graph $d = 0.3\lambda$, and the bottom graph $d = 0.48\lambda$. Note the different axes for each graph. The sparser the configuration, the better the angular resolution, with minimal errors for smaller angular separations.

Now we consider an array setup with ten elements in ULA 1 and five in ULA 2. This means a maximum of five signals can be detected. Furthermore, we vary the number of signals from one to four, with the respective angles of arrival at 90°, 70°, 60° and 5°, and the SNR varied from 0 to 30 dB.

The results are shown in Fig. 4.6, where the top graph shows the results using Root-MUSIC, and the bottom shows those of the Matrix-Pencil method. For the case of Root-MUSIC, we see that a high success rate is achieved even for low SNR values, with the cluster analysis method performing slightly worse than the eigenvalue method. This can be explained by the fact that not all of the snapshots in the execution of Root-MUSIC are used to calculate the base terms Ψ_i^ρ. This leads to more scattered results in the clustering step, in turn causing the algorithm to detect fewer clusters than the true number of signals. As mentioned previously, we choose $N_s = 100$ and $N_{ss} = 50$ to decrease computational time. However, if N_s and N_{ss} were both chosen to be $2^8 - 2$, for example, more accurate results would be achieved for Ψ_i^ρ, and the correct number of clusters would be formed. The different choices of snapshots are illustrated in Fig. 4.7. The graphs show the results of the clustering step on Ψ_i^ρ, with the left graph corresponding to the higher number of snapshots.

For the case of the Matrix-Pencil method in the bottom graph, the cluster analysis seems to deliver fairly similar results independent of the number of signals, with zero success at roughly 5 dB and full success at about 15 dB SNR. The eigenvalue method, on the other hand, shows better results with fewer signals. For the cluster analysis method, the overestimation of the number of signals ensures that all possible base terms are returned, and later those that do not form clusters are discarded. On the other hand, when the number of signals is estimated per snapshot, as in the eigenvalue method, some signals can wrongly be identified as noise when their corresponding eigenvalues are smaller than the threshold value in (4.8). As the number of signals increases, it is evident that the distinction between noise eigenvalues and signal eigenvalues become vaguer.

From this, we can conclude that DOA estimation methods that are solved per snapshot can benefit from the cluster analysis method of estimating the number of signals, whereas for methods using the covariance matrix, the effect of a higher number of snapshots has a more significant impact, and both the eigenvalue method and cluster analysis method are accurate.

The work done in the above section will be included in a conference paper that is currently in preparation [35].

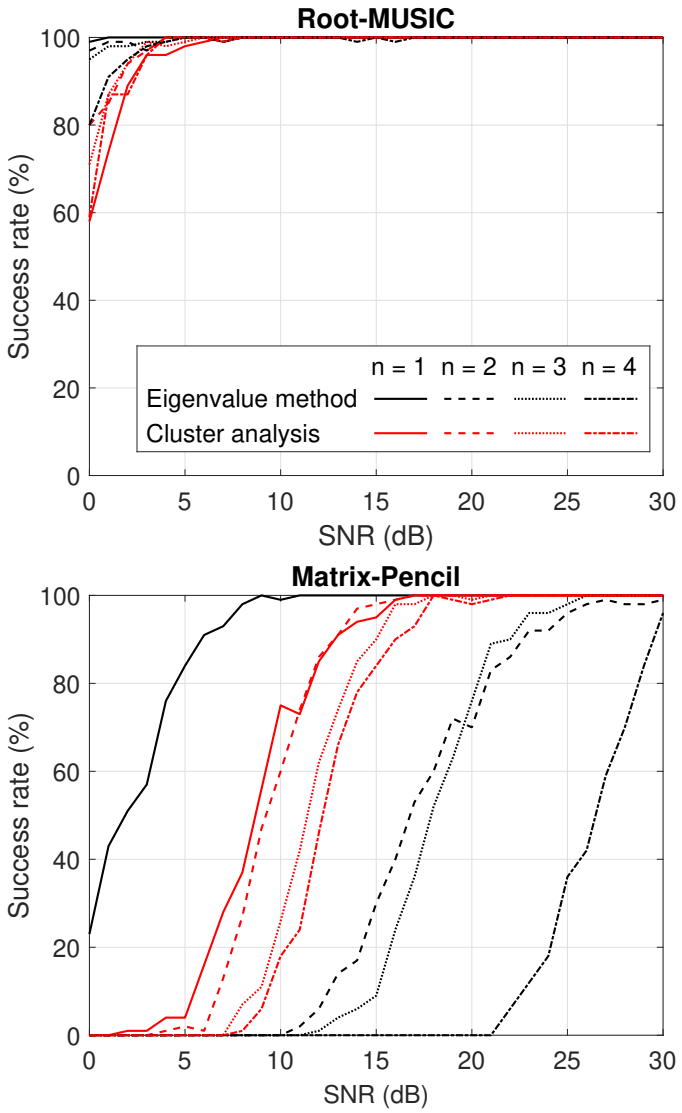

Figure 4.6: Success rate estimating the number of incoming signals by using two methods: identifying eigenvalues corresponding to the signal subspace (black), and using cluster analysis (red). The top and bottom graphs show the results using Root-MUSIC and Matrix-Pencil as underlying method to VEXPA, respectively.

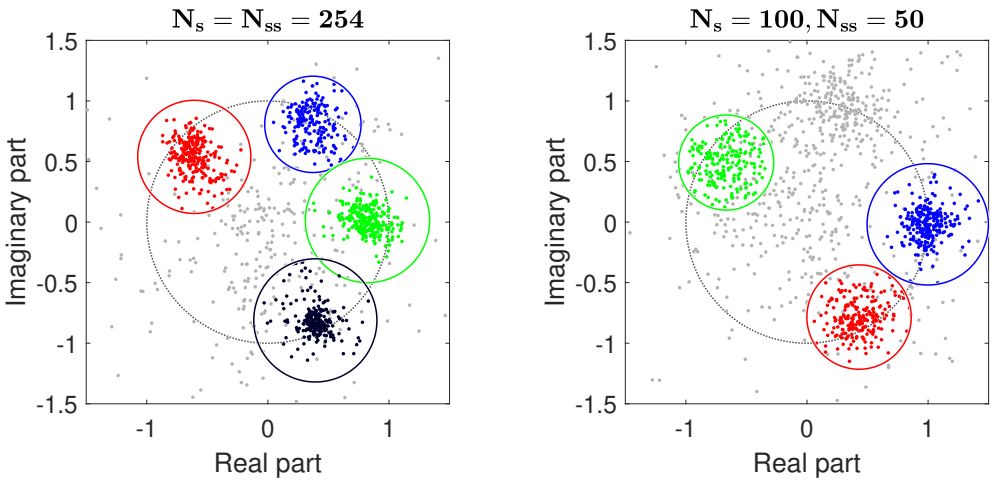

Figure 4.7: Clusters formed by Ψ_i^{ρ} when different number of snapshots are used in the subsets of VEXPA used with Root-MUSIC. The true number of signals is four. The left graph uses $N_s = N_{ss} = 2^8 - 2$ snapshots, and the right uses $N_s = 100$ and $N_{ss} = 50$. Fewer snapshots cause the results to be more scattered, and only three of the four clusters are formed.

4.6 Effects of SNR and number of snapshots

4.6.1 SNR

We now investigate the influence of noise on the VEXPA algorithm. As mentioned previously, one of the assumptions of the DOA estimation problem is that each element adds white Gaussian noise to the incoming signals, each with an equal variance σ^2. The Additive White Gaussian Noise is expressed in terms of SNR, which is defined as $\text{SNR} = 20\log_{10}(||f||_2/||\epsilon||_2)$, where $||f||_2$ and $||\epsilon||_2$ are the 2-norms of the data vector and noise vector respectively.

We vary the SNR from 0 dB to 30 dB, and consider two incoming signals from $\phi_1 = 45°$ and $\phi_2 = 45° + \Delta\phi = 46.99°$. In addition, the number of snapshots is kept constant at $2^8 = 256$. The experiment is repeated with a different realisation of the DBSCAN parameter δ. In particular, for the first experiment, it is as specified in Section 4.1: $\delta_\sigma = [0.0001, 0.001, 0.01, 0.1, 0.2, 0.3]$ and $\delta_\rho = 0.3$. For the second experiment, the parameter is slightly relaxed to allow for more noisy instances: $\delta_\sigma = [0.1, 0.3, 0.4]$ and $\delta_\rho = 0.4$. In Fig. 4.8 the RMSE of 100 Monte Carlo runs is shown, with the Rayleigh limit or angular resolution indicated by the dotted line. For the more stringent δ values, shown in the top graph, we can see that Root-MUSIC delivers results with errors smaller than the angular resolution from an SNR as low as -4 dB, while the Matrix-Pencil method only does so from an SNR of about 11 dB. It should be noted that, for SNR values below 11 dB, Matrix-Pencil does not return any angles at all.

When the δ parameter is relaxed, as shown in the bottom graph, Matrix-

Pencil returns angles from an SNR value as low as -1 dB. Here, the significance of the DBSCAN parameters becomes apparent. A bigger value of δ means that wider-spaced clusters are accepted, allowing for more noisy data to form clusters. This is helpful in the case of lower SNR values, as clusters are now found that would not be for stricter values of δ. On the other hand, for higher SNR values, this means that some outliers are included in the cluster, meaning that its centre is shifted slightly away from the true position of the base term. The result of this shift is depicted in Fig. 4.8, where the bottom graph shows returned angles from a lower SNR value, while possessing a higher RMSE. For example, at SNR = 15 dB in the top graph, Matrix-Pencil has an RMSE of about 0.1 degrees, while the same SNR value in the bottom graph has an RMSE of 0.4 degrees.

4.6.2 Number of snapshots

In Section 4.3 it was shown that a high number of snapshots is needed to estimate the covariance matrix correctly. We now investigate the effect of different numbers of snapshots on the VEXPA algorithm. In this setup the SNR is kept constant at 30 dB, and once again we consider two incoming signals from $\phi_1 = 45°$ and $\phi_2 = 45° + \Delta\phi = 46.99°$ respectively. It should be noted that the number of snapshots in the subsets used by Root-MUSIC are still kept constant at $N_s = 100$ and $N_{ss} = 50$. The number of snapshots in this case refers to the number of times an artificial snapshot is created by solving Root-MUSIC on a subset of snapshots.

Fig. 4.9 shows the RMSE of 100 Monte Carlo runs, with SNR = 30 dB and SNR = 15 dB for the top and bottom graphs, respectively. We observe that for the higher SNR value, VEXPA performs better for each iteration when more snapshots are used. On the other hand, when the data is noisier as shown in the bottom graph, the errors tend to increase as more snapshots are used for the Matrix-Pencil method. This is because more noisy snapshots lead to wider clusters with its centroids positioned incorrectly. Root-MUSIC, on the other hand, shows similar results for both realisations of noise. This indicates that Root-MUSIC is less susceptible to noise.

4.7 Quantisation errors

An important step in the data capturing process of an antenna array is the quantisation of the incoming analogue signals. This is done by an analogue-to-digital converter (ADC), with a certain number of quantisation levels [36]. Each quantisation level is represented by a binary number, which is made up of a number of bits b relating to the number of quantisation levels L by $2^b = L$. The resolution of the quantiser is then $\Delta = \frac{R}{2^{b+1}}$, where R is the range thereof. As the accuracy of the quantiser is determined by the resolution, a

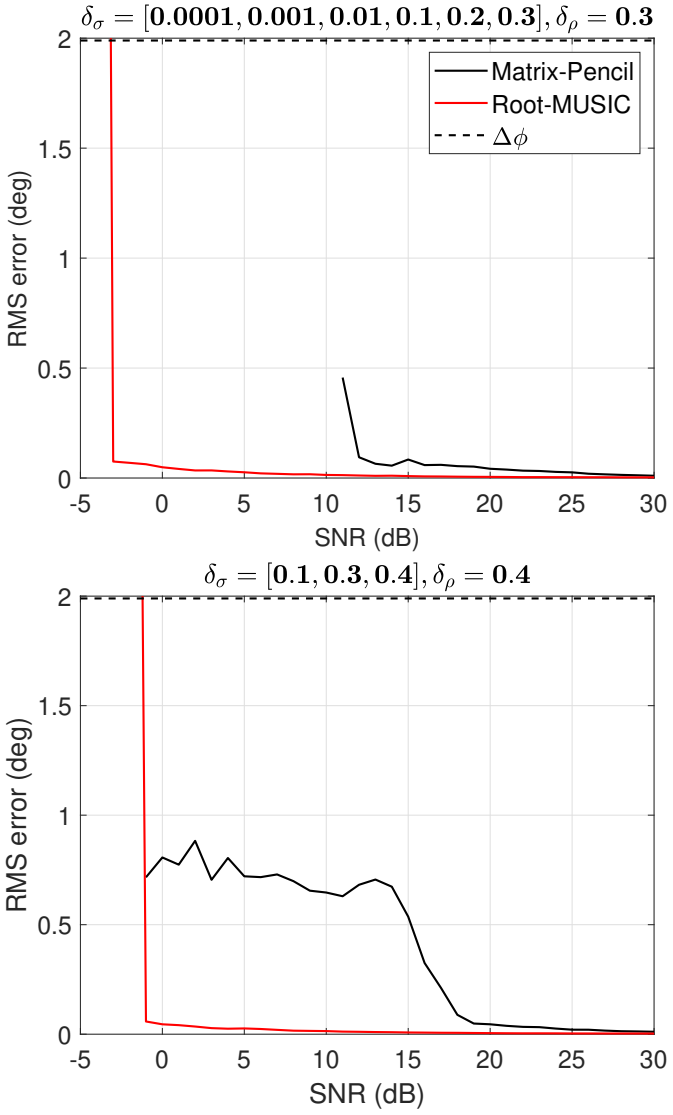

Figure 4.8: Effect of noise on VEXPA algorithm with different underlying methods. The horizontal dotted line indicates the angular resolution of the antenna array. The top graph shows results for a lower value of δ in DBSCAN than the bottom graph, meaning a more relaxed cluster analysis. We see that this translates to a lower RMSE, but also a requirement for higher SNR values in order to return angles at all.

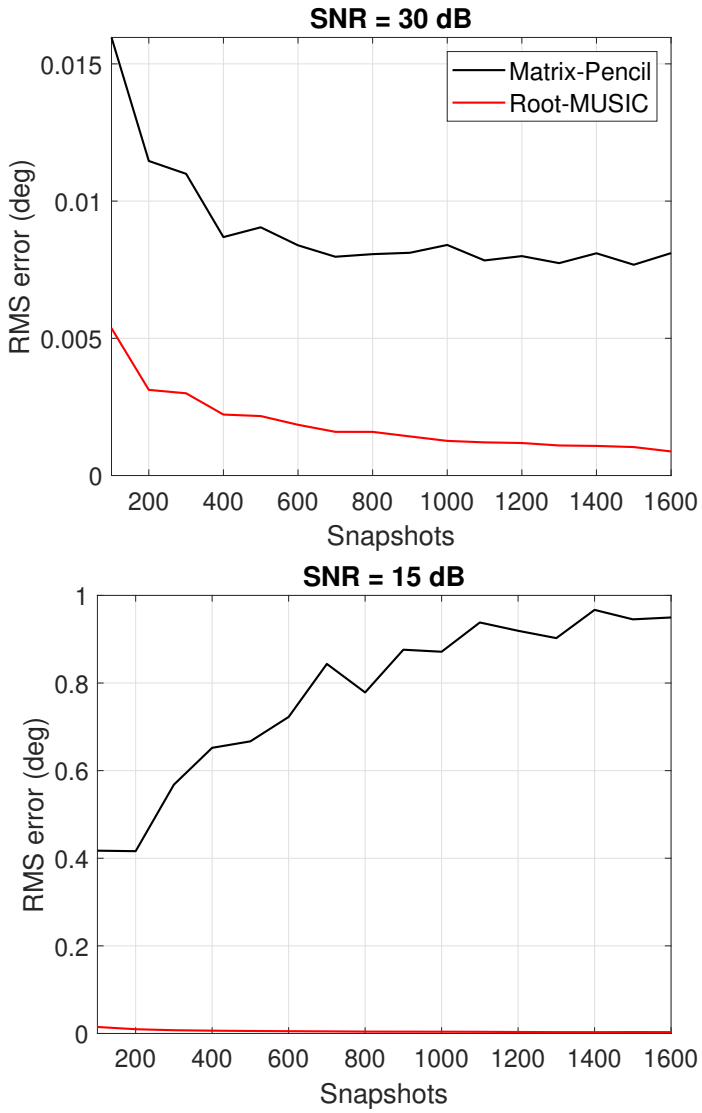

Figure 4.9: Effect of a different number of snapshots on VEXPA algorithm with different underlying methods. The SNR values for the top and bottom graph are 30 dB and 15 dB, respectively. For less noisy data, the performance of both algorithms improves with more snapshots, but as the noise is increased, the Matrix-Pencil method achieves better results with fewer snapshots.

quantisation error $e_q(n)$ is introduced. This error is quantified by the signal-to-quantisation-noise ratio (SQNR). The calculation of the SQNR is often derived as [36]

$$\text{SQNR} = 6.02b + 1.76\,\text{dB}. \tag{4.9}$$

This derivation is based on the assumption that the sampling rate satisfies the Nyquist sampling theorem. Thus, for each added bit, the SQNR is increased by 6 dB.

As higher-resolution quantisers come with the disadvantage of a higher cost and intricate circuit design [37], the use of low-resolution ADCs is desirable for antenna array applications. One-bit ADCs are especially attractive as they can be implemented by simply using a single comparator, as these return a logical value indicating whether the signal amplitude is above or below a certain threshold value. A quantiser with one bit results in $2^1 = 2$ quantisation levels. The quantisation function can be described as

$$Q(z) = \frac{1}{\sqrt{2}}\left(\text{sign}\left(\text{Re}\{z\}\right) + j\,\text{sign}\left(\text{Im}\{z\}\right)\right). \tag{4.10}$$

Hence, by (4.10), each sample is quantised to become one of the four values $\frac{1}{\sqrt{2}}(\pm 1 \pm 1j)$. It is noteworthy that all amplitude information is therefore lost, with only phase and frequency information remaining.

A technique to incorporate one-bit data in DOA estimation methods that use the covariance matrix is proposed in [38]. This technique is based on the idea of reconstructing the unquantised covariance matrix from the one-bit matrix by making use of the arcsine law. In [34] it is shown that using the one-bit covariance matrix without reconstruction does not have a significant negative impact on performance, especially at low SNR levels. If we want to use VEXPA with one-bit data, it would therefore be ideal to use Root-MUSIC as the underlying method, as it uses the covariance matrix.

We first compare the quantised-data performance of Root-MUSIC against the Matrix-Pencil method in a dense array configuration (12 elements, 0.48λ spacing). In addition, we vary the number of signals from one to three, with the respective angles of arrival at 10°, 30°, and 90°. Moreover, the SNR and number of snapshots are kept constant at 30 dB and 256, respectively. The number of ADC bits is varied from 1 to 8, meaning 2 quantisation levels at the least, and 256 at the most. For the above experiment, 100 Monte Carlo runs are performed, and the RMSE results are shown in Fig. 4.10. As suspected, we see that Root-MUSIC performs accurately even with the minimal number of bits and multiple incoming signals. The Matrix-Pencil method, on the other hand, has low error values for a single incoming signal, but when multiple signals are present, a higher resolution ADC is required. This reiterates that if an ADC with few bits is used, Root-MUSIC is the preferred underlying method.

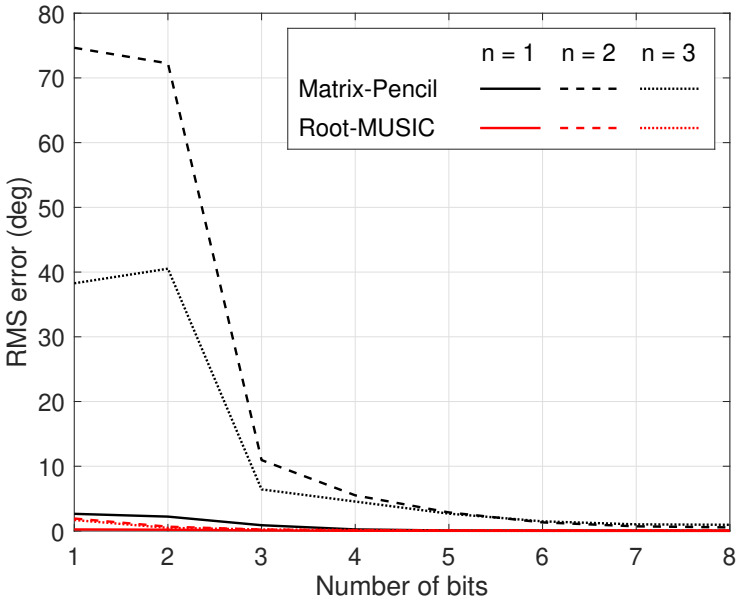

Figure 4.10: Performance of Matrix-Pencil and Root-MUSIC with a dense array configuration, with data quantised by ADCs of different bit sizes. Root-MUSIC performs accurately with low-resolution quantised data, whereas Matrix-Pencil has difficulty estimating the correct directions when more than one signal is present.

Next we investigate how these methods perform with the same experiment, but with a sparse co-prime configuration using VEXPA. The array consists of 12 elements, with $\sigma = 11$ and $\rho = 5$. To determine if it is at all possible to estimate the DOAs successfully with the co-prime setup and low resolution quantised data, we first specify the number of incoming signals for the algorithm, indicating how many clusters should be detected in the cluster analysis step.

The results are shown in Fig. 4.11. We see that, for one incoming signal, the RMSE is comparable to the dense case in Fig. 4.10 for both the Matrix-Pencil method and Root-MUSIC. For multiple incoming signals, however, a high number of bits is required to estimate the DOAs accurately, even for Root-MUSIC. Matrix-Pencil is completely unsuccessful in returning estimated signals when only one or two bits are available. As mentioned before, an ADC with fewer bits results in amplitude errors in the signal data. For the VEXPA algorithm, the signal amplitudes are important when retrieving the base terms Ψ_i^ρ from the Vandermonde system in (3.12), so even if the underlying method can solve the base terms of ULA 1 successfully, an error is introduced in the succeeding step. As the number of incoming signals increase, the effect of this amplitude error worsens, which explains why a significantly higher error is observed for Root-MUSIC with one-bit data and two or three signals.

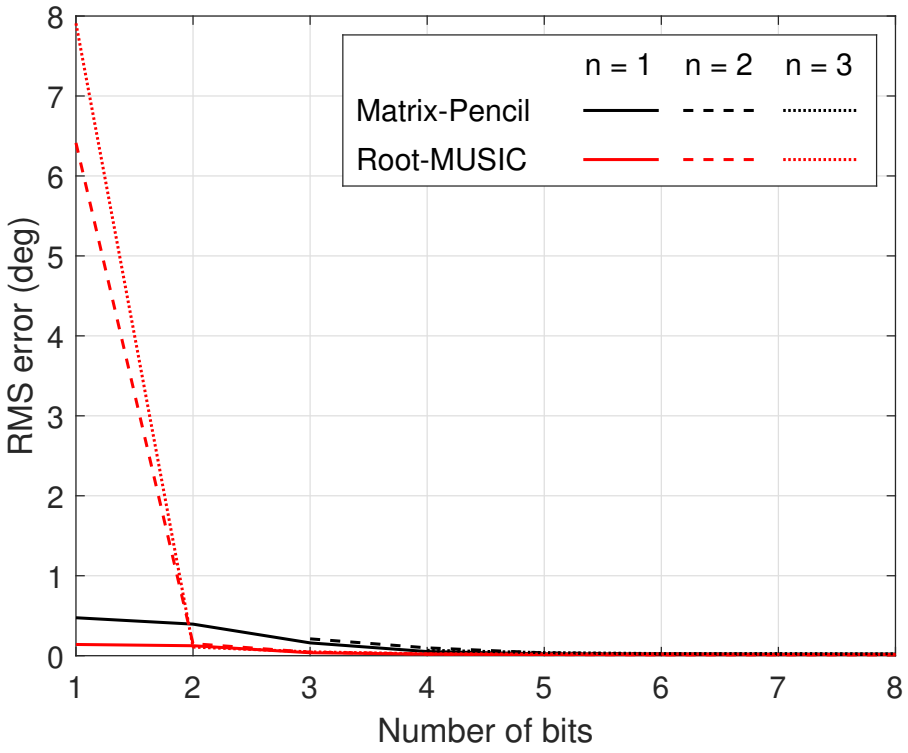

Figure 4.11: Performance of VEXPA (with Matrix-Pencil and Root-MUSIC underlying) with a sparse co-prime array configuration, with data quantised by ADCs of different bit sizes. Root-MUSIC performs accurately with low-resolution quantised data, whereas Matrix-Pencil does not return any DOA when more than one signal is present.

Next, we consider the effect of letting VEXPA estimate the number of incoming signals. Fig. 4.14 shows the success rates of the same experimental setup as Fig. 4.11, with the exception that the number of signals is now overestimated as $M_\sigma/2 = 3$, instead of being specified. Something interesting to note is that, in the case of Root-MUSIC, the success rate is lower for one incoming signal than multiple signals, which is the opposite for the case when the number of signals is specified. This is because lower-resolution input data allows for fewer possible base terms, so the spurious base terms also form clusters, whereas they are scattered for higher-resolution data. This is worse for fewer signals due to the overestimation of a higher degree, resulting in more spurious base terms than true ones. Fig. 4.12 illustrates the different base term results of Root-MUSIC for two-bit (left-hand side) and five-bit data (right-hand side) respectively, with one incoming signal. The black dots are the roots calculated by Root-MUSIC for each subset of snapshots. For each of these 256 subsets, Root-MUSIC calculates $2(M_\sigma - 1) = 10$ roots, after which the $M_\sigma/2 = 3$ roots closest to the unit circle are accepted as the base terms and sent to the clus-

tering algorithm. The final clusters are also shown in the figure as coloured circles. For the two-bit data on the left-hand side, we see the lower-resolution data causes the noisy data to form clusters as well, leading to three clusters being detected. For the five-bit data on the right-hand side, the noisy data is scattered, and the correct number of clusters is detected. Fig. 4.13 shows the same results as the left-hand side of Fig. 4.12, except for two incoming signals instead of one. Here we see that even with low-resolution, two-bit data, the right number of clusters are found, due to the overestimation of a lesser degree.

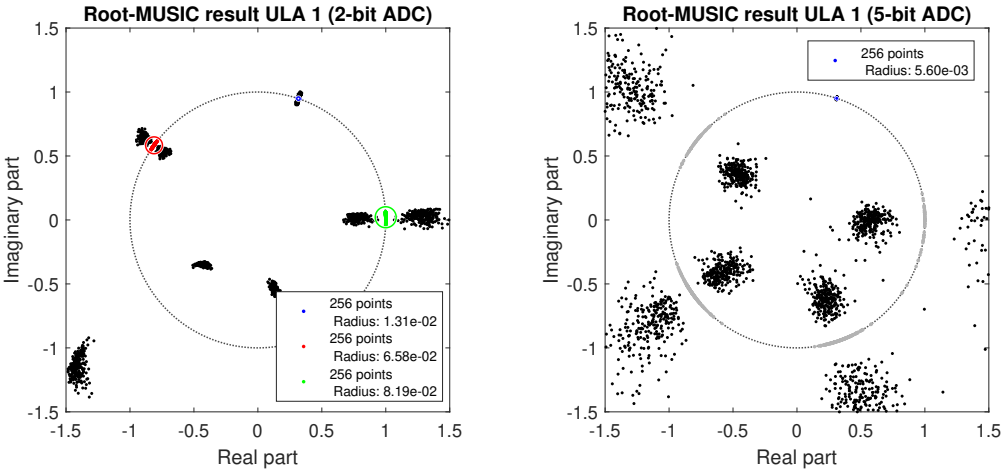

Figure 4.12: The base term results returned by Root-MUSIC for one incoming signal with quantised data. The results are less scattered for two-bit data (left-hand side graph) than for five-bit data (right-hand side graph). This leads to DBSCAN detecting too many clusters for the one-bit data, leading to an incorrect estimation of the number of incoming signals.

From this, we can conclude that Root-MUSIC is the preferred method to use underlying to VEXPA when an ADC with few bits is used, and if the number of incoming signals is unknown, erroneous results are expected.

The work done in the above section will be included in a conference paper that is currently in preparation [35].

4.8 Systematic errors

4.8.1 Antenna position errors

Errors in the antenna element positions translate to phase delay errors in the array steering matrix. It is important to detect these errors so that they can be mitigated in software. We investigate the effect of positional errors by shifting the coordinates of the elements with a distance-vector, chosen randomly from a sphere with uniformly distributed radius, azimuth and elevation angle. The

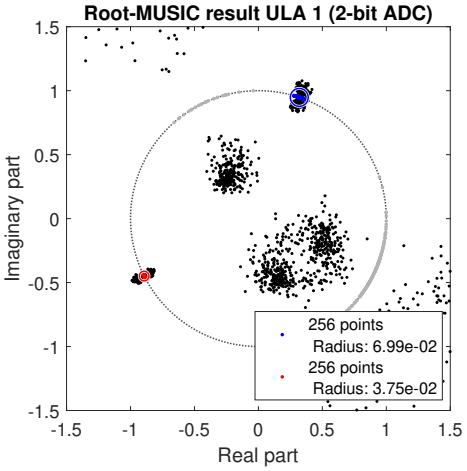

Figure 4.13: The base term results returned by Root-MUSIC for two incoming signals with two-bit quantised data. Unlike the case for one incoming signal, the correct number of clusters are found for data quantised with a two-bit ADC.

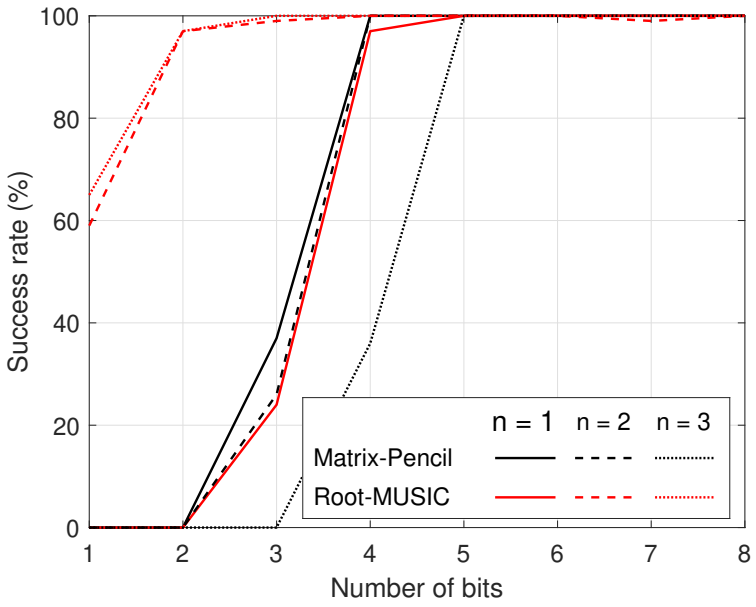

Figure 4.14: Success rate of VEXPA (with Matrix-Pencil and Root-MUSIC underlying) with a sparse co-prime array configuration, with data quantised by ADCs of different bit sizes, when the number of incoming signals is over-estimated. Data quantised by fewer bits cause spurious base terms to form clusters when the true number of signals is low.

maximum possible radius of the sphere, i.e., the upper limit of the uniform distribution, is varied to represent smaller and larger errors and is expressed in terms of wavelengths. As in Section 4.4, two arriving signals are present, the first fixed at $\phi_1 = 45°$, and the second varied in $\phi_2 \in [30°, 44°]$. The spherical radius is varied in $\epsilon \in \{0.01\lambda, 0.05\lambda, 0.06\lambda\}$, while the SNR and number of snapshots are kept constant at 30 dB and $2^8 = 256$, respectively.

Fig. 4.15 shows the results. Once again, both the Matrix-Pencil method and Root-MUSIC are used underlying to VEXPA. The virtual dense array has a spacing of 0.3λ, resulting in an angular resolution or Rayleigh limit of 3.18°, which is indicated by the black dotted lines. These results indicate that a phase calibration accuracy of around 0.06λ is required to achieve an estimation accuracy better than the Rayleigh limit. The above experiment was presented in an abstract paper for the 2019 IEEE-APS Topical Conference on Antennas and Propagation in Wireless Communications (APWC) [39].

Next, we also consider the success rate of VEXPA as the radius of the positional error is varied. The experiment is as before, but we consider two pairs of two incoming signals: the first, at $\phi_1 = 45°$, $\phi_2 = 45° - \Delta_\phi = 41.82°$, and the second at $\phi_1 = 45°$, $\phi_2 = 30°$. In Fig. 4.16, the top and bottom graphs show the results of the first and second pair of signals, respectively. As expected, the case where the angular separation between the signals is equal to the Rayleigh limit results in the success rate starting to drop at a smaller positional error than when the signals are separated further from each other. The Matrix-Pencil method shows this observation more clearly than Root-MUSIC, meaning that the latter is more capable of detecting signals with a smaller angular separation.

4.8.2 Calibration errors

In practice, all antenna elements are not identical and some systematic errors may be present in the channels before any calibration process is executed. For this reason, it is important to investigate the effect that channel amplitude and phase errors have on DOA algorithms. Channel errors are simulated by adding a complex Gaussian signal at the channel of each individual antenna, which is then multiplied with the incoming signal at the respective antenna. The complex noise signal is made up of a normally distributed amplitude within a certain standard deviation (SD) and a uniform random phase shift. The size of the error is increased by increasing the standard deviation of the noise signal. Three different experiments are performed, with one, two and three incoming signals, respectively. For the experiments, the angles of arrival are $\phi = 90°$, $\phi = 90°$, 75° and $\phi = 90°$, 75°, 60°. The SD of the amplitude of the error signals is varied as SD $\in [0; 0.7]$, and 100 Monte Carlo runs are performed at every fixed SD.

Fig. 4.17 shows the results of the above-mentioned experiment. The true angles for the incoming sources are indicated as thick blue dashed lines. The

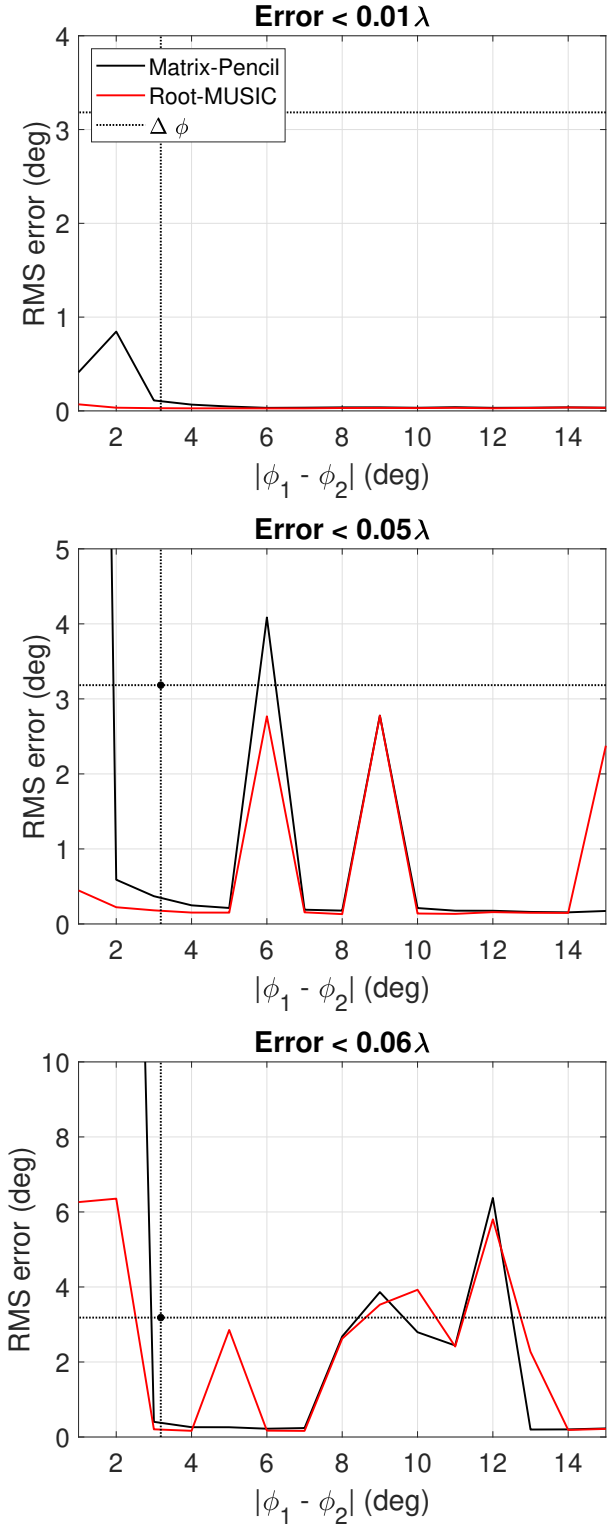

Figure 4.15: RMS accuracy of two incoming directions for a range of angular separations. The top graph shows results for positional errors of $\epsilon < 0.01\lambda$, the middle graph for $\epsilon < 0.05\lambda$ and the lower for $\epsilon < 0.06\lambda$. Note the different scales for the vertical axes.

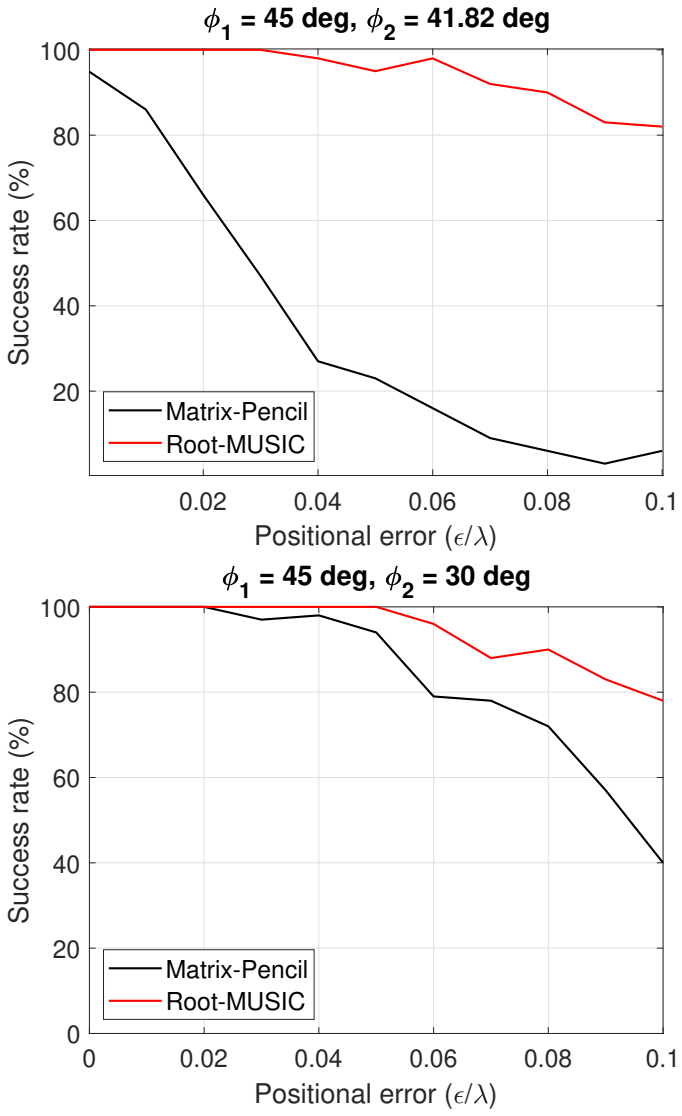

Figure 4.16: Success rates of VEXPA when the radius of the positional error is varied and the two angles of arrival are constant. The top graph shows results for the signals at $\phi_1 = 45°$, $\phi_2 = 45° - \Delta_\phi = 41.82°$, and the bottom graph for the signals at $\phi_1 = 45°$, $\phi_2 = 30°$. The smaller angular separation shows a drop in success rate for smaller positional errors.

angular resolution (or Rayleigh limit) is indicated as thinner dashed blue lines above and below the true angles. For both the Matrix-Pencil method and Root-MUSIC, errors become significant as the SD of the amplitude error increases, which is to be expected. For the most part, however, the estimated angles remain well within the Rayleigh limit, up to at least SD = 0.35. This means that the antenna channels should be calibrated for errors larger than this standard distribution.

The practical difference between the above experiment and the positional error experiment in the previous subsection is clear. However, the statistical comparison is not something we can deduce by just looking at the results. To compare these experiments statistically, we consider the output signal when the respective errors are applied to an input signal. This input signal is specifically the received signal at an antenna element when two noise-less complex exponential signals with zero phase are arriving from $\phi_1 = 45°$ and $\phi_2 = 30°$. The SD of the calibration error is equal to 0.35 and the maximum radius of the positional error is 0.06λ. To isolate these errors, no other non-idealities are introduced. We only consider one snapshot and one antenna element as these errors are time-independent and statistically equal for all elements. A total of 1×10^4 Monte Carlo runs are performed, and the PDF of both the output amplitude and phase are estimated by performing a kernel density estimation (KDE). Kernel estimation is a technique to estimate the PDF of a random variable, providing a smoother estimate than the traditional histogram [40]. The results are shown in Fig. 4.18, with the amplitude and phase PDF in the top and bottom graph, respectively. The phase results look similar for the two experiments, with the PDF spread around zero phase. The difference appears in the amplitude PDF: the PDF of the positional error has a very narrow spread, whereas that of the calibration error output is spread more widely. This is because the shifting of the antenna elements translates to a phase error, with no change to the signal amplitude. We can therefore conclude that the effect on VEXPA of the two types of errors are statistically very similar, as a phase error is much more significant than an amplitude error in the DOA estimation problem.

4.8.3 Mutual coupling

Mutual coupling between antenna array elements means that a voltage is induced at other elements due to an excitation at one antenna [5]. The mutual coupling worsens if the inter-element spacing is smaller, and thus a sparse array has the advantage of less mutual coupling. The computational electromagnetics software FEKO [41] is used to perform full-wave method of moments (MOM) simulations. A dipole antenna array is considered, with elements having lengths of $\lambda/2$ and radii of $\lambda/1000$ (thin wires). The dipoles are oriented along the z-axis, and the array axis is along the x-axis.

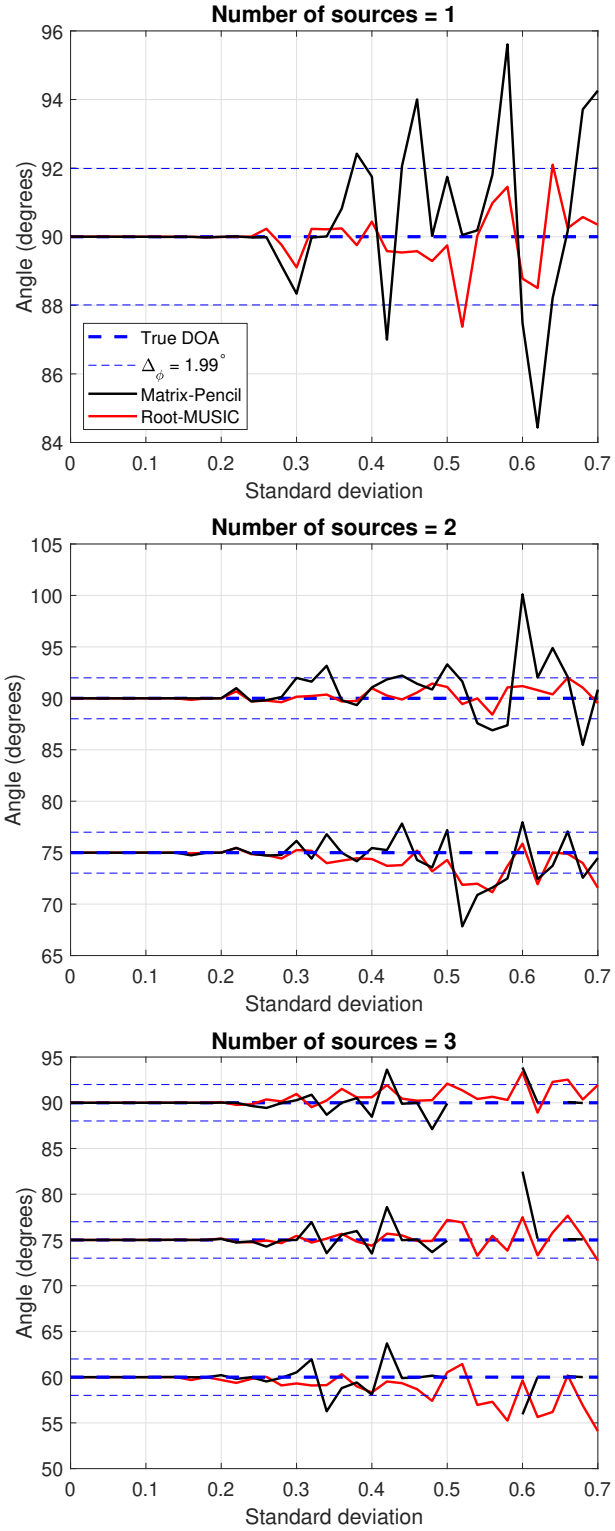

Figure 4.17: DOA angles retrieved from VEXPA with ESPRIT and Root-MUSIC underlying when increasing the standard deviation of a Gaussian amplitude channel error. The phase channel error is uniform random. In the top panel the number of sources = 1 at 90°, the middle panel two sources at 90°, 75° and the bottom panel three sources at 90°, 75°, 60°. These are indicated as thick blue lines. The angular resolution is 1.99°, indicated on either side of each true DOA.

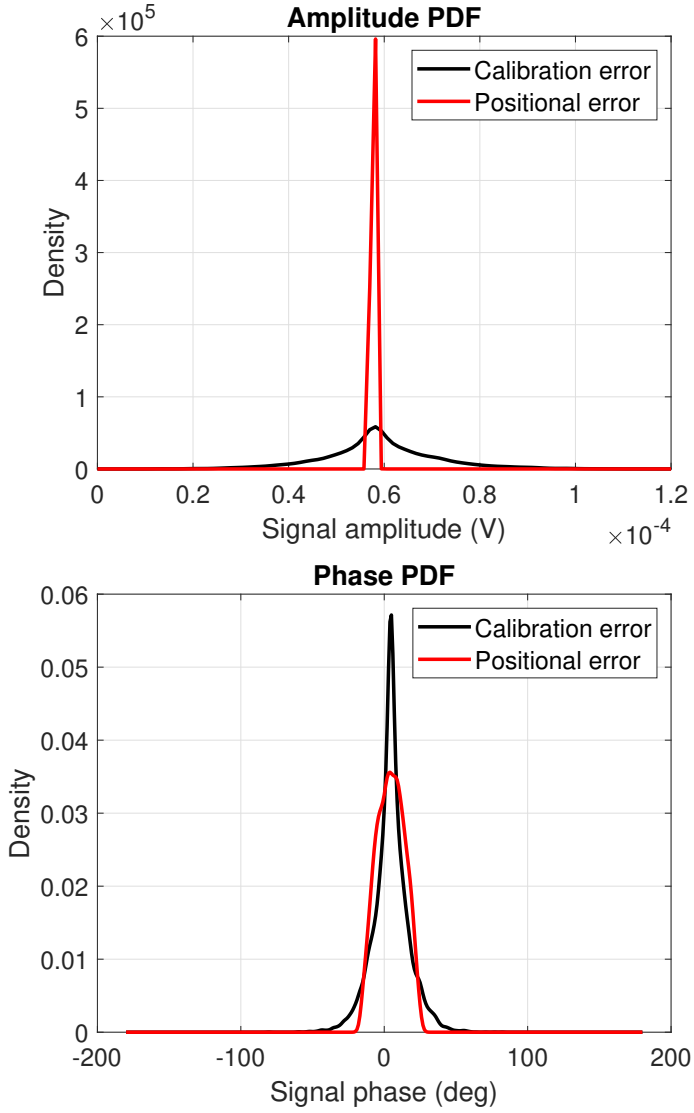

Figure 4.18: Kernel density estimation of the probability density functions of the output signal when a calibration and positional error are applied, respectively. The PDF of the amplitude and phase are shown in the top and bottom graph, respectively. The biggest difference between the experiments is that the positional errors do not introduce an amplitude error, as can be seen by the steep peak in the PDF of the red plot in the top graph.

The array is excited by two monochromatic plane waves with slightly different frequencies to achieve signal incoherence. The incoming directions of the signals are $\phi_1 = 90°$ and $\phi_2 \in [75°, 90°]$. In addition, the scaling parameter $\sigma = 11$, shifting parameter $\rho = 5$, with $M_\sigma = M_\rho = 6$, and the virtual dense array inter-element spacing d is varied in $d \in [0.9\lambda, 0.3\lambda, 0.48\lambda]$. Thereafter, the RMSE is calculated for each DOA individually, with the results shown in Fig. 4.19, with the top (bottom) graph referring to the most dense (sparse) configuration. The resolution $\Delta\phi$ for each configuration is indicated as a vertical dotted line in each graph.

It is clear that for each array setup, both signals can be resolved accurately from about half the Rayleigh limit for the Matrix-Pencil method, and about a quarter of the Rayleigh limit for Root-MUSIC. Increasing d has the effect of lower mutual coupling and therefore lower errors in estimated angles. For example, the resolution for the most sparse case at $d = 0.48\lambda$ is approximately a factor 5 better than for a half-wavelength dense array. This resolution can be increased even further by increasing σ and ρ [7].

4.9 Narrowband assumption

As mentioned in Section 2.2, the narrowband assumption allows us to make the approximation $s_i(t + m\tau_i) \approx s_i(t)$ in (2.14). This is achieved if the amplitudes and phases of the incoming signals are slowly varying with time, i.e.,

$$a_i(t) \approx a_i(t + \tau) \quad \text{and} \quad p_i(t) \approx p_i(t + \tau). \tag{4.11}$$

Together with the requirement that the frequency contents of the incoming signal are in close proximity of the carrier frequency, this ensures that the Fourier transform of the signal has a single frequency component [8]. Essentially, no signal decorrelation occurs between the opposite ends of the antenna array. The effect of dispersion causes a zero-bandwidth signal to be perceived as coming from a single discrete angle, whereas a non-zero-bandwidth signal appears to be coming from multiple angles [42]. This is illustrated in Fig. 4.20.

It was shown in Section 2.3.2 that the rank of the input data covariance matrix is equal to the number of incoming signals. However, when the frequency contents of the signal are spread outside the centre frequency, the rank of the signal covariance matrix is increased from one to two. Compton quantified the requirement for a signal to qualify as narrowband as [43]

$$\text{sinc}\,(2b\tau_{1N}) \approx 1, \tag{4.12}$$

where b is defined as $f_{max} - f_0$, and τ_{1N} is the signal time delay between the first and Nth element in the array.

To illustrate the effect of wideband signals, we consider a narrowband noise signal as defined in Section 4.2 incoming from $\phi = 60°$, and vary the fractional

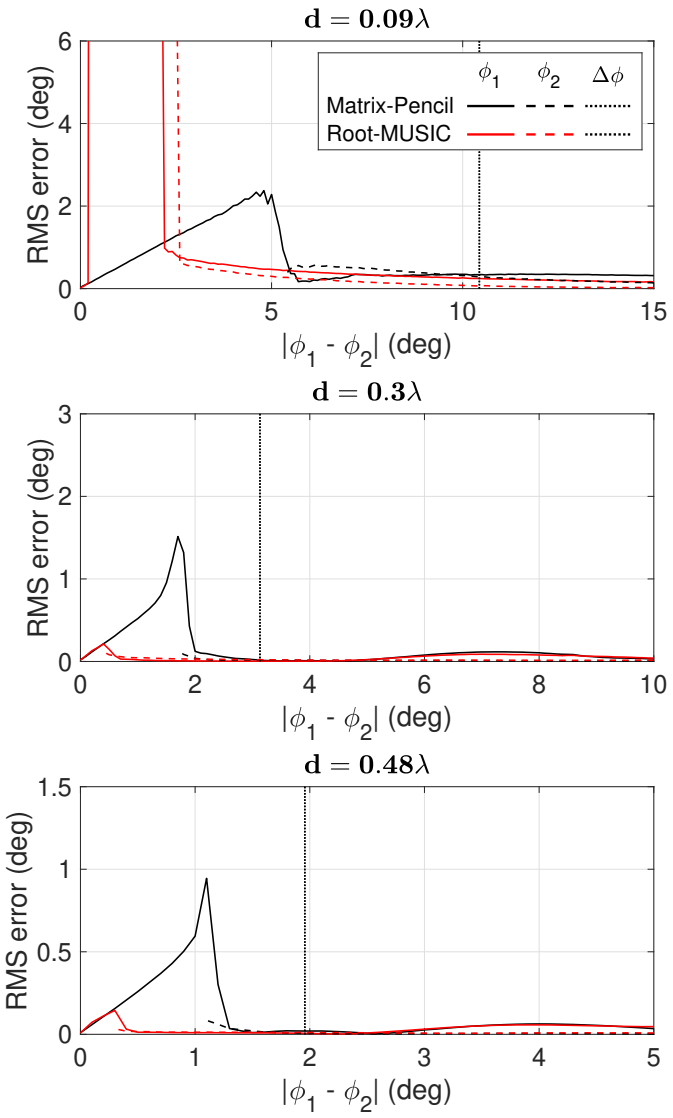

Figure 4.19: Performance of the VEXPA algorithm for three different array configurations on data from a FEKO full-wave MOM simulation. The top graph shows the results of an array with $d = 0.09\lambda$, the middle graph $d = 0.3\lambda$, and the bottom graph $d = 0.48\lambda$. Note the different axes for each graph. With a sparser configuration, less mutual coupling is achieved, resulting in greater accuracy.

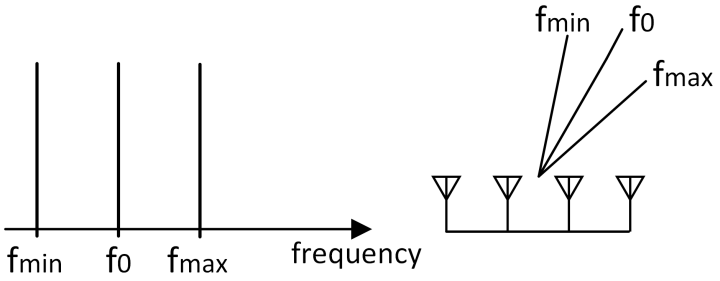

Figure 4.20: An illustration of the effect of dispersion, which occurs when the frequency contents of a signal contain more than a single frequency component.

bandwidth b_f. As we increase the bandwidth of the signal, the DOA estimation methods no longer only detect one signal, but rather two coming from inaccurate directions. As this occurrence has a significant relation to the estimation of the number of incoming signals, the two different estimation methods are considered: the traditional method of considering the sizes of the eigenvalues, and the cluster analysis method as introduced by VEXPA.

The results are displayed in Fig. 4.21. We see that for both methods, Root-MUSIC starts detecting two signals at a lower bandwidth than the Matrix-Pencil method. This can be expected, as Root-MUSIC is able to detect incoming signals with very small angular separations. Moreover, we observe that the scenario allowing for the biggest bandwidth is when the Matrix-Pencil method is used in conjunction with the cluster analysis method. This is again due to the fact that determining the number of signals per snapshot, as for the eigenvalue method, gives the impression that two signals are present. However, when the results of all the snapshots are passed to a clustering method, these results form one cluster in the vicinity of the true base term. This reiterates the premise that DOA estimation methods operating per snapshot can benefit from the cluster analysis method. Furthermore, we conclude that the Matrix-Pencil method is the preferred method when dealing with wider rather than strict narrowband signals.

4.10 Practical consideration of collided base terms

In Section 3.6, we addressed the problem of collided base terms, which occurs when the angles of multiple incoming signals result in equal or nearly-equal base terms. The estimation algorithms cannot distinguish between these, and return a single result for each set of collided base terms. This is similar to the problem caused by angles closer than the angular resolution, for the dense case.

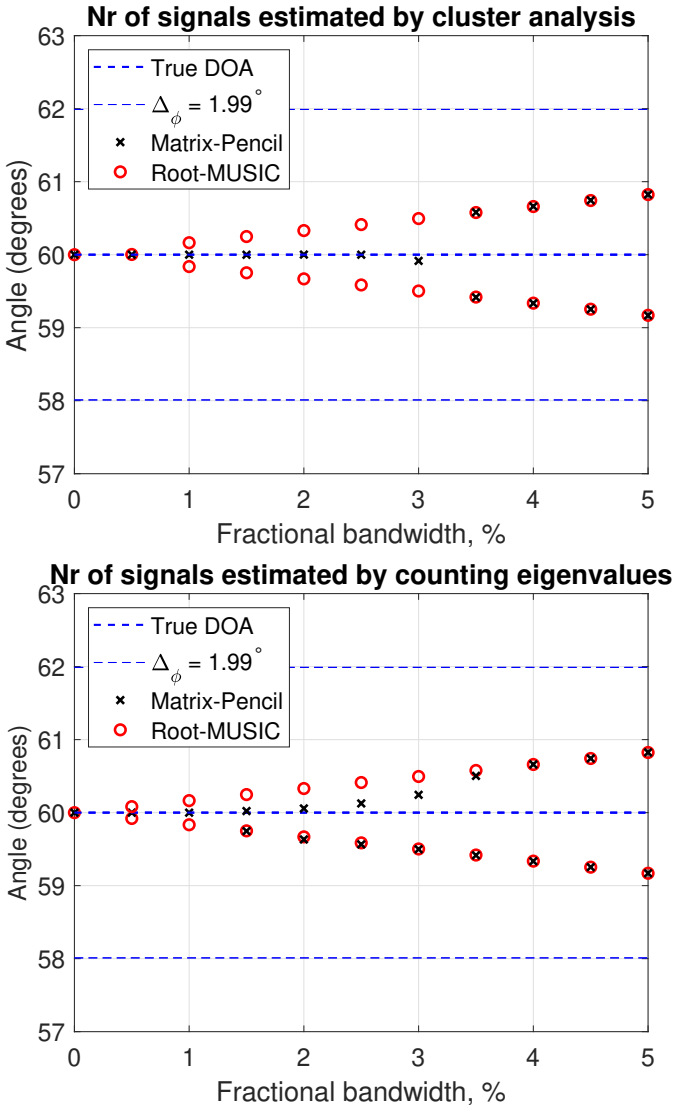

Figure 4.21: DOA angles retrieved from VEXPA with the Matrix-Pencil method and Root-MUSIC underlying when increasing the fractional bandwidth of a single narrowband noise signal arriving from 60°. The top graph shows the results when the cluster analysis method is used to estimate the number of incoming signals, and the bottom uses the eigenvalue method. As the fractional bandwidth increases, two signals are detected instead of one, explaining the relevance of the narrowband assumption when working with DOA estimation.

As mentioned previously, the base terms Ψ_i^σ, computed using the samples of ULA 1, are complex values situated on the unit circle, i.e., a unity amplitude and a phase given by

$$|\arg(\Psi_i^\sigma)| = \frac{\omega \cos\phi_i \sigma d}{c}. \tag{4.13}$$

If we consider the virtual dense array to have half-wavelength spacing, this simplifies to $|\arg(\Psi_i^\sigma)| = \sigma\pi\cos\phi_i$. We therefore expect the algorithm to fail when the difference between the phases $\sigma\pi\cos\phi_i$ is too small. To demonstrate these failures, we consider the positions of the base terms Ψ_i^σ for all the DOAs in $[0°, 90°]$. In this setup two array configurations are used: each with the standard setup as mentioned in Section 4.1, but with one difference. The virtual dense array inter-element spacing is 0.04λ and 0.48λ, respectively, in effect meaning that the one array is dense. This is shown in Fig. 4.22, with the dense array base terms on the left-hand side. The colour of the markers gets darker as the DOA increases, with the lightest colour used for $\phi = 0°$ and the darkest for $\phi = 90°$. As the base terms of dense arrays all fit in one revolution of the unit circle, the base terms that are situated close to one another correspond to DOAs from similar angles. For the sparse case, however, there is no relationship between the angles that correspond to closely-situated base terms.

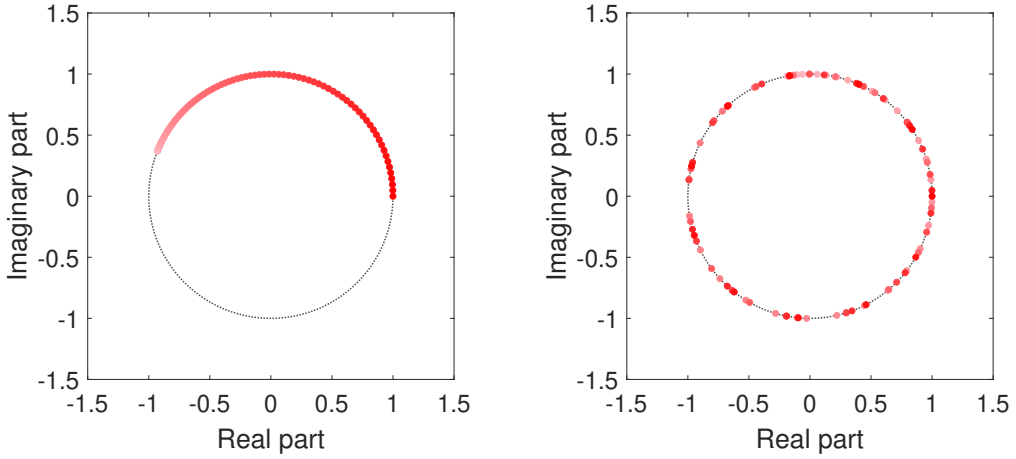

Figure 4.22: The base terms Ψ_i^σ for $\phi \in [0°, 90°]$, with the darker markers representing bigger values of ϕ. The left and right graphs correspond to a dense and sparse array, respectively. Signals that have closely-situated base terms will be more difficult to distinguish.

Next, we investigate how sensitive VEXPA is to this issue by considering two incoming signals, the first fixed at $\phi_1 = 90°$, and the second varied in $\phi_2 \in [0°, 90°]$, and plotting the success rate against the phase difference between the two base terms of the two incoming signals. Fig. 4.23 shows

the results, with the phase differences wrapped in radians to $[-\pi, \pi]$, and also expressed as a fraction of 2π, to represent the sector of the unit circle separating the two base terms. We observe that the Matrix-Pencil method requires a separation of more than 0.12 of a revolution to achieve a 100% success rate. This translates to roughly a 43° difference. Root-MUSIC delivers accurate results with smaller separations, at about 0.04 of a revolution, or 14°. It is reiterated that these values refer to the phase differences of the base terms, i.e., $|\arg(\Psi_2^\sigma)| - |\arg(\Psi_1^\sigma)|$, and not the actual angles of arrival.

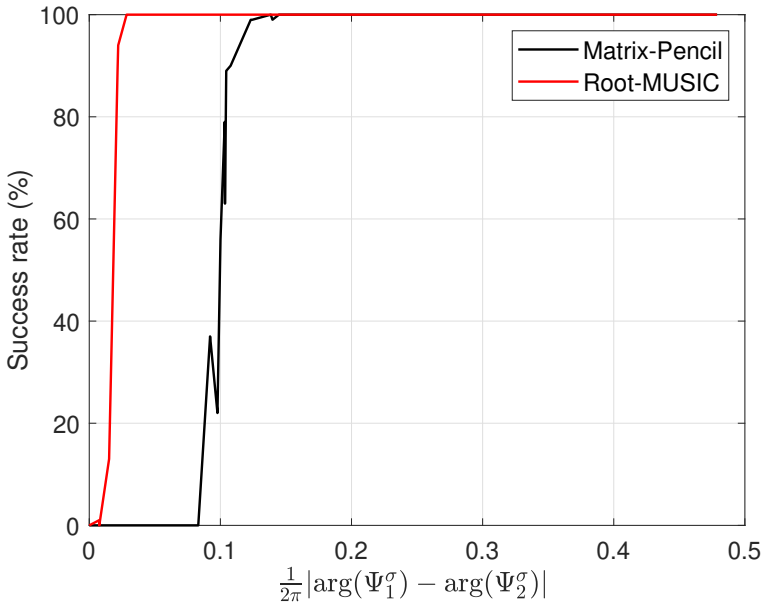

Figure 4.23: Success rate of VEXPA (with the Matrix-Pencil method and Root-MUSIC underlying) with two signals that have base terms separated by a certain phase on the unit circle. The x-axis labels are expressed as fractions of 2π. The Matrix-Pencil method requires the base terms to have a separation of about 43° for a 100% success rate, while Root-MUSIC can distinguish between base terms that are closer, at a separation of about 14°.

It is important to mitigate this occurrence, as there are often signals coming from different directions with similar base terms. The mathematical solution to this problem is discussed previously in Section 3.6, but as this method requires additional samples and thus additional antenna elements, it is not ideal.

Frequency division multiple access (FDMA) or frequency division multiplexing (FDM) refers to the practice of transmitting multiple signals on the same channel without the signals interfering with one another [44]. This is done by modulating each signal to a different carrier frequency. The total

bandwidth of the communication channel is split up into different subchannels, each with its own bandwidth. These subchannels should not overlap, and guard bands occur between adjacent subchannels to isolate them.

A shift in frequency implies that the base term shifts as well, meaning that the collisions will occur at different DOAs. The above entails that a bigger bandwidth, such as in the practice of FDM, could be useful for detecting collided base terms, when the different frequency subchannels are used. Remembering that DOA estimation methods are used to detect interference signals, it is useful to know that broadband RFI signals exist in practice.

In order to detect where the collisions occur for the standard experimental setup, we set $\phi_1 = 90°$ and vary ϕ_2 in $[0°, 90°]$, and consider the success rates of VEXPA with both the Matrix-Pencil method and Root-MUSIC. The frequency of the two signals is at 0.948 GHz, for which the reason will become clear later. The results are shown in Fig. 4.24, where we can see which angles cause collided base terms by the abrupt dips in success rate. Next, we discuss

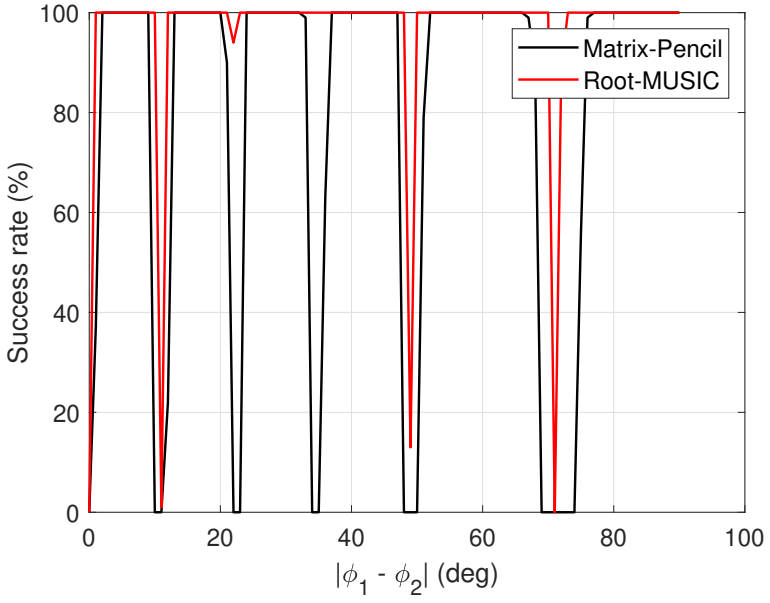

Figure 4.24: Success rate of VEXPA with $\phi_1 = 90°$ and $\phi_2 = [0°, 90°]$. The low success rates occur at angles where the base terms of the two signals are too close to each other to be distinguished.

how the success rates can be improved by the mitigation method described in Section 3.6. We choose $R = 4$, meaning one scaled ULA and three shifted ULAs. Each shifted ULA consists of two elements, while the scaled ULA consists of six. This means twelve elements in total, in order to retain the number of elements from the original experiment. The results are shown in Fig. 4.25, where we can see a significant improvement in success rates. There

are only two collisions causing completely unsuccessful runs for the Matrix-Pencil method, at $\phi_2 = 67°$ and $\phi_2 = 68°$. The success rate for Root-MUSIC does not fall below 85%, except for $\phi_2 = 90°$, as only one signal is detected.

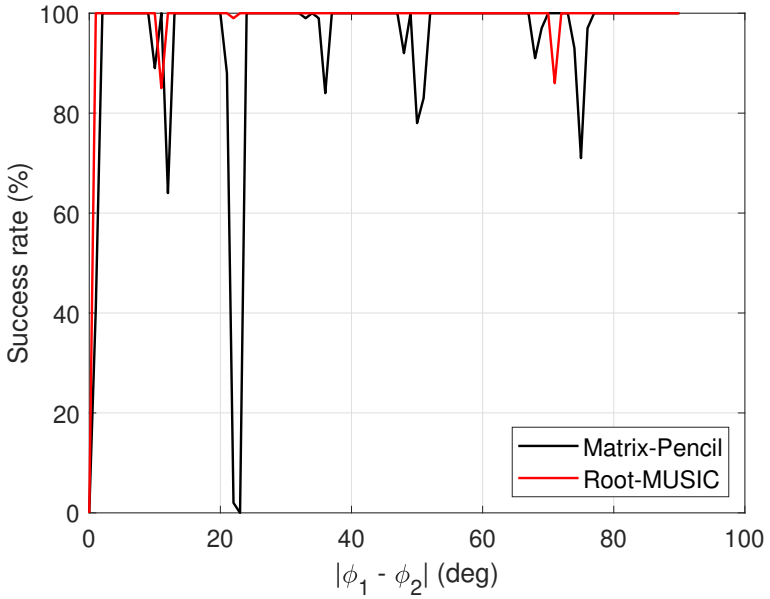

Figure 4.25: Success rate of VEXPA with $\phi_1 = 90°$ and $\phi_2 = [0°, 90°]$, when using the approach to mitigate collisions. A significant improvement can be seen from Fig. 4.24.

Next, we illustrate how a larger bandwidth can improve the problem of collided base terms. We consider a fractional bandwidth of 10%, with the centre frequency at 920.5 MHz, with 124 frequency channels. The choice of frequency channels results in the experiment repeating 124 times, each time with the signals at a different frequency. The virtual dense array inter-element spacing is at half of the minimum wavelength, to ensure the spacing is dense for all the wavelengths in the band. In addition, the minimum wavelength corresponds to the maximum frequency in the band, at 0.948 GHz, which is why the previous two experiments were also conducted at this frequency. Fig. 4.26 shows the returned DOAs by VEXPA at the 124 different frequencies, specifically for $\phi_1 = 90°$ and $\phi_2 = 53°$. Here we can clearly see how the algorithm is only successful at the higher and lower frequencies in contrast to the middle frequencies, where collisions occur. In the case where we have access to results at a larger bandwidth, we can then perform a cluster analysis and obtain accurate results by filtering out faulty DOAs caused by collisions. The success rate when a cluster analysis algorithm is performed on the complete set of results from all 124 frequencies is shown in Fig. 4.27. We see that all collisions are mitigated, except for the case when $\phi_2 = 79°$ for the Matrix-

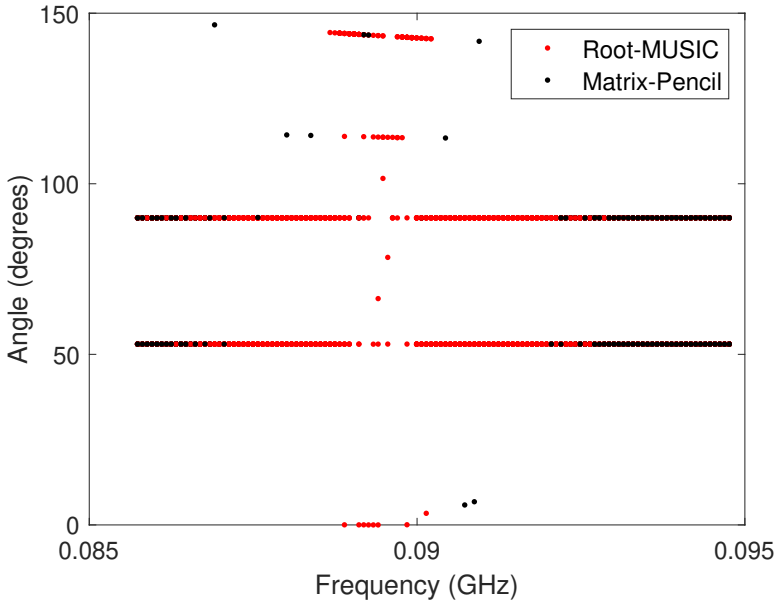

Figure 4.26: DOAs returned by VEXPA with $\phi_1 = 90°$ and $\phi_2 = 53°$, for signals at different frequencies. Inaccurate results occur at frequencies where the base terms for the two incoming signals are too closely spaced and result in a single, inaccurate returned DOA.

Pencil method. In theory, the use of wideband signals is thus a useful method to combat the problem of collided base terms. It should be noted, however, that signals with a fractional bandwidth as wide as 10% are rare in practice; for example, GSM-900 uses 890 - 915 MHz, which translates to a fractional bandwidth of 2.78%. Other limitations introduced when broadband signals need to be detected, are the receivers that need to be capable of handling such bandwidths, as well as consisting of enough channels to represent the wideband signal as several narrowband signals.

4.11 Conclusion

In this chapter we considered how some practical effects affect the performance of VEXPA by performing simulations in Matlab. First, we looked at a way to construct incoherent signals by making use of narrowband noise in order to implement VEXPA using Root-MUSIC as underlying method. We saw that Root-MUSIC could successfully act as underlying method, as long as enough snapshots are available and signal incoherence is achieved. Furthermore, we illustrated the improvement in angular resolution gained by using sparse arrays. In the next section, we compared two methods of estimating the number of signals: the cluster analysis method used by VEXPA, and the traditional method used by dense techniques. We concluded that the usefulness of the

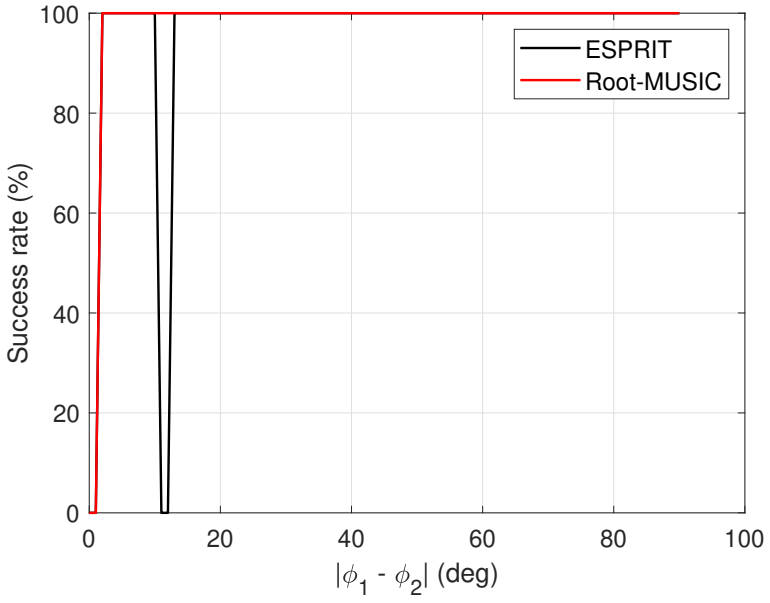

Figure 4.27: Success rate of VEXPA with $\phi_1 = 90°$ and $\phi_2 = [0°, 90°]$, when solving the DOA problem at a band of frequencies, followed by a cluster algorithm. A significant improvement can be seen from Fig. 4.24, with unsuccessful results only at $\phi_2 = 79°$ for the Matrix-Pencil method. This shows that a signal with a larger bandwidth is useful to remove collided base terms.

cluster analysis method depends on the chosen underlying estimation method. We took a brief look at the effect that the SNR and the number of snapshots have on VEXPA. Investigating the quantisation errors introduced by the use of an ADC, we saw that VEXPA struggles to perform accurately with one-bit data when multiple signals are present. After this, we considered some common systematic errors, i.e., position errors, calibration errors and mutual coupling. Next, we saw that the violation of the narrowband assumption leads to the algorithm wrongly detecting two signals when only one is present. Finally, we looked into the possibility of solving the issue of collided base terms by making use of FDMA.

Now that we have an understanding of VEXPA's performance in simulation, the next step is to create a simple practical system. This follows in the next chapter.

Chapter 5

Practical performance of VEXPA

5.1 Experimental setup

Now that we have investigated the performance of VEXPA using simulated data with non-idealities, the next step is to create a practical system to test its performance using practical data. As a receiver, we will be using the Tektronix 6 Series MSO64 oscilloscope which has four channels. This means a total of four antenna elements can be used, two for each sub-ULA. Therefore a maximum of one signal can be detected, as $M_\sigma = 2 \geq 2n$.

The maximum frequency of the incoming signal is limited by the bandwidth of the oscilloscope, which is 2.5 GHz. The far-field assumption mentioned in Section 2.2 states that the antenna array needs to be farther than $2D^2/\lambda$ from the source to ensure a plane wave signal is perceived. Ideally we would want the array as far removed from the source as possible, but we also would like a clear signal without any interference from other sources. For the latter reason, we choose to perform the practical experiment in an anechoic chamber, as to avoid reflections and external noise. The available anechoic chamber allows for a distance of up to 5 m between the source and receiver. Substituting this value and the wavelength at 2.5 GHz into the far-field region criterion, the maximum length of the array is limited to roughly 0.52 m or 4.33λ.

Two different co-prime configurations are used, which we will elaborate on in a later section. The DOA is varied by rotating the antenna array and keeping the source fixed. The measurements are taken at five-degree intervals in the range $\phi \in [45°, 135°]$. The specifications of the experimental setup are shown in Table 5.1.

Table 5.1: Specifications of the practical experimental setup: signal frequency, virtual array spacing, scale and shift parameters for two different setups, number of elements in ULA 1 and ULA 2, and number of snapshots.

f	d	σ_1	σ_2	ρ_1	ρ_2	M_σ	M_ρ	N_t
2.5 GHz	0.4λ	5	7	2	3	2	2	200

5.2 Single antenna element design

For simplicity, a low-cost printed dipole antenna is chosen, with the design based on [45]. A model of the antenna is constructed in CST Studio Suite, which is depicted in Fig. 5.1. A microstrip line is used to feed the dipole arms, and an integrated balun is included to remove any current flowing on the outer conductor of the coaxial cable that will be connected to the antenna.

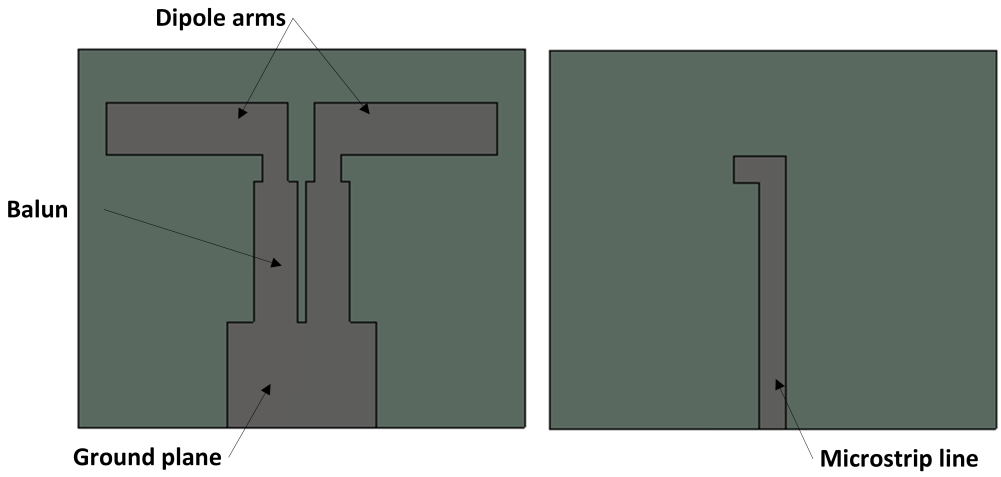

Figure 5.1: The CST design of the dipole antenna element that will be used in the antenna array. A microstrip line is used to feed the dipole arms, and an integrated balun is included to remove any current flowing on the outer conductor of the coaxial cable that will be connected to the antenna.

The antenna elements are printed on FR-4 dielectric substrate with thickness 1.6 mm and permittivity $\epsilon_r = 4.4$. A photo of a single element is shown in Fig. 5.3. The reflection coefficient, or $S11$ parameter, of the dipole is measured

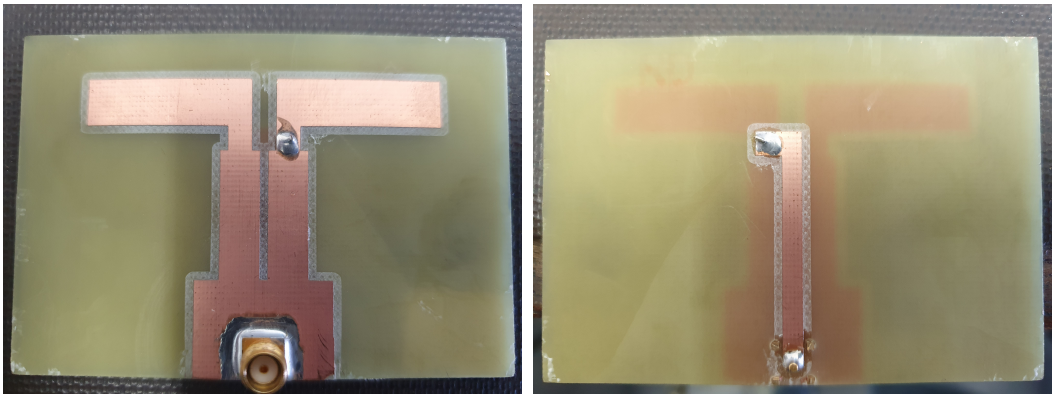

Figure 5.2: A photo of the printed dipole antenna.

by using a vector network analyser; a comparison between these results and those determined by CST is shown in Fig. 5.3. The measured results have a slightly higher resonance than the simulated results, at 2.55 GHz vs 2.48 GHz. Otherwise, the results are in reasonable agreement. At the planned operating frequency of 2.5 GHz, the value of the measured reflection coefficient is -20.19 dB, which is sufficiently low for our use.

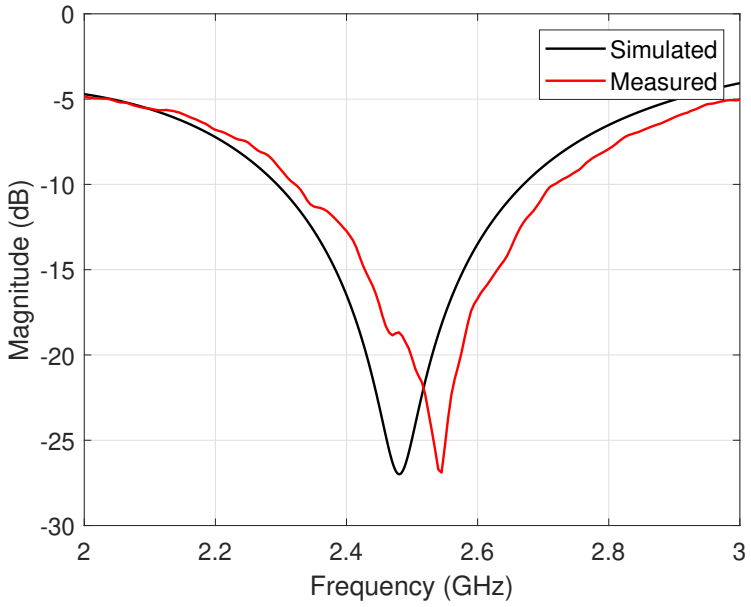

Figure 5.3: The reflection coefficient of the single antenna element. The simulated and measured results are in good agreement.

5.3 Antenna array design

After the single antenna element is designed, the next step is to design an antenna array that can satisfy the requirements of the VEXPA co-prime setup. A ground plane with dimensions 700 mm $\times$ 800 mm is manufactured with a single slit of 500 mm in the middle, allowing the antenna elements to be shifted along a line to create different co-prime configurations. Furthermore, right-angled SMA connectors with nuts are used to allow the shifting, fastening and loosening of the elements. This can be seen on the right-hand side image of Fig. 5.7.

If the position of the first element is taken to be at $x = 0$, the other element positions will therefore be at $x_2 = \rho d$, $x_3 = \sigma d$, $x_4 = (\sigma + \rho)d$, respectively, where d is the virtual dense array inter-element spacing. We choose d as 0.4λ, and since the complete array has to fit in the slit spacing of 0.5m, the requirement $(\sigma + \rho)d < 0.5$ m, or $\sigma + \rho \leq 10$ is created. Two different setups

are chosen: $\sigma = 5, \rho = 2$, and $\sigma = 7, \rho = 3$. These setups are illustrated in Fig. 5.4. The CST model for the first setup is shown in Fig. 5.5. Once

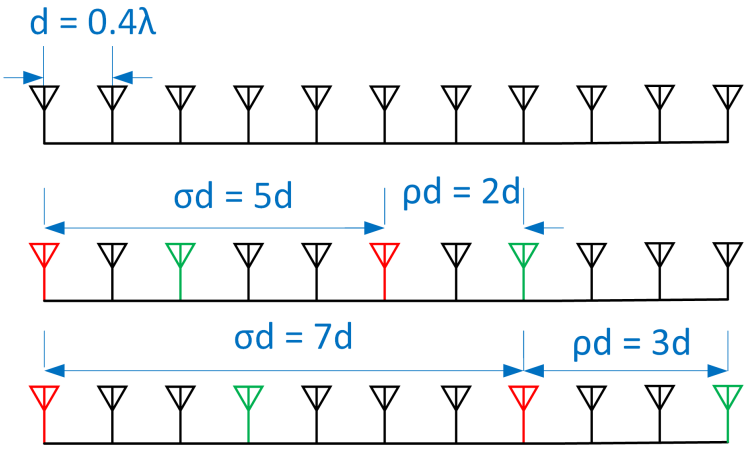

Figure 5.4: The two different co-prime antenna array setups that are used for practical experiments. The top array is the virtual dense array, and the bottom two arrays are the two different setups, with the red (green) elements belonging to ULA 1 (ULA 2).

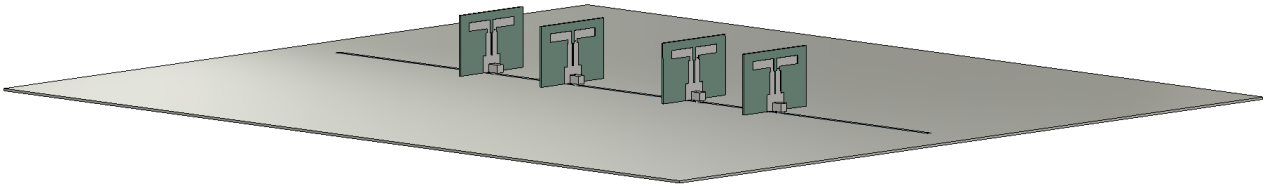

Figure 5.5: A CST model of the antenna array setup with $\sigma = 5$ and $\rho = 2$.

again, the vector network analyser is used to measure the reflection coefficient of all the elements in the complete array structure. As the reflection of all four elements are very similar, we only show the results of one element. The simulated and measured results of the first element are shown in Fig. 5.6, with substantial similarity. If we compare these results to those of the single element in Fig. 5.3, we see the value of reflection coefficient is slightly higher in the array structure, at -15.88 dB at 2.5 GHz. This is, however, still low enough

for our application. A photo of both the mounted antenna array and mounted

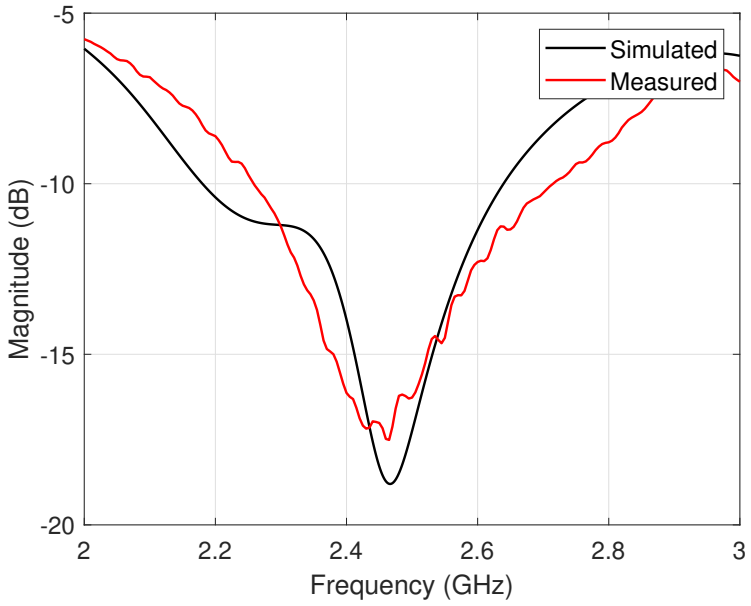

Figure 5.6: The reflection coefficient of the left-most element, i.e., the first element of ULA 1, in the array structure with ground plane. The simulated and measured results are in good agreement.

transmitting antenna in the anechoic chamber can be seen in Fig. 5.7.

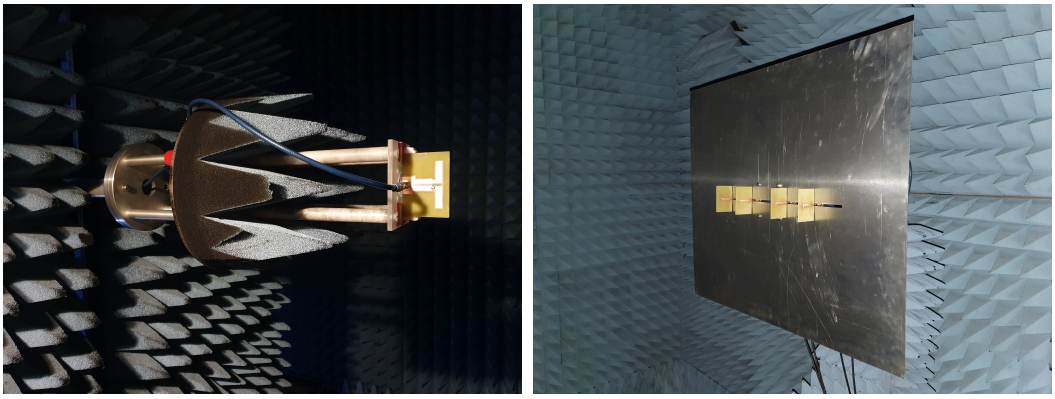

Figure 5.7: Photos of the mounted transmitting antenna (left) and mounted antenna array (right) in the anechoic chamber.

5.4 Data acquisition

Each of the four antenna elements of the array is connected to a channel of the Tektronix 6 Series MSO64 oscilloscope. The oscilloscope has a 12-bit ADC and a sample rate of 50 GS/s (Gigasamples per second) [46]. A photo of the complete setup can be seen in Fig. 5.8.

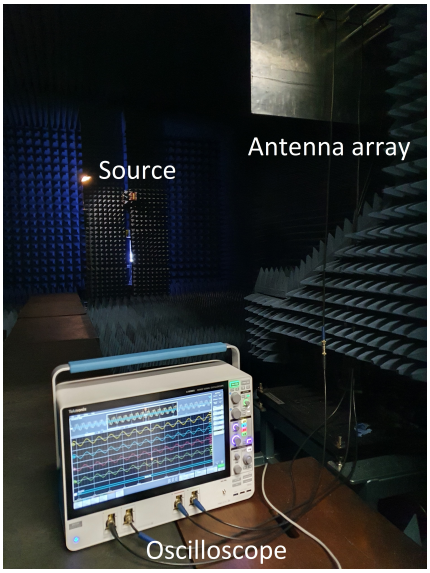

Figure 5.8: A photo of the complete setup in the anechoic chamber.

The data captured by the oscilloscope is the real part of the incoming complex exponential signal, i.e., $\mathrm{Re}(\alpha \exp(j\omega t)) = \alpha \cos(\omega t)$. The imaginary part $\mathrm{Im}(\alpha \exp(j\omega t)) = \alpha \sin(\omega t)$ is equal to the real part with a 90° phase shift. Therefore, if we sample the data at four times the signal frequency (4×2.5 GHz = 10 GS/s), the imaginary part can be retrieved by shifting the data by one sample. As the oscilloscope sample rate is five times larger than our required sample rate, we select every fifth sample, which implies we only use 200 of the total 1000 samples.

In Section 4.8 we mentioned that antenna array systems require calibration to mitigate the errors caused by differences in cable lengths. This is required for our small practical setup as well, as the four cables connecting the antenna elements to the oscilloscope ports are not exactly the same length. When the array is rotated to vary the angle of arrival, the cables will bend, which could cause different angles of arrival leading to different time delays between the received signals at each element. These differences will be small, as the physical cable lengths do not change as the array is rotated. We therefore assume the effect of the cables bending is small enough to implement the same calibration procedure for each angle of arrival, as angle-dependent calibration methods are much more complex.

In order to calibrate the system, we consider the data when the signal is arriving from broadside ($\phi = 90°$). We know for this case the signals received by the four elements should all be in phase. We can therefore create a correction matrix F_{corr}. If F is the matrix of size $N_t \times M$ (remember that N_t is the number of snapshots and M is the number of antenna elements) containing the sampled data, F_{corr} can be constructed by the division $F_{\text{corr}ij} = F_{ij}/F_{i1}$. Then, for DOAs other than broadside, the calibrated data F_{cal} can be obtained by the division $F_{\text{cal}ij} = F_{ij}/F_{\text{corr}ij}$.

5.5 Results

As mentioned previously, the measurements are taken at five-degree intervals in the range $\phi \in [45°, 135°]$. The experiments are repeated at three different output power levels of the signal generator: 0 dBm, 10 dBm, and 25 dBm. The number of snapshots used is $N_t = 200$. As usual, both Matrix-Pencil and Root-MUSIC are used as underlying methods for VEXPA.

The results for the first ($\sigma = 5, \rho = 2$) and second ($\sigma = 7, \rho = 3$) setups are shown in Fig. 5.9 and Fig. 5.10 respectively. For both figures, the top (bottom) graphs represent the results generated by using Matrix-Pencil (Root-MUSIC). As we use broadside ($\phi = 90°$) to calibrate the system, the errors for this angle are zero. For the first setup, for $P = 25$ dBm and $P = 10$ dBm, both Matrix-Pencil and Root-MUSIC underlying to VEXPA perform exceptionally, with errors smaller than 2.2° for all DOAs. When the signal strength is lower at $P = 0$ dBm, slightly larger errors occur, with four instances indicating VEXPA with MP underlying was unsuccessful in returning an estimated DOA. These instances that VEXPA failed to return any DOA are due to the cases that the clustering algorithm found no clusters from the base terms Ψ_i^σ and Ψ_i^ρ.

Similar results are seen for the second setup in Fig. 5.10. For $P = 0$ dBm, however, VEXPA with the Matrix-Pencil method underlying is unable to return an estimated DOA for any of the angles.

The errors of the practical experiments can largely be ascribed to two factors: the near-field effect and the anisotropic embedded element patterns. These are discussed in the following subsections.

5.5.1 Near-field effect

In Section 2.2, the assumptions of the DOA estimation problem are discussed. This includes the far-field assumption which states that if a source is far enough away from the receiving antennas, the spherical wavefront appears as an incoming plane wave signal. This implies that the phase difference between elements is only dependent on the angle of arrival.

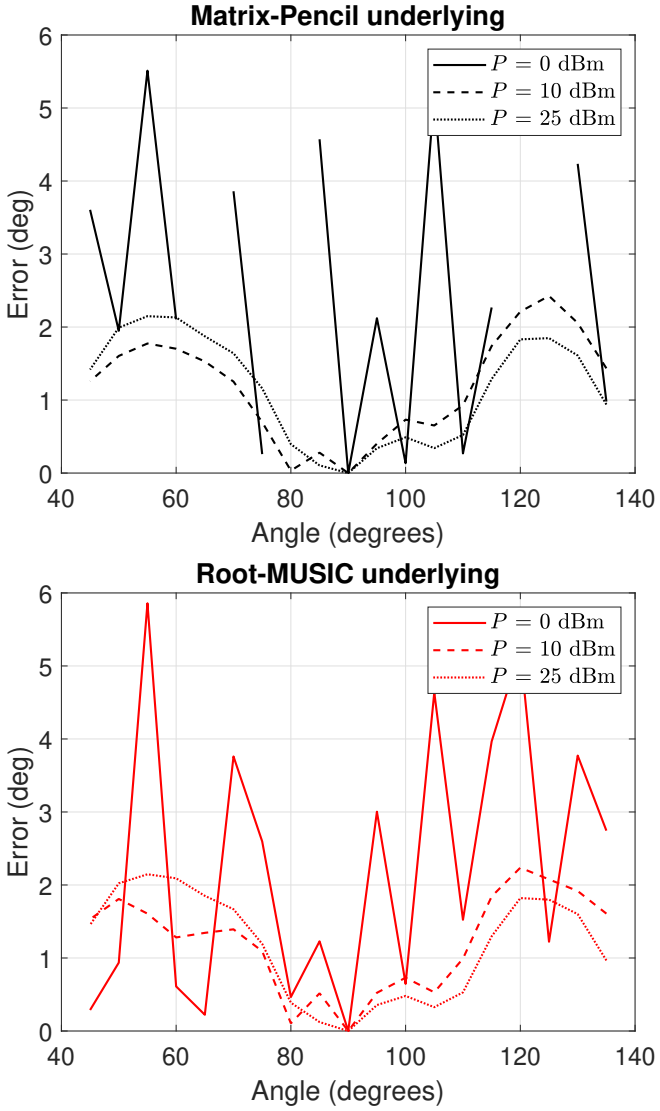

Figure 5.9: Results of the first array setup ($\sigma = 5$, $\rho = 2$), with the top and bottom graphs corresponding to Matrix-Pencil and Root-MUSIC as underlying DOA estimation method, respectively.

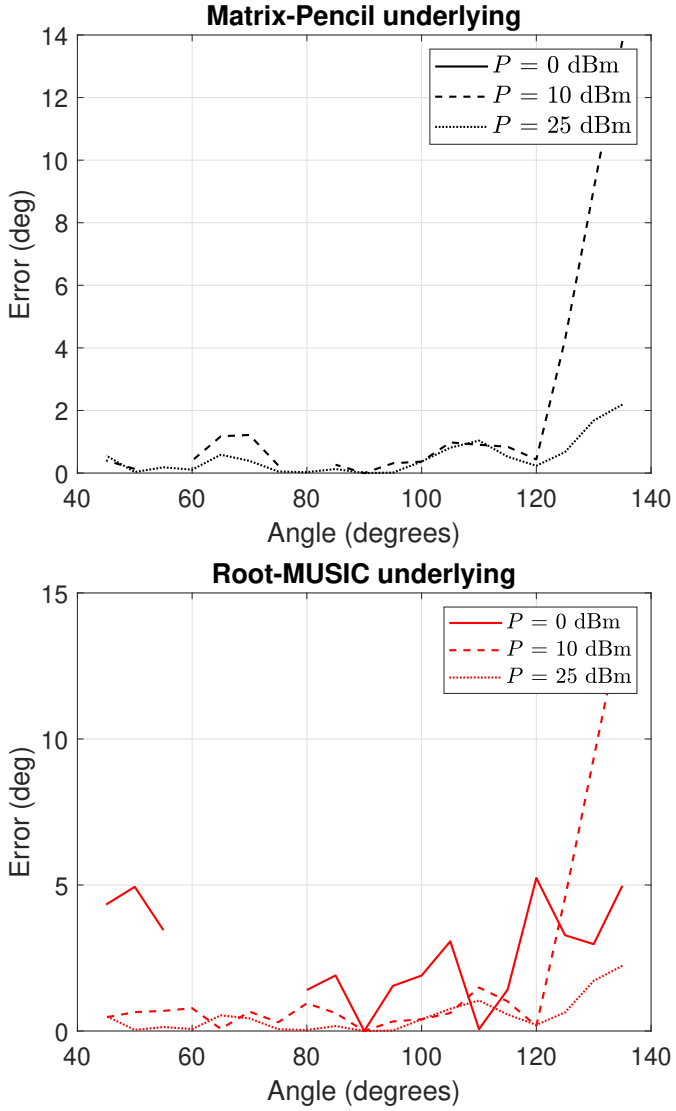

Figure 5.10: Results of the second array setup ($\sigma = 7$, $\rho = 3$), with the top and bottom graphs corresponding to Matrix-Pencil and Root-MUSIC as underlying DOA estimation method, respectively.

The far-field, given as the space further than $2D^2/\lambda$ from the antenna array, begins at 10.67 m from the array, where $D = 800$ mm, the length of the ground plane. The measured distance between the source and the antenna array in the anechoic chamber is 4.95 m, meaning that the source is in the near-field of the array. In Fig. 5.11 and Fig. 5.12 the significance of this effect for the first and second setup is shown. For broadside, the time delay is cancelled through calibration when we equalise the output signals of each element artificially. As we rotate the array away from broadside, however, the effect becomes significant, as can be seen by the errors at angles other than broadside in Fig. 5.9. Another thing to take into consideration is the alignment of the source with regards to the array: for the first setup, the four elements are positioned symmetrically about the centre of the ground plane slit, but for the second setup the first element is placed at the beginning of the slit, with the remaining elements placed in reference to the first one. This means that, for the second setup, the source is not directly aligned with the centre of the ground plane slit, but has a small offset. In turn, this implies that for the first setup, at broadside, the time delay between the two elements of ULA 1 is equal to the time delay between the two elements of ULA 2, which is not the case for the second setup. The unequal time delay is one of the factors contributing to the slightly sub-par performance of the second setup at lower power levels.

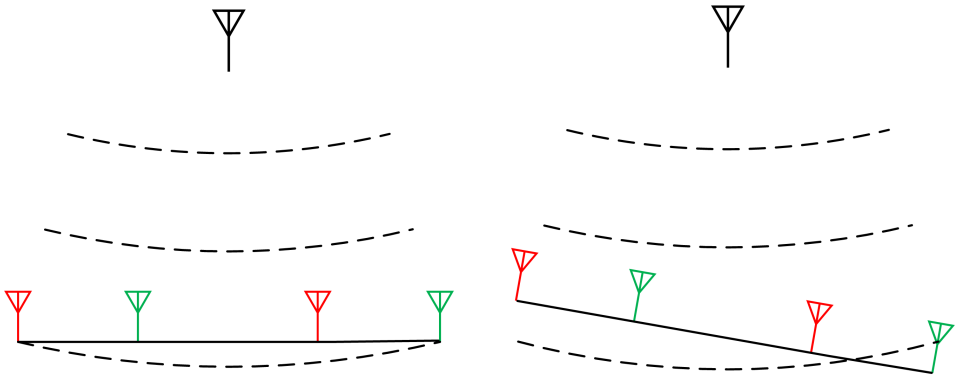

Figure 5.11: The near-field effect of the first setup. As the source is in the near-field of the array, the incoming signal has a spherical rather than plane wavefront, meaning that a time delay occurs between elements, even at broadside (left). The right-hand side shows the effect when the array is rotated to vary the DOA.

5.5.2 Anisotropic embedded element patterns

The embedded element pattern is the pattern of an antenna in its environment, i.e., with regards to the complete antenna array and ground plane. In

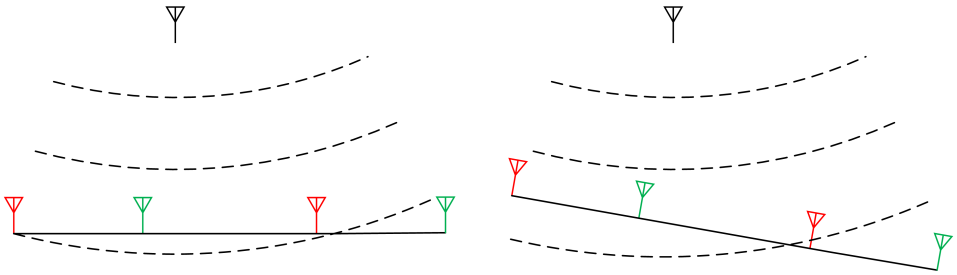

Figure 5.12: The near-field effect of the second setup. In this case, the source is not aligned directly with the centre of the array, meaning that there exists a different time delay for each element pair at broadside (left). The right-hand side shows the effect when the array is rotated to vary the DOA.

Section 2.2, we assumed the isotropic transmission of the incoming signal. This would require isotropic embedded element patterns, meaning that the directivity of all elements is equal for all angles of arrival. In this setup, however, this is not the case.

In Section 4.8 we discussed the effect of mutual coupling. Here we see a different consequence thereof: the mutual coupling between elements affect the embedded element patterns. To show this, the antenna patterns in the $\theta = 0°$ plane in CST are shown in Fig. 5.13 to Fig. 5.16.

Fig. 5.13 and Fig. 5.14 show the magnitude of the directivity in dBi for the first and second setup, respectively. We see that the patterns for each element are similar, but not identical. The level of directivity also differs with ϕ, although in the range of interest $\phi \in [45°, 135°]$, these differences are small.

Fig. 5.15 and Fig. 5.16 show the phase differences in degrees between the reference element (element 1) and the other three elements. It is portrayed together with the calculated phase differences, i.e., $\exp(j\omega\rho d\cos\phi_i/c)$ for element 2, $\exp(j\omega\sigma d\cos\phi_i/c)$ for element 3, and $\exp(j\omega(\sigma+\rho)d\cos\phi_i/c)$ for element 4. Again we see that, for the range $\phi \in [45°, 135°]$, the patterns represent the expected behaviour with some small errors.

Thus, the effect of mutual coupling is present, but is not so significant that no accurate results can be obtained. For improved results, a calibration procedure is needed to mitigate the unmatched embedded element patterns.

5.6 Conclusion

In this chapter we presented the practical experiment used to test the performance of VEXPA. The results proved to be very accurate, as VEXPA could successfully estimate the DOA. Improved results can be achieved by performing experiments with the antenna array farther away from the source, ensuring the far-field assumption is satisfied, as well as applying a more complex calibration method.

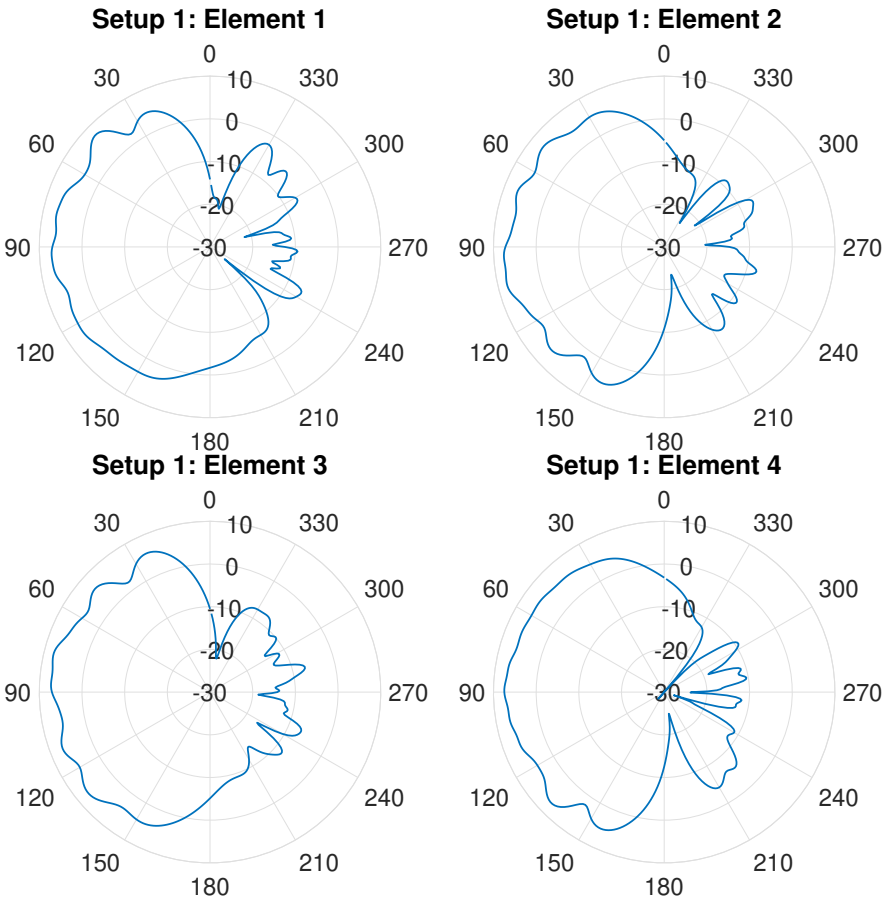

Figure 5.13: The magnitude of the embedded element patterns as simulated in CST for the first setup. The top left, top right, bottom left and bottom right graphs correspond to element 1, 2, 3 and 4, respectively. The graphs are plotted as dBi vs ϕ in degrees. The anisotropicity of the patterns, as well as the difference in patterns between elements, can be calibrated for more accurate results.

Referring back to Chapter 4, we briefly consider the practical limitations that were investigated to understand in which way they affected the results:

- **SNR**: By performing experiments at different power levels, we saw how the results get less accurate as the signal power is lowered. At the lower power levels, VEXPA fails to return an estimated angle of arrival, which means that the base terms returned by the underlying methods are scattered due to noise, leading to no clusters forming.

- **Number of snapshots**: We used $N_t = 200$ snapshots in the practical experiments, using $N_s = 100$ of these to calculate the covariance matrix in the case of Root-MUSIC. In Chapter 4 we saw that the biggest concern caused by fewer snapshots is when estimating the covariance

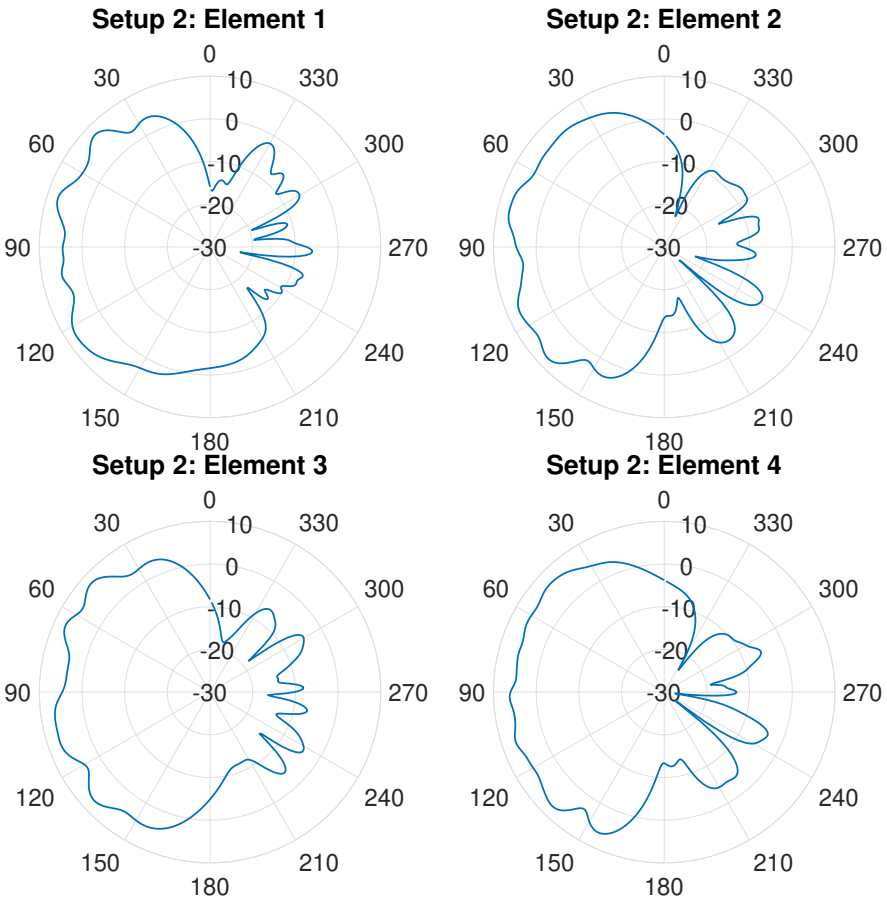

Figure 5.14: The magnitude of the embedded element patterns as simulated in CST for the second setup. The top left, top right, bottom left and bottom right graphs correspond to element 1, 2, 3 and 4, respectively. The graphs are plotted as dBi vs ϕ in degrees. The anisotropicity of the patterns, as well as the difference in patterns between elements, can be calibrated for more accurate results.

matrix. However, 100 snapshots are more than enough for an accurate calculation, and thus did not influence the results.

- **Quantisation errors**: In Chapter 4 we performed simulations investigating the effect of using an ADC, varying the number of bits from one to eight. With only one incoming signal, VEXPA is able to deliver accurate results from quantised data with only one bit. The oscilloscope used in the practical experiment has a built-in ADC with 12 bits, contributing to accurate results.

- **Systematic errors**: As mentioned before, the mutual coupling between elements, positional errors and differences in cable lengths all cause unwanted phase shifts in the received signals. A simple calibration method

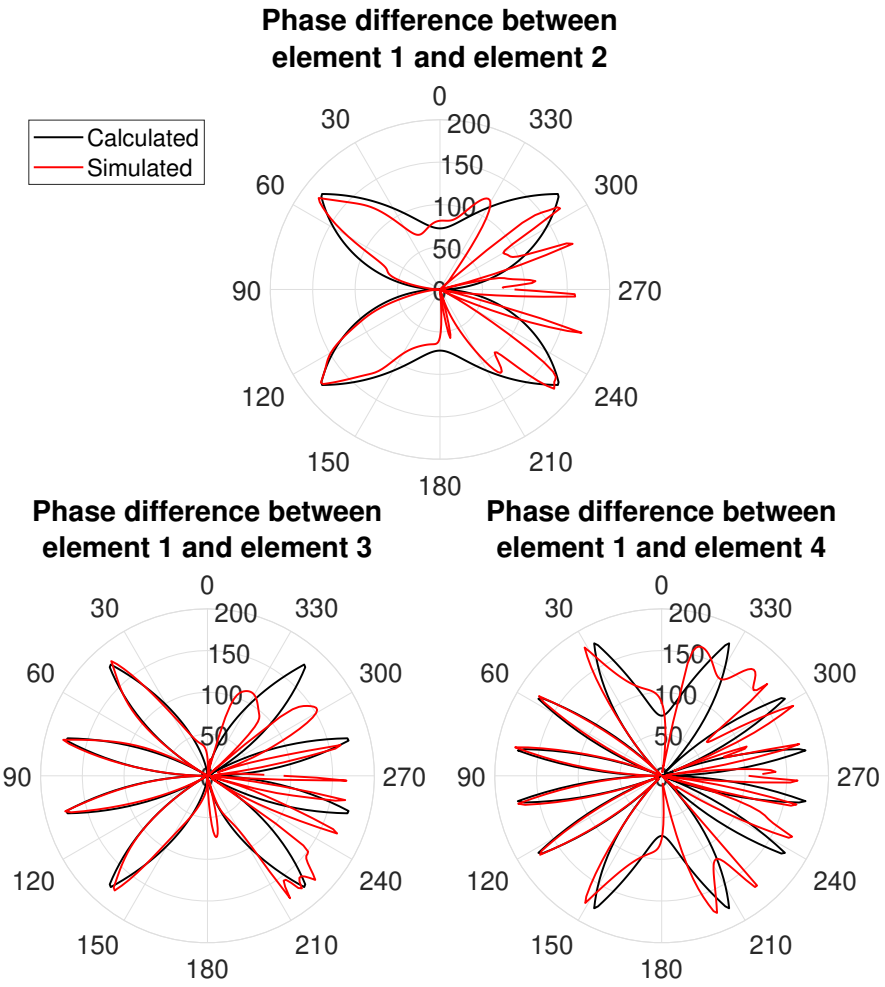

Figure 5.15: The phase differences of the embedded element patterns as simulated in CST for the first setup, with the phase of the first element taken as reference. The graphs are plotted as phase in degrees vs ϕ in degrees.

is applied to mitigate these errors, but they still influence the accuracy of the results negatively.

- **Narrowband assumption**: The signal generator used for the practical experiment produces a narrowband signal, and therefore there are no wideband effects influencing the results.

In conducting this practical experiment, the theory behind VEXPA as explained in Chapter 3 in addition to the practical non-idealities that were introduced in Chapter 4 could be explored, and thereby a deeper understanding of the sparse DOA estimation problem could be attained.

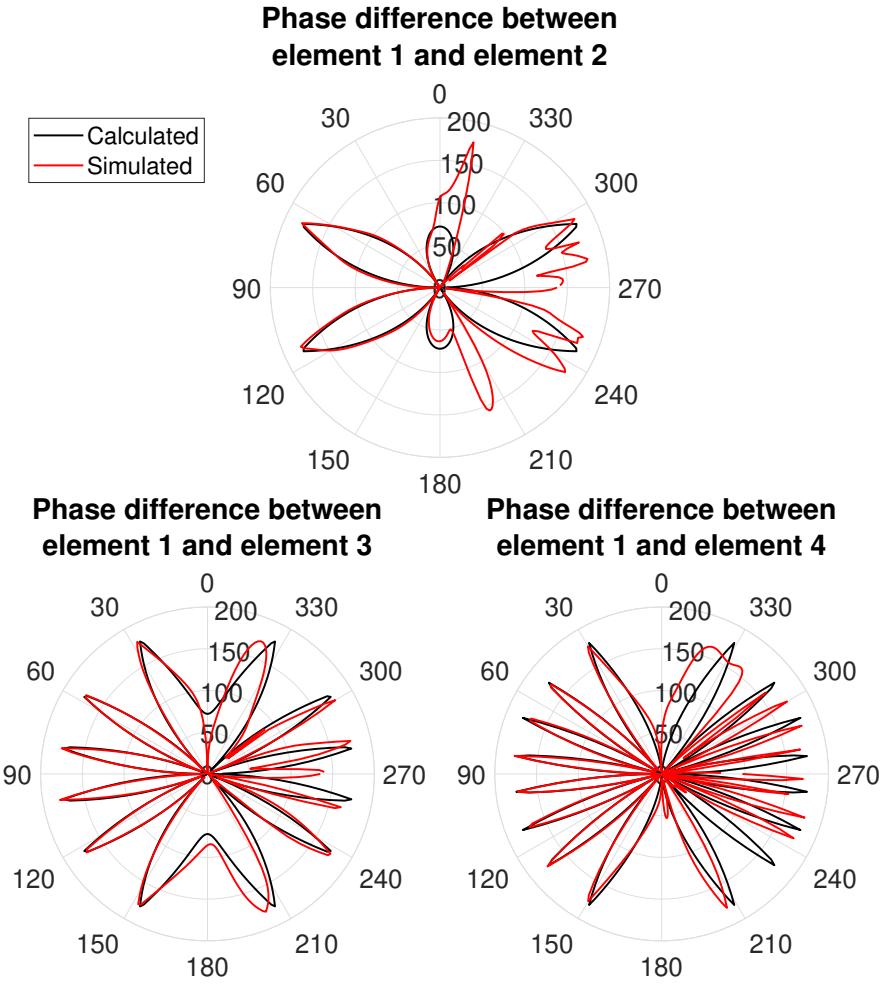

Figure 5.16: The phase differences of the embedded element patterns as simulated in CST for the second setup, with the phase of the first element taken as reference. The graphs are plotted as phase in degrees vs ϕ in degrees.

Chapter 6

Conclusion

This thesis investigated the practical performance of a direction-of-arrival (DOA) estimation method based on exponential analysis, called Validated Exponential Analysis (VEXPA). The appeal of this method lies in the fact that antenna elements can be spaced further than a half-wavelength apart, in a so-called sparse array configuration. Sparse arrays, in contrast to dense arrays, have an advantage of a finer resolution for the same number of antenna elements, as well as less mutual coupling.

We first discussed direction-of-arrival theory in general, and considered different existing DOA estimation methods, including ESPRIT, the Matrix-Pencil method and Root-MUSIC. Thereafter, we investigated the workings of the VEXPA method, including the required array configuration as well as the algorithm using the output data from the array.

Where VEXPA is originally used alongside the Matrix-Pencil method, which is a DOA estimation method that can be applied by using a single snapshot of data, we considered the usage of Root-MUSIC as underlying method. This method uses the covariance matrix of the array data, leading to two noticeable remarks: firstly, multiple snapshots are required for an accurate estimation of the covariance matrix; secondly, if more than one incoming signals are present, these signals need to be incoherent to ensure a non-singular covariance matrix. This means the signals are required to have slightly different frequencies and phases to ensure complete incoherence.

Considering the improved angular resolution achieved by using sparse instead of dense arrays, we saw an instance where the resolution was improved by a factor of 5 by using VEXPA.

Next, we considered VEXPA's ability to detect the number of incoming signals accurately, by comparing it to an existing method using the multiplicity of eigenvalues in the decomposition of the data. Here we saw that those underlying methods that use a single snapshot can benefit from VEXPA's approach, but that both approaches are accurate for methods using the covariance matrix.

An important investigation of the performance of VEXPA is its ability to

use quantised data. It was observed that Root-MUSIC performs better than the Matrix-Pencil method as underlying method when the data is quantised by an ADC with few bits. When multiple signals are present, however, the number of signals need to be known even for Root-MUSIC to accurately perform with one-bit data. The work done in this section, as well as that of the estimation of the number of signals mentioned above, are in preparation for a conference paper.

After this, some systematic errors were investigated, namely mutual coupling, calibration errors and positional errors. The work done on the effect of positional errors on the performance of VEXPA was also presented in an abstract paper at the 2019 IEEE-APS Topical Conference on Antennas and Propagation in Wireless Communications (APWC).

Thereafter, a shortcoming of VEXPA was investigated: when multiple signals are present from angles that lead to equal or nearly-equal base terms, the underlying method only detects one signal. Two different approaches to this problem were discussed. Firstly, by selecting a different set of antenna elements from the virtual dense array and performing a second round of Prony-like estimation. However, it was noted that this method has the disadvantage of additional required antenna elements. Secondly, by assuming a wideband signal is available, we can perform VEXPA on the different frequency components to cover frequencies for which the specific angles do not cause collided base terms. We saw that for this to be a viable solution, however, the bandwidth of the signal should be larger than most of what is usually observed in practice. Thus, we should be aware that collided base terms are a possibility that could occur.

Finally, we constructed a small co-prime antenna array setup, with four elements, each sub-ULA consisting of two elements. We used simple printed dipole elements, and used a TekTronix oscilloscope to capture the data. The system was set up in an anechoic chamber to minimise interference, and the array was rotated to vary the angle of arrival. VEXPA could successfully estimate the DOA.

Possible expansions of this project include:

- Constructing a larger practical system with more elements, in order to consider the practical performance when multiple signals are present. Specifically, attention can be given to the practical susceptibility to collided base terms, and incoherent signals for underlying methods such as Root-MUSIC.

- The implementation of VEXPA for planar arrays has been developed, as well as a similar small practical setup such as the one in this thesis. Future work on this project includes performing RFI detection by using the existing infrastructure of the Low-Frequency Array (LOFAR) infrastructure in the Netherlands. The possibility of using VEXPA for point source imaging will also be investigated.

Bibliography

[1] M. Briani, A. Cuyt, and W.-S. Lee, "VEXPA: Validated EXPonential Analysis through regular sub-sampling," *arXiv preprint arXiv:1709.04281*, 2017.

[2] B. Burke, F. Graham-Smith, and P. Wilkinson, *An Introduction to Radio Astronomy*. Cambridge University Press, 2019. [Online]. Available: https://books.google.co.za/books?id=lOKfDwAAQBAJ

[3] The SKA Project. [Online]. Available: https://www.skatelescope.org/the-ska-project/

[4] What Is Radio Astronomy? [Online]. Available: https://www.skatelescope.org/radio-astronomy/

[5] P.-S. Kildal, *Foundations of Antenna Engineering: A Unified Approach for Line-of-sight and Multipath*, ser. Artech House antennas and electromagnetics analysis library. Artech House, 2015. [Online]. Available: https://books.google.co.za/books?id=_MDzrQEACAAJ

[6] J. L. Volakis, *Antenna Engineering Handbook*. McGraw-Hill Education, 2018. [Online]. Available: https://books.google.co.za/books?id=CMx7DwAAQBAJ

[7] F. Knaepkens, A. Cuyt, W. Lee, and D. I. L. de Villiers, "Regular sparse array direction of arrival estimation in one dimension," *IEEE Transactions on Antennas and Propagation*, vol. 68, no. 5, pp. 3997–4006, 2020.

[8] Z. Chen, G. Gokeda, and Y. Yu, *Introduction to Direction-of-arrival Estimation*. Artech House, 2010.

[9] V. Krishnaveni, T. Kesavamurthy, and B. Aparna, "Beamforming for direction-of-arrival (DOA) estimation- a survey," *International Journal of Computer Applications*, vol. 61, no. 11, 2013.

[10] S. S. Balabadrapatruni, "Performance evaluation of direction of arrival estimation using Matlab," *Signal & Image Processing*, vol. 3, no. 5, p. 57, 2012.

[11] R. Schmidt, "Multiple emitter location and signal parameter estimation," *IEEE Transactions on Antennas and Propagation*, vol. 34, no. 3, pp. 276–280, March 1986.

[12] M. Wax, "Detection and estimation of superimposed signals," Ph.D. dissertation, 03 1985.

[13] H. Tang, "DOA estimation based on MUSIC algorithm," 2014.

[14] A. Barabell, "Improving the resolution performance of eigenstructure-based direction-finding algorithms," in *ICASSP'83. IEEE International Conference on Acoustics, Speech, and Signal Processing*, vol. 8. IEEE, 1983, pp. 336–339.

[15] A. Vesa, "Direction of arrival estimation using MUSIC and root–MUSIC algorithm," in *18th Telecommunications Forum, Pg*, 2010, pp. 582–585.

[16] R. Roy and T. Kailath, "ESPRIT–estimation of signal parameters via rotational invariance techniques," *IEEE Transactions on acoustics, speech, and signal processing*, vol. 37, no. 7, pp. 984–995, 1989.

[17] R. Roy, "Esprit-estimation of signal parameters via rotational invariance techniques," Ph.D. dissertation, 1987.

[18] E. Assiimwe, E. Mwangi, and D. Konditi, "A matrix pencil method for the efficient computation of direction of arrival estimation for weakly correlated signals using uniform linear array in a low SNR regime," *International Journal of Engineering Research and Technology*, vol. 11, pp. 1347–1361, 01 2018.

[19] F. R. Gantmakher, *The theory of matrices*. American Mathematical Soc., 1959, vol. 131.

[20] K. Ikramov, "Matrix pencils: Theory, applications, and numerical methods," *Journal of Soviet Mathematics*, vol. 64, 04 1993.

[21] H. M. Elkamchouchi and M. M. Omar, "An efficient computational approach in the matrix pencil method to find one dimensional and two dimensional direction of arrival," in *2007 National Radio Science Conference*. IEEE, 2007, pp. 1–8.

[22] F. Sun, B. Gao, L. Chen, and P. Lan, "A low-complexity ESPRIT-based DOA estimation method for co-prime linear arrays," *Sensors*, vol. 16, no. 9, p. 1367, 2016.

[23] P. P. Vaidyanathan and P. Pal, "Sparse sensing with co-prime samplers and arrays," *IEEE Transactions on Signal Processing*, vol. 59, no. 2, pp. 573–586, 2010.

[24] K. Liu and Y. D. Zhang, "Coprime array-based DOA estimation in unknown nonuniform noise environment," *Digital Signal Processing*, vol. 79, pp. 66 – 74, 2018. [Online]. Available: http://www.sciencedirect.com/science/article/pii/S1051200418301064

[25] A. Moffet, "Minimum-redundancy linear arrays," *IEEE Transactions on antennas and propagation*, vol. 16, no. 2, pp. 172–175, 1968.

[26] A. Patwari and G. R. Reddy, "A conceptual framework for the use of minimum redundancy linear arrays and flexible arrays in future smartphones," *International Journal of Antennas and Propagation*, vol. 2018, 2018.

[27] R. N. Bracewell, "Radio astronomy techniques," in *Astrophysik V: Verschiedenes/Astrophysics V: Miscellaneous*. Springer, 1962, pp. 42–129.

[28] K. Han and A. Nehorai, "Wideband direction of arrival estimation using nested arrays," in *2013 5th IEEE International Workshop on Computational Advances in Multi-Sensor Adaptive Processing (CAMSAP)*, 2013, pp. 188–191.

[29] P. Pal and P. P. Vaidyanathan, "Nested arrays: A novel approach to array processing with enhanced degrees of freedom," *IEEE Transactions on Signal Processing*, vol. 58, no. 8, pp. 4167–4181, 2010.

[30] R. de Prony, "Essai expérimental et analytique sur les lois de la dilatabilité des fluides élastiques et sur celles de la force expansive de la vapeur de l'eau et de la vapeur de l'alkool, á différentes températures," *J. Ec. Poly.*, vol. 1, pp. 24–76, 1795.

[31] L. Weiss and R. McDonough, "Prony's method, z-transforms, and Padé approximation," *Siam Review*, vol. 5, no. 2, pp. 145–149, 1963.

[32] M. Ester, H.-P. Kriegel, J. Sander, X. Xu *et al.*, "A density-based algorithm for discovering clusters in large spatial databases with noise." in *Kdd*, vol. 96, no. 34, 1996, pp. 226–231.

[33] W. P. Robins, *Phase Noise in Signal Sources*, ser. Telecommunications. Institution of Engineering and Technology, 1984. [Online]. Available: https://digital-library.theiet.org/content/books/te/pbte009e

[34] X. Huang and B. Liao, "One-Bit MUSIC," *IEEE Signal Processing Letters*, vol. 26, no. 7, pp. 961–965, 2019.

[35] R. Weideman, D. I. L. de Villiers, and R. Louw, "Practical limitations of the VEXPA estimation method in sparse regular arrays," in *XXXIV General Assembly and Scientific Symposium (GASS) of the International Union of Radio Science (Union Radio Scientifique Internationale-URSI)*, 2021, in preparation.

[36] J. G. Proakis, *Digital signal processing: principles algorithms and applications*. Pearson Education India, 2001.

[37] F. Sohrabi and W. Yu, "Hybrid digital and analog beamforming design for large-scale antenna arrays," *IEEE Journal of Selected Topics in Signal Processing*, vol. 10, no. 3, pp. 501–513, 2016.

[38] O. Bar-Shalom and A. J. Weiss, "DOA estimation using one-bit quantized measurements," *IEEE Transactions on Aerospace and Electronic Systems*, vol. 38, no. 3, pp. 868–884, 2002.

[39] D. I. L. de Villiers, R. Louw, R. Weideman, A. Cuyt, F. Knaepkens, and W. Lee, "Practical performance of regular sparse array direction of arrival estimation in 1-d," in *2019 IEEE-APS Topical Conference on Antennas and Propagation in Wireless Communications (APWC)*, 2019, pp. 112–112.

[40] S. Weglarczyk, "Kernel density estimation and its application," *ITM Web of Conferences*, vol. 23, p. 00037, 01 2018.

[41] Altair Development S. A. (Pty) Ltd and Stellenbosch, South Africa, *FEKO*. Suite 2017. [Online], 2017.

[42] M. Zatman, "How narrow is narrowband?" *IEE Proceedings-Radar, Sonar and Navigation*, vol. 145, no. 2, pp. 85–91, 1998.

[43] R. Compton, *Adaptive Antennas: Concepts and Performance*. Prentice-Hall, 1988. [Online]. Available: https://books.google.co.za/books?id=jnMeAQAAIAAJ

[44] E. Kaplan and C. Hegarty, *Understanding GPS: Principles and Applications*, ser. Artech House mobile communications series. Artech House, 2005. [Online]. Available: https://books.google.co.za/books?id=-sPXPuOW7ggC

[45] C. Votis, P. Kostarakis, and A. Alexandridis, "Design, analysis, and measurements of an antenna structure for 2.4 GHz wireless applications," *International Journal of Antennas and Propagation*, vol. 2010, 11 2010.

[46] *6 Series MSO Mixed Signal Oscilloscope Datasheet*, Tektronix, 2 2020.